POLITECNICO DI MILANO

Scuola di Ingegneria Industriale e dell'Informazione

Corso di Laurea Magistrale in Ingegneria Aeronautica

DESIGN OF SUBOPTIMAL CONTROLLERS FOR REDUCTION OF VIBRATION AND SOUND RADIATION OF PLATES USING INERTIAL ACTUATORS

Relatore:
Prof. Lorenzo Dozio

Tesi di laurea di:
Francesco Riccardo De Leo
Matr. 804648

Anno accademico 2014/2015

Acknowledgments

My first and dutiful thanks go to Prof. Lorenzo Dozio, for his teachings and advices and for guiding me in the writing of this thesis, with great willingness, competence and patience.

My thanks also goes to all the teachers of Politecnico di Milano who transmitted their knowledge to me with passion and motivation.

A big thanks goes to my family and, in particular, to my parents, for their patience, their support, and their encouragement during this whole period of studies.

A special thanks goes to my girlfriend, Sara, for standing by me during these years, making every day better.

Finally, I would like to thank all my friends and my collegues. They made these years of studies the best adventure of my life.

Contents

List of Figures

List of Tables

Abstract

The research presented in this work of thesis is addressed to the problem of controlling vibration (active vibration control, AVC) and noise (active structural acoustic control, ASAC) of rectangular plates, using multiple accelerometers and inertial actuators. A coupled structural acoustic model is developed, taking into account the electromechanical dynamics associated to the actuators and the dynamics of the integrators, that convert acceleration measures to velocities. Relying on the suboptimal control technique, a velocity feedback optimal controller is designed. In particular, the types of controller studied are the decentralized velocity feedback with independent gains, the centralized velocity feedback and the decentralized velocity feedback with equal gains. Results and considerations are presented for the reduction of vibration and sound radiation of plates with variable characteristics, dimensions and boundary conditions. Configurations of collocated sensor/actuator pairs, both in assigned positions and located by an optimal placement technique, are studied. Two optimization approaches based on the use of different performance indeces are presented for vibro-acoustic control problems.

Sommario

Il presente lavoro di tesi ha l'obiettivo di studiare il problema del controllo di vibrazioni (controllo attivo delle vibrazioni) e del rumore (controllo attivo del rumore) di piastre rettangolari, utilizzando accelerometri e attuatori inerziali. Viene sviluppato un modello strutturale-acustico accoppiato, tenendo conto della dinamica elettromeccanica degli attuatori e della dinamica degli integratori, i quali convertono misure di accelerazione in velocitá. Affidandosi alla tecnica del controllo sub-ottimo, viene sviluppato un controllore ottimo con controreazione sulle velocitá. In particolare, i tipi di controllore esaminati sono il decentralizzato con guadagni indipendenti, il centralizzato e il decentralizzato con guadagni uguali. Vengono presentati risultati e considerazioni riguardo la riduzione delle vibrazioni e della radiazione acustica di piastre con differenti caratteristiche, dimensioni e condizioni al controrno. Vengono studiate configurazioni di coppie collocate di sensori e attuatori, sia in posizioni assegnate che posizionate tramite una tecnica di collocamento ottimo. Vengono presentati due approcci di ottimizzazione, basati sull'utilizzo di differenti indici di prestazione, per problemi di controllo vibro-acustico.

Chapter 1

Introduction

Vibration control of flexible structures is an important issue in many engineering applications. As large lightweight structures used in the aeronautical and space fields are characterized by modal frequencies and damping ratios relatively low, they are widely affected by vibrations that may cause problems both in terms of safety and comfort. The transmission of acoustic noise is one of the main issues and the improvement of the flight comfort trying to reduce radiated noise produced by the vibrating structures of the airplane respresents an important challege in civil aeronautics. Therefore, to comply with the request of vibration suppression and noise attenuation, the concept of actively controlled structures with sensors and actuators has to be introduced. In recent years, several studies have been conducted on active control, both using inertial and piezoelectric actuators.

The aim of this work of thesis is to present active control of vibration and structure-borne noise of rectangular plates by the method of subotpimal control and using inertial actuators both in assigned and optimal positions. The structural model of the plates here considered, described in Chapter 2, is developed using the Ritz tecnique, whose application to the analysis of rectangular Kirchhoff plates is discussed by Dozio [6]. The plate model obtained is then coupled with the electromechanical dynamics of the actuators, as done in the works of Baumann and Elliot [4] and Griffin et al. [10], and with the dynamics of real integrators that provide velocities from acceleration measures. In Chapter 3 the structural model is finally coupled with the radiation model, obtained by the Radiation Modal Expansion (RME) technique developed by Gibbs et al. [9], to obtain the following augmented state space system:

$$\begin{cases} \dot{\mathbf{x}} = \mathbf{A}\mathbf{x} + \mathbf{B}\mathbf{u} \\ \mathbf{y} = \mathbf{C}\mathbf{x} \end{cases} \tag{1.1}$$

$\mathbf{A}$, $\mathbf{B}$ and $\mathbf{C}$ are the state space matrices, $\mathbf{x}$ is the state vector, $\mathbf{u}$ is the vector of inputs and $\mathbf{y}$ is the output vector. In order to attenuate both vibration and radiated sound, a velocity feedback control system is implemented, based on the following control law:

$$\mathbf{u} = -\mathbf{G}\mathbf{y} \tag{1.2}$$

Three control strategies based on different structures of the gain matrix $\mathbf{G}$ are discussed:

- Decentralized suboptimal control: $\mathbf{G}$ matrix is diagonal with independent gains.
- Centralized suboptimal control: $\mathbf{G}$ matrix is full with independent gains.
- Decentralized suboptimal control with equal gains: $\mathbf{G}$ matrix is diagonal with equal gains.

According to the theory of stochastic suboptimal control presented in Chapter 4, the optimal control solutions are obtained by minimizing the following cost function:

$$J = E\left[\mathbf{z}^{\mathbf{T}}\mathbf{W}_{zz}\mathbf{z} + \mathbf{u}^{\mathbf{T}}\mathbf{W}_{uu}\mathbf{u}\right] \tag{1.3}$$

where $\mathbf{z}(t)$ is a suitably selected performance vector, $\mathbf{W}_{zz}$ is a nonnegative symmetric weighting matrix associated with the performance and $\mathbf{W}_{uu}$ is a positive definite symmetric weighting matrix related to the control effort. The minimization problem to be solved is written as

$$\min J(\mathbf{X}) \rightarrow \mathbf{X}^* \tag{1.4}$$

where $\mathbf{X}^*$ are the optimum values that minimize J.
In our specific case, J is the cost functional defined in Equation 1.3 and $\mathbf{X}$ is

- a vector with the elements g_{ik} of the gain matrix, if an optimization of the gains in performed;

- a vector containing the components g_{ik} of the gain matix, the positions of sensors $\mathbf{X}_s$ and the positions of actuators $\mathbf{X}_a$ if an optimization in terms of gains and actuators/sensors placement is performed.

Some results in terms of active vibration control (AVC) using sensor/actuator collocated pairs in assigned positions are presented in Chapter 5, focusing on the differences among decentralized, centralized and decentralized with equal gains controllers.
In Chapter 6 some AVC results are obtained using a minimization procedure which is capable of providing not only optimal gains but also optimal positions of sensors and actuators. Differences with respect to the fixed grid approach are discussed.
Then, in Chapter 7, some examples of active structural acoustic control (ASAC) will be presented. In particular, results obtained performing an optimization specifically aimed at suppressing vibration or noise are discussed.

Chapter 2

Structural model

A plate model based on the classical Kirchhoff theory is here considered. Transverse vibration modes are considered to be of more interest compared to in-plane vibration modes since the latter have significantly higher frequencies than those related to transverse vibration. Therefore, in-plane vibration modes often fall beyond the typical range of frequency content of force excitations. For this reason, only the dynamics related to transverse displacements will be considered.
The model of the plate, both for isotropic and orthotropic cases, is fully described by Dozio [6], exployting a Ritz-based approach. The Ritz procedure consists in approximating the normal displacement variable through a linear combination of global assumed functions, commonly known as admissible functions, each satisfying at least the geometrical boundary conditions of the plate. Due to its conceptual simplicity, wide flexibility, high reliability and computational efficiency the Ritz tecnique has been widely used. The unknown coefficients of the combination can be obtained from the minimization of the energy functional of the system or exploiting the Principle of Virtual Work. Several effects representing practical situations can be considered, including in-plane loads, elastically restrained edges, rigid/elastic concentrated masses, intermediate line and point supports or their combinations.
This simple model of the plate can be improved by first including the mechanical model of the electrodynamic inertial actuators and the accelerometer sensors. The inertial actuators are control devices in which the current in a coil suspended in a magnetic gap provides a force between the structure and a proof mass. They are modelled as damped harminic oscillators with a plate-attached point mass modeling the case, while the sensors are simply considered as point masses attached to the plate.
A further step will be to include the dynamics related to real integrators that

provide velocities from acceleration measurements collected by the sensors. Finally, the electrical dynamics of the actuators is included into the model: this allow to consider voltages provided to the actuators as input variables of the problem.
The dynamic effects described can be coupled together, obtaining the overall state space model of the plate equipped with control actuator/sensor pairs.

2.1 Ritz formulation

Let's consider a flat thin rectangular orthotropic plate as in Figure 2.1, with length a and width b, lying in the (x, y) plane. The transverse displacement field of the plate is indicated by $w = w(x, y, t)$, where the origin of the (x, y) coordinate system is located at the plate center.

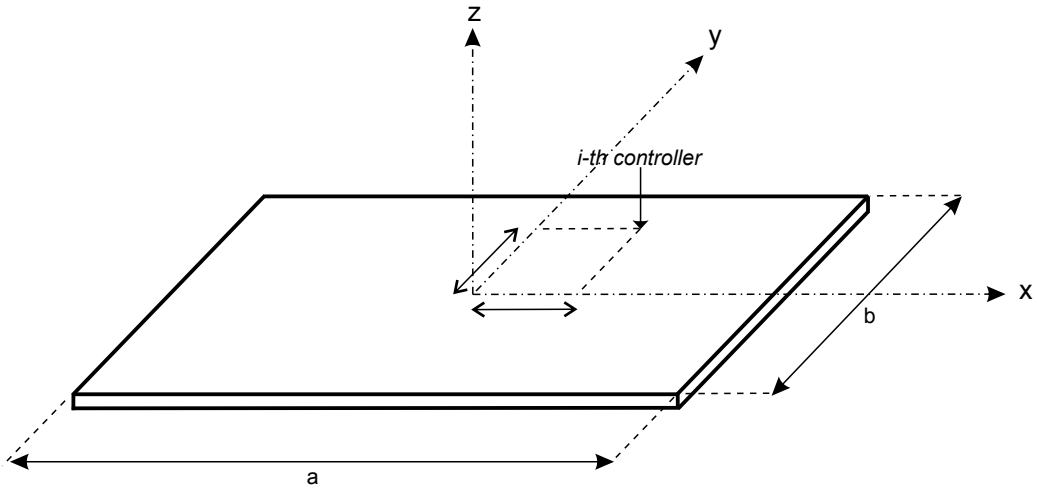

Figure 2.1: Rectangular plate lying in the (x, y) plane.

The counterclockwise four-letter symbolic notation introduced by Leissa [11] is used to describe classical boundary conditions for each edge:

- S = simply supported: zero deflection and free rotation.
- C = clamped: zero deflection and zero rotation.
- F = free: free deflection and free rotation.

The following non-dimensional coordinates are introduced:

$$\xi = \frac{2x}{a}, \quad \eta = \frac{2y}{b}, \tag{2.1}$$

The Ritz approximation is employed by assuming the following solution:

$$w(\xi, \eta, t) = \sum_{m=1}^{M} \sum_{n=1}^{N} X_m(\xi) Y_n(\eta) u_{mn}(t) \tag{2.2}$$

where the one-dimensional admissible functions proposed by Beslin and Nicolas [5] are used:

$$X_m(\xi) = sin(a_m\xi + b_m)sin(c_m\xi + d_m) \tag{2.3}$$
$$Y_n(\eta) = sin(a_n\eta + b_n)sin(c_n\eta + d_n) \tag{2.4}$$

The coefficients a_m, b_m, c_m, d_m and a_n, b_n, c_n, d_n can be selected according to the boundary conditions, as proposed by Dozio [6].
The same result can be obtained and expressed through a matrix notation as follows:

$$\mathbf{w}(\xi, \eta, t) = \mathbf{N}(\xi, \eta)\mathbf{u}(t) \tag{2.5}$$

expressing the components of the vector $\mathbf{N}(\xi, \eta)$ as the product of the admissible functions $X_m(x)$ and $Y_n(y)$:

$$\mathbf{N}(\xi, \eta) = \begin{bmatrix} X_1Y_1 & X_1Y_2 & \dots & X_1Y_N & X_2Y_1 & \dots X_2Y_N & \dots & X_MY_N \end{bmatrix} \tag{2.6}$$

and the column vector $\mathbf{u}(t)$ contains the generalized coordinates

$$\mathbf{u}(t) = \begin{bmatrix} u_{11} & u_{12} & \dots & u_{MN} \end{bmatrix}^T \tag{2.7}$$

2.2 Dynamic equations of the plate with ideal force actuators and velocity sensors

Once selected the material properties, the plate dimensions, the boundary conditions and the other complicating factors on the plate, the model ends up with the complete Mass and Stiffness matrices of the plate, $\mathbf{M}_p$ and $\mathbf{K}_p$. These matrices have dimensions $(M \cdot N \times M \cdot N)$, where M and N are the orders of the Ritz series expansion along x and y directions, respectively.
Once the number N_{sa} and locations of the actuators are selected, the equations of motion of the plate forced by N_{sa} ideal point forces $f_i(t)$ at points (ξ_{a_i}, η_{a_i}) can be written.
The plate is also assumed to be subjected to a distributed white pressure field, acting as a disturbance on the structure.

According to the Principle of Virtual Work, the equations of motion can be written as:

$$\mathbf{M}_p\ddot{\mathbf{u}}(t) + \mathbf{K}_p\mathbf{u}(t) = \mathbf{L}_{c_a}\mathbf{f}(t) + \mathbf{L}_d d(t) \tag{2.8}$$

where $\mathbf{f}(t)$ is the vector of actuator forces, $d(t)$ is a white noise disturbance, $\mathbf{M}_p$ and $\mathbf{K}_p$ are plate matrices resulting from the Ritz approximation, $\mathbf{L}_{c_a}$ and $\mathbf{L}_d$ are the matrices containing the Ritz functions evaluated at the actuator's locations and the integral over the plate surface of the Ritz functions, respectively:

$$\mathbf{L}_{c_a} = \begin{bmatrix}\mathbf{N}^T(\xi_{a_1},\eta_{a_1}) & \mathbf{N}^T(\xi_{a_2},\eta_{a_2}) & \dots & \mathbf{N}^T(\xi_{N_{sa}},\eta_{N_{sa}})\end{bmatrix} \tag{2.9}$$

$$\mathbf{L}_d = \frac{ab}{4}\int_{-1}^{1}\int_{-1}^{1}\mathbf{N}^T d\xi d\eta \tag{2.10}$$

The above problem is then transformed into modal coordinates in order to easily manage the model order reduction.
The eigenproblem associated with Equation 2.2, even when it is large since many functions are used in the Ritz approximation, can be solved numerically in a very efficient way through iterative methods. After computing eigenvalues and eigenvectors, a small amount of damping, ζ, is included in the response of the modes. Beeing $\mathbf{q}(t)$ the vector of modal coordinates and $\mathbf{U}$ the mass-normalized eigenvectors matrix, such that $\mathbf{u}(t) = \mathbf{U}\mathbf{q}(t)$, the following modal model of the plate is obtained: [1]

$$\ddot{\mathbf{q}}(t) + \mathbf{Diag}\{2\zeta_j\omega_j\}\dot{\mathbf{q}}(t) + \mathbf{Diag}\{\omega_j^2\}\mathbf{q}(t) = \mathbf{U^T}\mathbf{L}_{c_a}\mathbf{f}(t) + \mathbf{U^T}\mathbf{L}_d d(t) \tag{2.11}$$

where ω_j are the undamped eigenvalues of the plate.
If the equations of motion are projected on a subset $\mathbf{U}_L$ of the eigenvectors matrix and not on the entire set, a reduced order modal model is obtained:

$$\ddot{\mathbf{q}}_L(t)+\mathbf{Diag}\{2\zeta_j\omega_j\}\dot{\mathbf{q}}_L(t)+\mathbf{Diag}\{\omega_j^2\}\mathbf{q}_L(t) = \mathbf{U}_L^T\mathbf{L}_{c_a}\mathbf{f}(t)+\mathbf{U}_L^T\mathbf{L}_d\mathbf{d}(t) \tag{2.12}$$

This reduced model will be used to design the velocity feedback control.

[1] As $\mathbf{U}$ is the mass-normalized eigenverctors matrix for the plate model, $\mathbf{U}^T\mathbf{M}_p\mathbf{U} = \mathbf{I}$.

The equations of motion written before can be expressed in a state space form as follows:

$$\begin{Bmatrix} \dot{\mathbf{q}}_L \\ \ddot{\mathbf{q}}_L \end{Bmatrix} = \mathbf{A}_{p_0} \begin{Bmatrix} \mathbf{q}_L \\ \dot{\mathbf{q}}_L \end{Bmatrix} + \mathbf{B}_{up_0}\mathbf{f} + \mathbf{B}_{dp_0}d \tag{2.13}$$

with

$$\mathbf{A}_{p_0} = \begin{bmatrix} \mathbf{0} & \mathbf{I} \\ -\mathbf{Diag}\{\omega_j^2\} & -\mathbf{Diag}\{2\zeta_j\omega_j\} \end{bmatrix}$$

$$\mathbf{B}_{up_0} = \begin{bmatrix} \mathbf{0} \\ \mathbf{U}_L^T\mathbf{L}_{c_a} \end{bmatrix}$$

$$\mathbf{B}_{dp_0} = \begin{bmatrix} \mathbf{0} \\ \mathbf{U}_L^T\mathbf{L}_{d} \end{bmatrix}$$

If ideal velocity sensors located in (ξ_{s_i}, η_{s_i}) are considered in order to implement a direct output velocity feedback control , the output equation is given by:

$$\mathbf{y}_{p_0} = \dot{\mathbf{w}}(\xi_{s_i}, \eta_{s_i}) = \mathbf{L}_{c_s}\mathbf{U}_L\dot{\mathbf{q}}_L \tag{2.14}$$

with

$$\mathbf{L}_{c_s} = \begin{bmatrix} N(\xi_{s_1}, \eta_{s_1}) \\ N(\xi_{s_2}, \eta_{s_2}) \\ \cdots \\ N(\xi_{N_{sa}}, \eta_{N_{sa}}) \end{bmatrix} \tag{2.15}$$

which cast into a state space model gives:

$$\mathbf{y}_{p_0} = \mathbf{C}_{yp_0} \begin{Bmatrix} \mathbf{q}_L \\ \dot{\mathbf{q}}_L \end{Bmatrix} \tag{2.16}$$

with

$$\mathbf{C}_{yp_0} = \begin{bmatrix} \mathbf{0} & \mathbf{L}_{c_s}\mathbf{U}_L \end{bmatrix} \tag{2.17}$$

So a state space formulation of a plate provided with ideal actuators and

ideal velocity sensors has been derived.

2.3 Mechanical model of inertial actuators

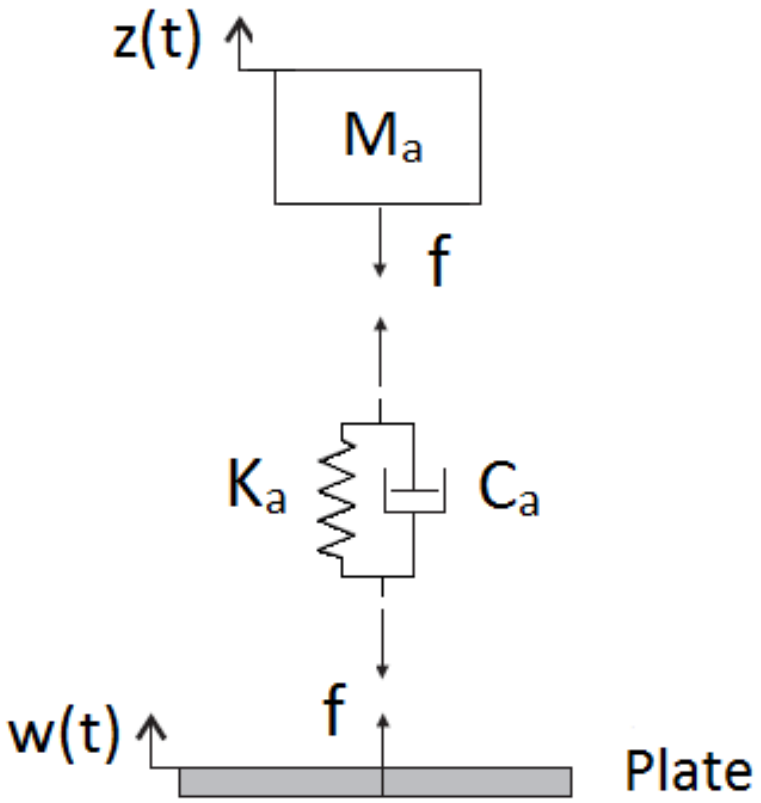

Figure 2.2: Lumped parameter actuator model

Now it is possible to introduce the dynamics related to the mechanical model of the inertial actuators.
Referring to the lumped parameter model presented in Figure 2.2, for each actuator i the following equation holds:

$$\begin{aligned} f_i &= K_{a_i}(z - w(\xi_{a_i}, \eta_{a_i}) - \delta_{c_i}) + C_{a_i}(\dot{z} - \dot{w}(\xi_{a_i}, \eta_{a_i})) = \\ &= K_{a_i}(z - w(\xi_{a_i}, \eta_{a_i})) + C_{a_i}(\dot{z} - \dot{w}(\xi_{a_i}, \eta_{a_i})) - K_{a_i}\delta_{c_i} = \\ &= K_{a_i}(z - w(\xi_{a_i}, \eta_{a_i})) + C_{a_i}(\dot{z} - \dot{w}(\xi_{a_i}, \eta_{a_i})) - f_{c_i} \end{aligned} \tag{2.18}$$

$z_i(t)$ is the absolute displacement of the proof mass, $\delta_{c_i}(t)$ is the elongation induced by the control force and $f_{c_i}(t)$ is the control force.
Moreover, the Newton's equation for each proof mass M_{a_i} holds:

$$f_i + M_{a_i}\ddot{z} = 0 \tag{2.19}$$

Substituting Equation (2.18) into Equation (2.19) the following equation for the mechanical model of the actuators is obtained:

$$M_{a_i}\ddot{z} + C_{a_i}\dot{z} + K_{a_i}z - C_{a_i}\dot{w}(\xi_{a_i}, \eta_{a_i}) - K_{a_i}w(\xi_{a_i}, \eta_{a_i}) = f_{c_i} \tag{2.20}$$

2.4 Coupling between plate and actuator models

The previous model of the plate with ideal point control forces and ideal sensors is here augmented by introducing sensor masses and actuator cases and coupling the obtained model to the actuator mechanical model.

Each sensor mass m_s and each actuator's case mass m_c can be modeled as point masses included into the plate model presented before, so a new mass matrix $\mathbf{M}_{p+s+c}$ will result :

$$\mathbf{M}_{p+s+c} = \mathbf{M}_p + \mathbf{M}_{sens} + \mathbf{M}_{case} \tag{2.21}$$

where

$$\mathbf{M}_{sens} = \sum_{i=1}^{N_{sa}} \mathbf{N}^T(\xi_{s_i}, \eta_{s_i}) m_s \mathbf{N}(\xi_{s_i}, \eta_{s_i}) \tag{2.22}$$

$$\mathbf{M}_{case} = \sum_{i=1}^{N_{sa}} \mathbf{N}^T(\xi_{a_i}, \eta_{a_i}) m_c \mathbf{N}(\xi_{a_i}, \eta_{a_i}) \tag{2.23}$$

Note that projecting this new mass matrix on the set of eigenvectors computed in Section 2.2 we will obtain no more an identity matrix.

Coupling between the plate model and the actuator model is now performed. After substituting Equation (2.18) into (2.12) and taking into account that

$$\mathbf{w}(\xi_{a_i}, \eta_{a_i}) = \mathbf{L}_{c_a}^T \mathbf{U}_L \mathbf{q}_L \tag{2.24}$$

the dynamic equations of the coupled model are obtained:

$$\mathbf{M} \begin{Bmatrix} \ddot{\mathbf{q}} \\ \ddot{\mathbf{z}} \end{Bmatrix} + \mathbf{C} \begin{Bmatrix} \dot{\mathbf{q}} \\ \dot{\mathbf{z}} \end{Bmatrix} + \mathbf{K} \begin{Bmatrix} \mathbf{q} \\ \mathbf{z} \end{Bmatrix} = \mathbf{B}_u \mathbf{f}_c + \mathbf{B}_d d \tag{2.25}$$

with

$$\mathbf{M} = \begin{bmatrix} \mathbf{U}_L^T \mathbf{M}_{p+s+c} \mathbf{U}_L & \mathbf{0} \\ \mathbf{0} & \mathbf{Diag}\{M_{a_i}\} \end{bmatrix}$$

$$\mathbf{C} = \begin{bmatrix} \mathbf{Diag}\{2\zeta_j \omega_j\} + \mathbf{U}_L^T \mathbf{L}_{c_a} \mathbf{Diag}\{C_{a_i}\} \mathbf{L}_{c_a}^T \mathbf{U}_L & -\mathbf{U}_L^T \mathbf{L}_{c_a} \mathbf{Diag}\{C_{a_i}\} \\ -\mathbf{Diag}\{C_{a_i}\} \mathbf{L}_{c_a}^T \mathbf{U}_L & \mathbf{Diag}\{C_{a_i}\} \end{bmatrix}$$

$$\mathbf{K} = \begin{bmatrix} \mathbf{Diag}\{\omega_j^2\} + \mathbf{U}_L^T \mathbf{L}_c \mathbf{Diag}\{K_{a_i}\} \mathbf{L}_{c_a}^T \mathbf{U}_L & -\mathbf{U}_L^T \mathbf{L}_{c_a} \mathbf{Diag}\{K_{a_i}\} \\ -\mathbf{Diag}\{K_{a_i}\} \mathbf{L}_{c_a}^T \mathbf{U}_L & \mathbf{Diag}\{K_{a_i}\} \end{bmatrix}$$

$$\mathbf{B}_u = \begin{bmatrix} -\mathbf{U}_L^T \mathbf{L}_{c_a} \\ \mathbf{I} \end{bmatrix}$$

$$\mathbf{B}_d = \begin{bmatrix} \mathbf{U}_L^T \mathbf{L}_d \\ \mathbf{0} \end{bmatrix}$$

A state space formulation of the model is written as:

$$\begin{Bmatrix} \dot{\mathbf{q}}_L \\ \dot{\mathbf{z}} \\ \ddot{\mathbf{q}}_L \\ \ddot{\mathbf{z}} \end{Bmatrix} = \mathbf{A}_p \begin{Bmatrix} \mathbf{q}_L \\ \mathbf{z} \\ \dot{\mathbf{q}}_L \\ \dot{\mathbf{z}} \end{Bmatrix} + \mathbf{B}_{up} \mathbf{f}_c + \mathbf{B}_{dp} d \tag{2.26}$$

with

$$\mathbf{A}_p = \begin{bmatrix} \mathbf{0} & \mathbf{I} \\ -\mathbf{M}^{-1}\mathbf{K} & -\mathbf{M}^{-1}\mathbf{C} \end{bmatrix}$$

$$\mathbf{B}_{up} = \begin{bmatrix} \mathbf{0} \\ \mathbf{M}^{-1}\mathbf{B}_u \end{bmatrix}$$

$$\mathbf{B}_{dp} = \begin{bmatrix} \mathbf{0} \\ \mathbf{M}^{-1}\mathbf{B}_d \end{bmatrix}$$

The output equation will be :

$$\mathbf{y}_p = \mathbf{C}_{yp} \begin{Bmatrix} \mathbf{q}_L \\ \mathbf{z} \\ \dot{\mathbf{q}}_L \\ \dot{\mathbf{z}} \end{Bmatrix} \tag{2.27}$$

with

$$\mathbf{C}_{yp} = \begin{bmatrix} \mathbf{0} & \mathbf{0} & \mathbf{L}_{c_s}\mathbf{U}_L & \mathbf{0} \end{bmatrix} \tag{2.28}$$

2.5 Integrator dynamics

In implementing velocity feedback control systems, the velocity signals can be obtained by proper integration of the accelerometer signals. Therefore, it is assumed that the plate is equipped with accelerometers. Accordingly, the output equation is modified as follows:

$$\mathbf{y}_p = \ddot{\mathbf{w}}(\xi_{si}, \eta_{si}) = \begin{bmatrix} \mathbf{0} & \mathbf{0} & \mathbf{L}_{c_s}\mathbf{U}_L & \mathbf{0} \end{bmatrix} \begin{Bmatrix} \dot{\mathbf{q}}_L \\ \dot{\mathbf{z}} \\ \ddot{\mathbf{q}}_L \\ \ddot{\mathbf{z}} \end{Bmatrix} \tag{2.29}$$

$$= \mathbf{C}_{yp} \begin{Bmatrix} \mathbf{q}_L \\ \mathbf{z} \\ \dot{\mathbf{q}}_L \\ \dot{\mathbf{z}} \end{Bmatrix} + \mathbf{D}_{up}\mathbf{f}_c + \mathbf{D}_{dp}d \tag{2.30}$$

with

$$\mathbf{C}_{yp} = \begin{bmatrix} \mathbf{0} & \mathbf{0} & \mathbf{L}_{c_s}\mathbf{U}_L & \mathbf{0} \end{bmatrix} \mathbf{A}_p$$

$$\mathbf{D}_{up} = \begin{bmatrix} \mathbf{0} & \mathbf{0} & \mathbf{L}_{c_s}\mathbf{U}_L & \mathbf{0} \end{bmatrix} \mathbf{B}_{up}$$

$$\mathbf{D}_{dp} = \begin{bmatrix} \mathbf{0} & \mathbf{0} & \mathbf{L}_{c_s}\mathbf{U}_L & \mathbf{0} \end{bmatrix} \mathbf{B}_{dp}$$

The model describing the dynamics of an integrator that provides velocities from acceleration measures is now introduced. It is possible to describe this block with the following transfer function:

$$y_{int_i} = \frac{s}{s^2 + 2\zeta_{int_i}\omega_{int_i}s + \omega_{int_i}^2} y_{p_i} \tag{2.31}$$

where y_{p_i} is the acceleration measure from sensor i and y_{int_i} is the corresponding integrator output (velocity). The cutoff frequency ω_{int_i} is selected in order to be a decade lower than the first natural frequency of the plate provided with real actuators. The state space representation is the following:

$$\begin{Bmatrix} \dot{\boldsymbol{\chi}} \\ \ddot{\boldsymbol{\chi}} \end{Bmatrix} = \mathbf{A}_{int} \begin{Bmatrix} \boldsymbol{\chi} \\ \dot{\boldsymbol{\chi}} \end{Bmatrix} + \mathbf{B}_{uint}\mathbf{y}_p \tag{2.32}$$

with

$$\mathbf{A}_{int} = \begin{bmatrix} \mathbf{0} & \mathbf{I} \\ -\mathbf{Diag}\{\omega_{int_i}^2\} & -\mathbf{Diag}\{2\zeta_{int_i}\omega_{int_i}\} \end{bmatrix}$$

$$\mathbf{B}_{uint} = \begin{bmatrix} \mathbf{0} \\ \mathbf{I} \end{bmatrix}$$

The output equation will be:

$$\mathbf{y}_{int} = \dot{\boldsymbol{\chi}} = \mathbf{C}_{yint} \begin{Bmatrix} \boldsymbol{\chi} \\ \dot{\boldsymbol{\chi}} \end{Bmatrix} \tag{2.33}$$

with

$$\mathbf{C}_{yint} = \begin{bmatrix} \mathbf{0} & \mathbf{I} \end{bmatrix}$$

2.6 Electrical dynamics of inertial actuators

Another block related to the electrical dynamics of the actuators is here introduced.
As stated in Griffin et al. [10], the electrical dynamics of the actuator can be modeled using a single Kirchhoff voltage law loop equation:

$$v_i = L\frac{di_i}{dt} + Ri_i + \psi(\dot{z} - \dot{w}(\xi_{a_i}, \eta_{a_i})) \tag{2.34}$$

where v_i are the control voltages, i_i are the control currents, L the inductance, R the DC resistance and ψ the force constant expressed in [N/A]. The relative motion between the two masses creates a feedback effect called back electromotive force (back-emf), which affects the force applied to the structure.
The control force applied by the actuator is given as

$$f_{c_i} = \psi i_i \tag{2.35}$$

Setting the currents as state variables, the state and the output equations of this model are:

$$\dot{\mathbf{x}}_{el} = -\frac{R}{L}\mathbf{x}_{el} - \frac{\psi}{L}(\dot{\mathbf{z}} - \mathbf{L}_{c_a}^T \mathbf{U}_L \dot{\mathbf{q}}) + \frac{1}{L}\mathbf{v} \tag{2.36}$$

$$\mathbf{y}_{el} = \mathbf{f}_c = \psi \mathbf{x}_{el} \tag{2.37}$$

2.6.1 Complete model

Coupling all the blocks presented before, the overall state space representation of the model is obtained:

$$\begin{Bmatrix} \dot{\mathbf{q}}_L \\ \dot{\mathbf{z}} \\ \ddot{\mathbf{q}}_L \\ \ddot{\mathbf{z}} \\ \dot{\boldsymbol{\chi}} \\ \ddot{\boldsymbol{\chi}} \\ \dot{\mathbf{x}}_{el} \end{Bmatrix} = \mathbf{A}_t \begin{Bmatrix} \mathbf{q}_L \\ \mathbf{z} \\ \dot{\mathbf{q}}_L \\ \dot{\mathbf{z}} \\ \boldsymbol{\chi} \\ \dot{\boldsymbol{\chi}} \\ \mathbf{x}_{el} \end{Bmatrix} + \mathbf{B}_{ut}\mathbf{v} + \mathbf{B}_{dt}\mathbf{d} \tag{2.38}$$

with

$$\mathbf{A}_t = \begin{bmatrix} \mathbf{A}_p & \mathbf{0} & \psi\mathbf{B}_{up} \\ \mathbf{B}_{uint}\mathbf{C}_{yp} & \mathbf{A}_{int} & \psi\mathbf{B}_{uint}\mathbf{D}_{up} \\ \begin{bmatrix}\mathbf{0} & \mathbf{0} & \frac{\psi}{L}\mathbf{L}_{c_a}^T\mathbf{U}_L & -\frac{\psi}{L}\mathbf{I}\end{bmatrix} & \mathbf{0} & -\frac{R}{L} \end{bmatrix}$$

$$\mathbf{B}_{ut} = \begin{bmatrix} \mathbf{0} \\ \mathbf{0} \\ \frac{1}{L}\mathbf{I} \end{bmatrix}$$

$$\mathbf{B}_{dt} = \begin{bmatrix} \mathbf{B}_{dp} \\ \mathbf{B}_{uint}\mathbf{D}_{dp} \\ \mathbf{0} \end{bmatrix}$$

The output equation is

$$\mathbf{y}_t = \mathbf{y}_{int} = \mathbf{C}_{yt} \begin{Bmatrix} \mathbf{q}_L \\ \mathbf{z} \\ \dot{\mathbf{q}}_L \\ \dot{\mathbf{z}} \\ \boldsymbol{\chi} \\ \dot{\boldsymbol{\chi}} \\ \mathbf{x}_{el} \end{Bmatrix} \tag{2.39}$$

with

$$\mathbf{C}_t = \begin{bmatrix} \mathbf{0} & \mathbf{C}_{yint} & \mathbf{0} \end{bmatrix}$$

Note that if a collocated sensor/actuator pattern is used, which means that sensors are placed in the same positions of actuators, the following relation holds:

$$\mathbf{L}_{c_s} = \mathbf{L}_{c_a}^T \tag{2.40}$$

and all the previous equations can be rewritten accordingly.

Chapter 3

Radiation model

For the purpose of estimating their sound radiation characteristics, many structures of practical interest may be modelled sufficiently accurately as rectangular, uniform, flat plates. For example, consider walls and floor of buildings, machinery casings, parts of vehicles, plane and satellite shells and hulls and bulkheads of ships. Even if it is not strictly correct to consider the modes of isolated panels when they are dynamically coupled to contiguous structures, the isolated rectuangular plate forms a useful starting point for modeling their radiation behavior.
The modeling of sound radiation of a plate in an infinite baffle is usually done in two ways, either by analyzing modal radiation or the so-called radiation modes. As the first approach is quite cumbersome, due to the need for computing a quadruple integral, the second technique is more appealing. This method is based on the so-called "radiation filters" and consists in using a modal expansion in order to calculate the overall radiated sound power as the summation of the contributions of each acoustic mode. In order to simplify further the model, a quite new method of reduced order modeling/design of radiation filters, termed Radiation Modal Expansion (RME), is presented.

3.1 Formulation in terms of Structural Modes

Referring to the book by Fahy and Gardonio [8] , the time-averaged total sound power radiation of a baffled plate can be evaluated by integrating the product of the surface sound pressure $p(x, y, 0, t)$ and the transverse velocity of the panel $\dot{w}(x, y, t)$ over the surface of a panel. For harmonic vibration,

$$\bar{P}(\omega) = \frac{1}{2} \int_0^a \int_0^b \mathrm{Re}\left(\dot{w}(x, y, \omega)^* p(x, y, 0, \omega)\right) \, dx \, dy \tag{3.1}$$

where $*$ denotes the complex conjugate. If analytical modes $\boldsymbol{\phi}(x, y)$ are provided, the transverse velocities of the plate $\dot{w}$ can be determined through mode shape terms:

$$\dot{w}(x, y) = \boldsymbol{\phi}(x, y)\mathbf{v} \tag{3.2}$$

$\mathbf{v}$ represent complex modal velocities amplitudes and $\boldsymbol{\phi}(x, y)$ represent normalised analytical mode shapes.
The surface acoustic pressure p can be written in terms of the normal surface velocity through the Rayleigh integral as

$$p(x, y, 0, \omega) = \frac{j\omega\rho_0}{2\pi} \int_0^a \int_0^b v(x', y', \omega) \frac{e^{-jkR}}{R} \, dx' \, dy' \tag{3.3}$$

where, $R = \sqrt{(x - x')^2 + (y - y')^2}$ is the distance between the point (x,y) where the sound pressure is evaluated and the vibrating point at (x', y'). Substituting Eq.(3.3) into Eq.(3.1), the time-average total sound power is given by the quadruple integral, which, using the modal expansion for $\dot{w}$, becomes

$$\begin{aligned} \bar{P}(\omega) = \frac{1}{2} Re\Big\{ \frac{j\omega\rho_0}{2\pi} \int_0^a \int_0^b \int_0^a \int_0^b \mathbf{v}^H \boldsymbol{\phi}(x, y)^T \\ \times \frac{e^{-jkR}}{R} \boldsymbol{\phi}(x', y')\mathbf{v} \Big\} \, dx' \, dy' \, dx \, dy \end{aligned} \tag{3.4}$$

where H denotes the Hermitian transpose (transpose and conjugate). Since $je^{-jkR}/R = j(\cos kR - j \sin kR)/R$, and because $\mathbf{v}^H\mathbf{v}$ is bound to be real positive, this expression can be rewritten as

$$\bar{P}(\omega) = \frac{\omega\rho_0}{4\pi}\mathbf{v}^H \left(\int_0^a \int_0^b \int_0^a \int_0^b \boldsymbol{\phi}(x,y)^T \frac{\sin kR}{R} \boldsymbol{\phi}(x',y')\, dx'\, dy'\, dx\, dy \right) \mathbf{v} \tag{3.5}$$

or, alternatively, in matrix form

$$\bar{P}(\omega) = \mathbf{v}^H \mathbf{A}(\omega) \mathbf{v} \tag{3.6}$$

where $\mathbf{A}$ is an $(n \times n)$ matrix (n represents the number of structural modes), which is normally referred to as the Power Transfer Matrix.

3.2 Formulation in terms of Elementary Radiators

Although the formulation presented above seems to be quite simple, the derivation of the quadruple integrals for the elements in the power transfer matrix $\mathbf{A}$ is relatively complex and cumbersome. An alternative approach based on the elementary radiators is therefore presented, as described by Fahy and Gardonio [8].

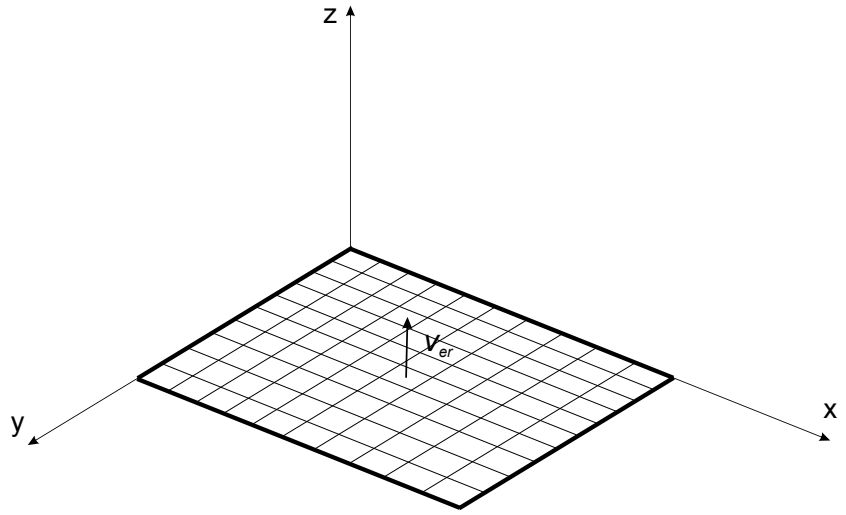

Figure 3.1: Subdivision of a panel into elementary radiators.

As shown in Figure 3.1, the baffled panel is divided into a grid of R small rectangular elements, called elementary radiators, whose transverse

vibrations are specified in terms of the velocities v_{er} at their center positions so that, assuming time-harmonic motion, the overall vibration of the panel can be described by the following column vector of complex amplitudes:

$$\mathbf{v}_e = [v_{e1} \quad v_{e2} \quad \dots \quad v_{eR}]^T \tag{3.7}$$

If the amplitudes of the sound pressures acting on each element are also grouped into a column vector as

$$\mathbf{p}_e = [p_{e1} \quad p_{e2} \quad \dots \quad p_{eR}]^T , \tag{3.8}$$

assuming that the dimensions of the elements are small compared with both the structural wavelength and the acoustic wavelength, the total radiated sound power can then be expressed as the summation of the powers radiated by each elementary radiator as follows

$$\bar{P}(\omega) = \sum_{r=1}^{R} \frac{1}{2} A_e \,\mathrm{Re}\,(v_{er}^* p_{er}) = \frac{S}{2R} \mathrm{Re}\left(\mathbf{v}_e^H \mathbf{p}_e\right) \tag{3.9}$$

where A_e and S are the area of each element and the whole panel, respectively. The pressure on each element is generated by the vibrations of all elements of the panel. Assuming that $\sqrt{A_e} \ll \lambda$, where λ is the acoustic wavelength, Equation (3.3) gives

$$p_{e_i}(x_i, y_i) = \frac{j\omega\rho_0 A_e e^{-jkR_{ij}}}{2\pi R_{ij}} v_{e_j}(x_j, y_j) \tag{3.10}$$

with R_{ij} the distance between the centers of the i-th and j-th elementary radiators. Therefore, the vector of sound pressures can be expressed by the impedance matrix relation

$$\mathbf{p}_e = \mathbf{Z}\mathbf{v}_e \tag{3.11}$$

where $\mathbf{Z}$ is the matrix incorporating the point and transfer acoustic impedence terms over the grid of elements into which the panel has been subdivided: $Z_{ij}(\omega) = (j\omega\rho_0 A_e/2\pi R_{ij})e^{-jkR_{ij}}$. Note that, because of reciprocity, the impedance matrix $\mathbf{Z}$ is symmetric, i.e., $\mathbf{Z} = \mathbf{Z}^T$.
Substituting Equation (3.11) into the expression for the total radiated sound power given in Equation (3.9), we obtain

$$\bar{P}(\omega) = \frac{S}{2R}\mathrm{Re}\left(\mathbf{v}_e^H \mathbf{Z}\mathbf{v}_e\right) \tag{3.12}$$

which, as $\mathbf{Z}$ is symmetric, can be rewritten as

$$\bar{P}(\omega) = \frac{S}{4R}\mathbf{v}_e^H\left(\mathbf{Z} + \mathbf{Z}^H\right)\mathbf{v}_e = \mathbf{v}_e^H \mathbf{R}\mathbf{v}_e \tag{3.13}$$

The matrix $\mathbf{R}$ is defined as the Radiation Resistance Matrix and for a baffled panel is given by

$$\begin{aligned}\mathbf{R} &= \frac{S}{2R}\mathrm{Re}\left(\mathbf{Z}\right) = \frac{S}{4R}\left(\mathbf{Z} + \mathbf{Z}^H\right) = \\ &= \frac{\omega^2\rho_0 A_e^2}{4\pi c}\begin{bmatrix} 1 & \frac{\sin(kR_{12})}{kR_{12}} & \cdots & \frac{\sin(kR_{1R})}{kR_{1R}} \\ \frac{\sin(kR_{21})}{kR_{21}} & 1 & & \\ \vdots & \cdots & \ddots & \cdots \\ \frac{\sin(kR_{R1})}{kR_{R1}} & & & 1 \end{bmatrix}\end{aligned} \tag{3.14}$$

where ω is the circular frequency in $[rad/s]$, ρ_0 is the density of the air, A_e is the area associated with the elementary radiator, c is the speed of sound in air, k is the wave number (ω/c), and R_{ij} is the distance between the center of the i-th and j-th velocity locations.
Since $R_{ij} = R_{ji}$, the radiation matrix is symmetric, and, as found for the power transfer matrix $\mathbf{A}$, it is also positive definite since the quadratic expression for the power radiation in Equation (3.13) is positive.

The agreement between Equation (3.5) and Equation (3.13) is generally good, provided that the dimensions of the discrete elements are much less than the acoustic wavelengths and the modal wavelengths in the panel.
In general, the modal approach can be used for regular shapes and common boundary conditions such that analytical expressions can be derived for the mode shapes. In the elementary radiator model, the velocities of the elementary radiators can be derived using general Ritz functions (or Finite Elements analysis), which enables the study of non-uniform, baffled plates of complex geometry having non-classic boundary conditions.

3.3 Independent Radiation Modes

In both the formulations presented in the previous section, the sound radiation due to the vibration of one structural mode or element is dependent

on the vibration of other structural modes or elements. Either of these formulations can be used to describe the sound power radiation in terms of a set of velocity distributions on the structure whose sound power radiation is independent from the amplitudes of the other velocity distributions. These velocity distributions are termed "radiation modes". Therefore, the sound radiation can be expressed in terms of a set of modes that radiate independently.
Referring to the formulation in terms of elementary radiators, a singular value decomposition can be performed on the matrix $\mathbf{R}$ to determine the dominant radiation modes of the system at each frequency. Singular value decomposition is performed at frequency ω_i as follows:

$$\mathbf{R}(\omega_i) = \mathbf{Y}\mathbf{\Sigma}\mathbf{Y}^{\mathbf{H}} \tag{3.15}$$

where $\mathbf{Y}$ is an $(R \times R)$ matrix whose columns are the normalized radiation modes of the matrix at frequency ω_i, and $\mathbf{\Sigma}$ is an $(R \times R)$ diagonal matrix whose elements are the singular values, decreasing monotonically along the diagonal. The magnitude fo the j-th diagonal element, σ_j, of $\mathbf{\Sigma}$ determines the relative importance of the j-th radiation mode compared to other radiation modes.

Substituting the singular value decomposition expression into Equation 3.13, the following expression for the total radiated sound power is obtained:

$$\bar{P}(\omega) = \mathbf{v}_e^H \mathbf{Y}\mathbf{\Sigma}\mathbf{Y}^H \mathbf{v}_e \tag{3.16}$$

Isolating the product between the eigenvector matrix $\mathbf{Y}$ and elemental radiator velocity vector $\mathbf{v}_e$, it is possible to write the vector

$$\mathbf{y} = \mathbf{Y}^H \mathbf{v}_e \tag{3.17}$$

Accordingly, Equation 3.16 becomes

$$\bar{P}(\omega) = \mathbf{y}^H \mathbf{\Sigma} \mathbf{y} = \sum_{r=1}^{R} \sigma_r \left| y_r \right|^2 \tag{3.18}$$

where R represents the number of elements. It is important to emphasise that, in general, the radiation modes are frequency dependent. Therefore, in order to predict the total power radiated over some bandwidth, the characteristics of the $\mathbf{R}$ matrix must be modeled over the bandwidth, fitting the trend of the singular values versus frequency to build the so-called Radiation

Filters model. This dynamic model is used to "filter" the discrete velocity measurements such that the rms sound power radiated from the structure can be estimated. Thus, for an $(R \times R)$ matrix, a total of R^2 transfer functions must be modeled. In order to avoid this high computational effort, a new method of reduced order modeling/design of radiation filters, termed Radiation Modal Expansion (RME), is presented.

3.4 Radiation Modal Expansion (RME)

The Radiation Modal Expansion (RME) is a special curve fitting technique, introduced by Gibbs et al. [9], which provides a reasonable approximation to the dynamics of the $\mathbf{R}$ matrix using a small fraction of the original number of states. This technique exploits the "nesting" property of the radiation modes: the space spanned by the significant radiating modes at frequency below some arbitrary maximum frequency of the bandwidth ω_{max} is a subspace of the space spanned by the radiating modes at the frequency ω_{max}. Thus, the set of singular vectors at ω_{max} corresponding to the significant radiating modes can be used as a basis to describe the radiation at any frequency below ω_{max}. The key to incorporating the essential physics of structural acoustic coupling rests in curve fitting the dominant radiating modes over the bandwidth, which is performed using the RME techinque outlined in this section. In this technique, the significant radiation modes at the upper frequency of the bandwidth of interest are used as a basis to curve fit the properties of the $\mathbf{R}$ matrix over the entire bandwidth. The amplitude-weighting coefficients $\Psi_i(\omega)$ are determined by the radiated power of each respective normalized radiation mode shape, at each frequency ω over the bandwidth, as follows:

$$\Psi_i^2(\omega) = \mathbf{Y}_{i,max}^H \mathbf{R}(j\omega)\mathbf{Y}_{i,max} \tag{3.19}$$

where $\Psi_i^2(\omega)$ is the radiated power of the i-th radiating mode (shape determined at ω_{max}), and $\mathbf{Y}_{i,max}$ is the i-th radiating mode shape determined at ω_{max}. A plot of the amplitude-weighting coefficients $\Psi_i(\omega)$ for the first six radiation modes of a simply supported aluminium plate (properties in Table 3.1) is shown in Fig. 3.2.

In order to create a model of the RME system it is only necessary to curve fit in frequency: the fitting of the Ψ_i considered is shown in Figure 3.3. Comparing the two figures do not notice visible differences between the trend of the model and the fitting, despite using relatively low order transfer functions: for the first 6 radiation modes, until 500 Hz, 3^{rd} order transfer

Property	Description	Value
a	x dimension	0.355 m
b	y dimension	0.254 m
ζ	Modal damping factor	0.001 m
h	Thickness	0.001 m
E	Young's Modulus	71 x 10^9 Pa
ρ	Density	2700 Kg/m^3
ν	Poisson's ratio	0.33

Table 3.1: Properties of the simply supported aluminium plate .

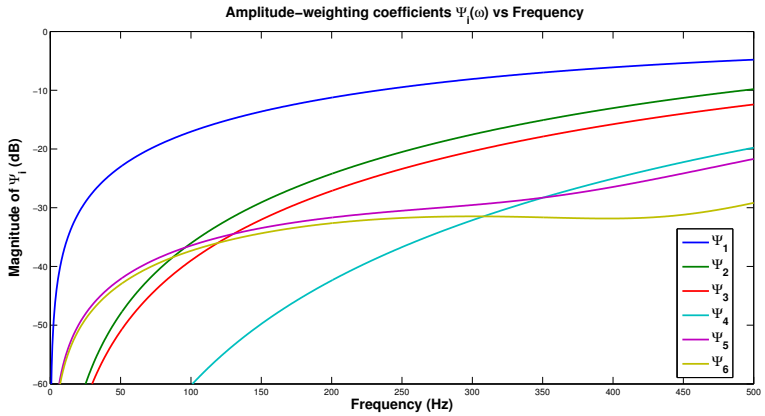

Figure 3.2: Radiation modal expansion coefficients (Ψ_i) for the first six radiation modes, up to 500 Hz.

functions are sufficient.

3.5 State space representation of the acoustic model

Performing the system realization based on the previous considerations, the following set of state space matrices for the radiation filters, one for each filter, is obtained:

$$\mathbf{A}_{rf} \quad \mathbf{B}_{rf} \quad \mathbf{C}_{rf} \quad \mathbf{D}_{rf} \tag{3.20}$$

In order to couple the radiation model with the structural model, the input to

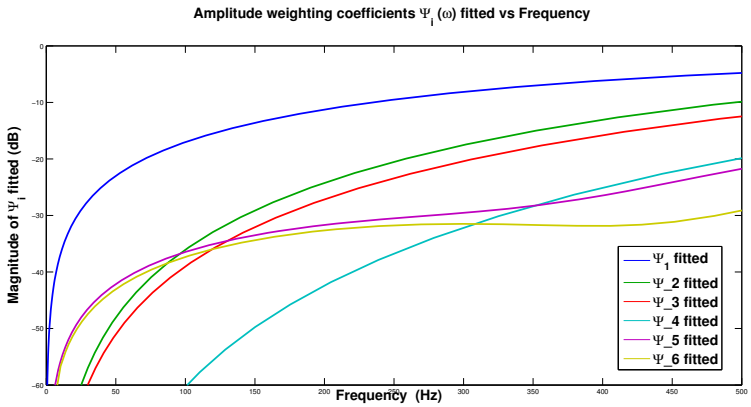

Figure 3.3: Fitting of the radiation modal expansion coefficients (Ψ_i) for the first six radiation modes, up to 500 Hz, with 3$^{\text{rd}}$ order radiation filters.

each radiation mode has to be calculated as a function of the modal velocities $\dot{\mathbf{q}}_L$ as:

$$\mathbf{v}_e = \mathbf{L}_{c_r}\mathbf{U}_L\dot{\mathbf{q}}_L(t) \tag{3.21}$$

where $\mathbf{L}_{c_r}$ is the matrix containing the Ritz functions evaluated in the coordinates of the center of each elementary radiator velocity (ξ_e, η_e) and $\mathbf{U}_L$ is the reduced set of structural modes (see Chapter 2).
At this point, applying the frequency dependent filters, the state space model for each radiation filter can be derived :

$$\begin{cases} \dot{\mathbf{a}}_{rfi} = \mathbf{A}_{rfi}\mathbf{a}_{rfi} + \mathbf{B}_{rfi}\mathbf{Y}_i^H\mathbf{L}_{c_r}\mathbf{U}_L\dot{\mathbf{q}}_L(t) \\ \mathbf{y}_{rfi} = \mathbf{C}_{rfi}\mathbf{a}_{rfi} + \mathbf{D}_{rfi}\mathbf{Y}_i^H\mathbf{L}_{c_r}\mathbf{U}_L\dot{\mathbf{q}}_L(t) \end{cases} \tag{3.22}$$

and then, incorporating all the radiation modes considered in the model, the representation becomes:

$$\begin{Bmatrix} \dot{\mathbf{a}}_{rf1} \\ \dot{\mathbf{a}}_{rf2} \\ \vdots \\ \dot{\mathbf{a}}_{rfN} \end{Bmatrix} = \underbrace{\begin{bmatrix} \mathbf{A}_{rf} & 0 & \dots & 0 \\ 0 & \mathbf{A}_{rf2} & & \vdots \\ \vdots & & \ddots & 0 \\ 0 & \dots & 0 & \mathbf{A}_{rfN} \end{bmatrix}}_{\mathbf{A}_{ac}} \begin{Bmatrix} \mathbf{a}_{rf1} \\ \mathbf{a}_{rf2} \\ \vdots \\ \mathbf{a}_{rfN} \end{Bmatrix} + \underbrace{\begin{bmatrix} \mathbf{B}_{rf1}\mathbf{Y}_1^H\mathbf{L}_{c_r}\mathbf{U}_L \\ \mathbf{B}_{rf2}\mathbf{Y}_2^H\mathbf{L}_{c_r}\mathbf{U}_L \\ \vdots \\ \mathbf{B}_{rfN}\mathbf{Y}_N^H\mathbf{L}_{c_r}\mathbf{U}_L \end{bmatrix}}_{\mathbf{B}_{ac}} \dot{\mathbf{q}}_L \tag{3.23}$$

$$\mathbf{y_{ac}} = \begin{Bmatrix} \mathbf{y}_{rf1} \\ \mathbf{y}_{rf2} \\ \vdots \\ \mathbf{y}_{rfN} \end{Bmatrix} \underbrace{\begin{bmatrix} \mathbf{C}_{rf} & 0 & \dots & 0 \\ 0 & \mathbf{C}_{rf2} & & \vdots \\ \vdots & & \ddots & 0 \\ 0 & \dots & 0 & \mathbf{C}_{rfN} \end{bmatrix}}_{\mathbf{C}_{ac}} \begin{Bmatrix} \mathbf{a}_{rf1} \\ \mathbf{a}_{rf2} \\ \vdots \\ \mathbf{a}_{rfN} \end{Bmatrix} + \underbrace{\begin{bmatrix} \mathbf{D}_{rf1}\mathbf{Y}_1^H\mathbf{L}_{c_r}\mathbf{U}_L \\ \mathbf{D}_{rf2}\mathbf{Y}_2^H\mathbf{L}_{c_r}\mathbf{U}_L \\ \vdots \\ \mathbf{D}_{rfN}\mathbf{Y}_N^H\mathbf{L}_{c_r}\mathbf{U}_L \end{bmatrix}}_{\mathbf{D}_{ac}} \dot{\mathbf{q}}_L \tag{3.24}$$

It can be written in a more compact form as follows:

$$\begin{cases} \dot{\mathbf{a}}_{ac} = \mathbf{A}_{ac}\mathbf{a}_{ac} + \mathbf{B}_{ac}\dot{\mathbf{q}}_L \\ \mathbf{y}_{ac} = \mathbf{C}_{ac}\mathbf{a}_{ac} + \mathbf{D}_{ac}\dot{\mathbf{q}}_L \end{cases} \tag{3.25}$$

where $\mathbf{a}_{ac}$ are the states of the radiation filters. $\mathbf{B_{ac}}$ describes the excitation of the filters as a function of the modal velocities, $\mathbf{A_{ac}}$ describes the dynamics, $\mathbf{C_{ac}}$ describes the relation between the states of each filter and its output and $\mathbf{D_{ac}}$ is a direct feedthrough matrix of the structural modal velocities.

3.6 Global state space representation

An efficient way to simultaneously deal with the structural and the acoustic model, as they are coupled, is embedding them in a global state space representation with a state vector which includes structural modes and acoustic modes.

$$\begin{Bmatrix} \dot{\mathbf{q}}_L \\ \dot{\mathbf{z}} \\ \ddot{\mathbf{q}}_L \\ \ddot{\mathbf{z}} \\ \dot{\boldsymbol{\chi}} \\ \ddot{\boldsymbol{\chi}} \\ \dot{\mathbf{x}}_{el} \\ \dot{\mathbf{a}}_{ac} \end{Bmatrix} = \mathbf{A} \begin{Bmatrix} \mathbf{q}_L \\ \mathbf{z} \\ \dot{\mathbf{q}}_L \\ \dot{\mathbf{z}} \\ \boldsymbol{\chi} \\ \dot{\boldsymbol{\chi}} \\ \mathbf{x}_{el} \\ \mathbf{a}_{ac} \end{Bmatrix} + \mathbf{B}_u\mathbf{v} + \mathbf{B}_d\mathbf{d} \tag{3.26}$$

with

$$\mathbf{A} = \begin{bmatrix} & & \mathbf{A}_t & & & & & \mathbf{0} \\ \begin{bmatrix} \mathbf{0} & \mathbf{0} & \mathbf{B}_{ac} & \mathbf{0} & \mathbf{0} & \mathbf{0} & \mathbf{0} \end{bmatrix} & & & & & & & \mathbf{A}_{ac} \end{bmatrix}$$

$$\mathbf{B}_u = \begin{bmatrix} \mathbf{B}_{ut} \\ \mathbf{0} \end{bmatrix}$$

$$\mathbf{B}_d = \begin{bmatrix} \mathbf{B}_{dt} \\ \mathbf{0} \end{bmatrix}$$

The output equation of the structural model (velocities) is

$$\mathbf{y}_s = \mathbf{C}_{ys} \begin{Bmatrix} \mathbf{q}_L \\ \mathbf{z} \\ \dot{\mathbf{q}}_L \\ \dot{\mathbf{z}} \\ \boldsymbol{\chi} \\ \dot{\boldsymbol{\chi}} \\ \mathbf{x}_{el} \\ \mathbf{a}_{ac} \end{Bmatrix} \tag{3.27}$$

with

$$\mathbf{C}_{ys} = \begin{bmatrix} \mathbf{C}_{yt} & \mathbf{0} \end{bmatrix}$$

The output equation of the radiation model (radiated acoustic power) is

$$\mathbf{y}_{ac} = \mathbf{C}_{yac} \begin{Bmatrix} \mathbf{q}_L \\ \mathbf{z} \\ \dot{\mathbf{q}}_L \\ \dot{\mathbf{z}} \\ \boldsymbol{\chi} \\ \dot{\boldsymbol{\chi}} \\ \mathbf{x}_{el} \\ \mathbf{a}_{ac} \end{Bmatrix} \tag{3.28}$$

with

$$\mathbf{C}_{yac} = \begin{bmatrix} \mathbf{0} & \mathbf{0} & \mathbf{D}_{ac} & \mathbf{0} & \mathbf{0} & \mathbf{0} & \mathbf{0} & \mathbf{C}_{ac} \end{bmatrix}$$

Chapter 4

Control strategy

A modern method of designing an active control for a LTI system is to use a state-space design technique. Probably the most common design procedure is the so-called steady-state optimal linear quadratic control or linear quadratic regulator (LQR). The LQR problem is formulated assuming a stabilizing linear state feedback law with constant gain matrix

$$\mathbf{u}(t) = -\mathbf{G}\mathbf{x}(t) \tag{4.1}$$

and selecting the gain matrix $\mathbf{G}$ such that a properly defined quadratic cost functional is minimized. If we are dealing with a stochastic response, the cost function to minimize is represented by the expected value of the quadratic forms associated with performance and control. It can be written as:

$$J = E\left[\mathbf{z}(\mathbf{t})^T \mathbf{W}_{zz}\mathbf{z}(t) + \mathbf{u}(\mathbf{t})^T \mathbf{W}_{uu}\mathbf{u}(t)\right] \tag{4.2}$$

where

- $\mathbf{z}(t)$ is a selected performance vector.
- $\mathbf{W}_{zz}$ is a nonnegative symmetric weighting matrix ($\mathbf{W}_{zz} \geq 0$) associated with the performance.
- $\mathbf{W}_{uu}$ is a positive definite symmetric weighting matrix related to the control effort $\mathbf{u}(t)$.

It is noted that the cost functional contains two contributions. The first is the quadratic form $\mathbf{z}(\mathbf{t})^T \mathbf{W}_{zz}\mathbf{z}(t)$, which represents the penalty on the deviation of the performance vector $\mathbf{z}$ from the origin. The second quadratic

form $\mathbf{u(t)}^T\mathbf{W}_{uu}\mathbf{u}(t)$ represents the cost of control and is included in order to limit the magnitude of the control variables. In most practical cases, the control weighting matrix is selected large enough to avoid saturation of the actuators under nominal conditions of operation. The weighting matrices can be used to specify the relative importance of the various components of the performance vector and the control input vector.

A similar approach that avoids completely the need of reconstructing the state vector is based on the direct feedback of the output vector $\mathbf{y}(t)$ instead of the full state $\mathbf{x(t)}$. This approach is called Direct Output Optimal Control or Suboptimal control. It is based on the following feedback law:

$$\mathbf{u}(t) = -\mathbf{G}\mathbf{y}(t) \tag{4.3}$$

where $\mathbf{G}$ is the unknown gain matrix and $\mathbf{y}(t)$ is the set of output measurements.

Let's consider the open-loop dynamics written as

$$\dot{\mathbf{x}} = \mathbf{A}\mathbf{x} + \mathbf{B}_u\mathbf{u} + \mathbf{B}_d\mathbf{d} \tag{4.4}$$
$$\mathbf{y} = \mathbf{C}_y\mathbf{x} \tag{4.5}$$

and the performance vector can be expressed as follows

$$\mathbf{z}(t) = \mathbf{C}_z\mathbf{x} \tag{4.6}$$

Substituting Equation 4.6 into Equation 4.5 the following expression of $\mathbf{J}$ is obtained

$$J = E\left[\mathbf{x}^T\mathbf{W}(\mathbf{G})\mathbf{x}\right] \tag{4.7}$$

where

$$\mathbf{W}(\mathbf{G}) = \mathbf{C}_z^T\mathbf{W}_{zz}\mathbf{C}_z + \mathbf{C}_y^T\mathbf{G}^T\mathbf{W}_{uu}\mathbf{G}\mathbf{C}_y \tag{4.8}$$

In the next section the selection of the performance variables and the minimization of the cost function J will be discussed.

4.1 Definition of the performance variables

Depending on the type of minimization to be performed, a suitable performance term in the expression of the cost function J has to be chosen. As the aim of the active vibration control is to suppress vibrations all over a certain bandwidth, a global quantity like kinetic energy is a good index to be minimized in order to obtain an overall damping of every mode considered. The same consideration holds for the radiated sound power in order to suppress noise. Therefore, kinetic energy and radiated sound power will be the performance indeces to be minimized for the AVC and ASAC problems, respectively.

Referring to Chapter 2 for the notation, the kinetic energy of the plate can be computed as:

$$\begin{aligned} E_k &= \frac{1}{2}\int_0^a \int_0^b \rho h \dot{w}(x,y)^2 \, dA = \\ &= \frac{1}{2}\frac{\rho h a b}{4}\int_0^1 \int_0^1 \dot{w}(\xi,\eta)^2 \, d\xi \, d\eta = \\ &= \frac{1}{2}\frac{\rho h a b}{4}\int_0^1 \int_0^1 \dot{\mathbf{u}}^T \mathbf{N}^T \mathbf{N} \dot{\mathbf{u}} \, d\xi \, d\eta = \\ &= \frac{1}{2}\dot{\mathbf{q}}_L^T \mathbf{U}_L^T \frac{\rho h a b}{4}\int_0^1 \int_0^1 \mathbf{N}^T \mathbf{N} \, d\xi \, d\eta \, \mathbf{U}_L \dot{\mathbf{q}}_L = \\ &= \frac{1}{2}\dot{\mathbf{q}}_L^T \mathbf{U}^T \mathbf{M_p} \mathbf{U} \dot{\mathbf{q}}_L \end{aligned} \tag{4.9}$$

So, for the chosen mode shape rapresentation, as the matrix $\mathbf{U}_L$ contains mass-normalized eigenvectors, the expression for the kinetic energy will be:

$$E_k = \frac{1}{2}\dot{\mathbf{q}}_L^T(t)\dot{\mathbf{q}}_L(t) \tag{4.10}$$

If the kinetic energy is selected as performance index, the following relation holds:

$$E_k = \frac{1}{2}\begin{Bmatrix} \dot{\mathbf{q}}_L \\ \dot{\mathbf{z}} \\ \ddot{\mathbf{q}}_L \\ \ddot{\mathbf{z}} \\ \dot{\boldsymbol{\chi}} \\ \ddot{\boldsymbol{\chi}} \\ \dot{\mathbf{x}}_{el} \end{Bmatrix}^T \mathbf{C}_z^T \mathbf{W}_{zz} \mathbf{C}_z \begin{Bmatrix} \mathbf{q}_L \\ \mathbf{z} \\ \dot{\mathbf{q}}_L \\ \dot{\mathbf{z}} \\ \boldsymbol{\chi} \\ \dot{\boldsymbol{\chi}} \\ \mathbf{x}_{el} \end{Bmatrix} \tag{4.11}$$

If $\mathbf{W}_{zz} = \mathbf{I}$,

$$\mathbf{C}_z = \begin{bmatrix} \mathbf{0} & \mathbf{0} & \mathbf{I} & \mathbf{0} & \mathbf{0} & \mathbf{0} & \mathbf{0} \end{bmatrix} \tag{4.12}$$

If the radiated sound power is used as performance variable, consider the expression for the output equation obtained in Chapter 3:

$$\mathbf{y}_{ac} = \mathbf{C}_{yac} \begin{Bmatrix} \mathbf{q}_L \\ \mathbf{z} \\ \dot{\mathbf{q}}_L \\ \dot{\mathbf{z}} \\ \boldsymbol{\chi} \\ \dot{\boldsymbol{\chi}} \\ \mathbf{x}_{el} \end{Bmatrix} \tag{4.13}$$

with

$$\mathbf{C}_{yac} = \begin{bmatrix} \mathbf{0} & \mathbf{0} & \mathbf{D}_{ac} & \mathbf{0} & \mathbf{0} & \mathbf{0} & \mathbf{0} & \mathbf{C}_{ac} \end{bmatrix}$$

The radiated sound power will be

$$P_{rad} = \mathbf{y}_{\mathbf{ac}}^{\mathbf{T}}(t)\mathbf{y}_{\mathbf{ac}}(t) \tag{4.14}$$

and C_z matrix will be

$$\mathbf{C}_z = C_{yac} \tag{4.15}$$

4.2 Minimization problem

Referring back to Equation 4.7, the cost functional J can be also expressed by taking the trace without changing the result:

$$J = Tr\left\{E\left[\mathbf{x}^T\mathbf{W}(\mathbf{G})\mathbf{x}\right]\right\} \tag{4.16}$$

Since the trace and the expected value are linear operators, after few manipulations using the properties of the trace the following expression for the cost function is obtained:

$$J = Tr\left[\mathbf{W}(\mathbf{G})\boldsymbol{\sigma}_{xx}^2\right] \tag{4.17}$$

Therefore, the minimization of J implies the minimization of the variance matrix of the state vector $\boldsymbol{\sigma}_{xx}^2$. We know that $\boldsymbol{\sigma}_{xx}^2$ must satisfy the following Lyapunov equation corresponding to the closed-loop dynamics

$$\mathbf{A}_c\boldsymbol{\sigma}_{xx}^2 + \boldsymbol{\sigma}_{xx}^2\mathbf{A}_c^T + \mathbf{B}_d\mathbf{W}_{dd}\mathbf{B}_d^T = 0 \tag{4.18}$$

where

$$\mathbf{A}_c = \mathbf{A} - \mathbf{B}_u\mathbf{G}\mathbf{C}_y \tag{4.19}$$

is the closed-loop state matrix and $\mathbf{W}_{dd}$ is the matrix of intensities of the white noise disturbances. The above equation represents the constraint equation of the minimization process. An unconstrained minimization can be carried out if we introduce into J the constraint equation using the Lagrange multipliers. Therefore, the cost functional to be minimized is rewritten as

$$J = Tr\left[\mathbf{W}(\mathbf{G})\boldsymbol{\sigma}_{xx}^2 + \boldsymbol{\Lambda}(\mathbf{A}_c\boldsymbol{\sigma}_{xx}^2 + \boldsymbol{\sigma}_{xx}^2\mathbf{A}_c^T + \mathbf{B}_d\mathbf{W}_{dd}\mathbf{B}_d^T)\right] \tag{4.20}$$

where $\boldsymbol{\Lambda}$ is the symmetric matrix of Lagrange multipliers. Since we have three unknown matrices, $\boldsymbol{\Lambda}$, $\boldsymbol{\sigma}_{xx}^2$ and $\mathbf{G}$, the minimization of J implies that

$$\frac{\partial J}{\partial \boldsymbol{\Lambda}} = 0 \tag{4.21}$$

$$\frac{\partial J}{\partial \boldsymbol{\sigma}_{xx}^2} = 0 \tag{4.22}$$

$$\frac{\partial J}{\partial \mathbf{G}} = 0 \tag{4.23}$$

Performing these partial derivatives, the following equations are obtained:

$$(\mathbf{A} - \mathbf{B}_u\mathbf{G}\mathbf{C}_y)\boldsymbol{\sigma}_{xx}^2 + \boldsymbol{\sigma}_{xx}^2(\mathbf{A} - \mathbf{B}_u\mathbf{G}\mathbf{C}_y)^T + \mathbf{B}_d\mathbf{W}_{dd}\mathbf{B}_d^T = 0 \tag{4.24}$$

$$(\mathbf{A} - \mathbf{B}_u\mathbf{G}\mathbf{C}_y)^T\boldsymbol{\Lambda} + \boldsymbol{\Lambda}(\mathbf{A} - \mathbf{B}_u\mathbf{G}\mathbf{C}_y) + \mathbf{W}(\mathbf{G}) = 0 \tag{4.25}$$

$$\mathbf{G} = \mathbf{W}_{uu}^{-1}\mathbf{B}_u^T\boldsymbol{\Lambda}\boldsymbol{\sigma}_{xx}^2\mathbf{C}_y^T(\mathbf{C}_y\boldsymbol{\sigma}_{xx}^2\mathbf{C}_y^T)^{-1} \tag{4.26}$$

Accordingly, if a static output feedback law is assumed, the expression of the gain matrix $\mathbf{G}$ contains two unknown matrices $\boldsymbol{\sigma}_{xx}^2$ and $\boldsymbol{\Lambda}$. Such matrices satisfy Lyapunov equations, which in turn contain the unknown gain matrix. Consequently, the overall solution involves a fully coupled set of nonlinear matrix equations.

Instead of relying on a numerical solution of the previous set, a gradient-based optimization on the cost function expressed in Equation 4.17 can be employed. Once provided an expression of the cost functional $J(\mathbf{x})$ (where $\mathbf{x}$ is the vector of variables with respect to which perform the minimization), an initial guess vector $\mathbf{x}_0$ and a gradient, the optimization problem is written as

$$\min J(\mathbf{X}) \rightarrow \mathbf{X}^* \tag{4.27}$$

where $\mathbf{X}^*$ are the optimum values that minimize J.
In our specific case, J is the cost functional defined in Equation (4.17) and $\mathbf{X}$ is

- a vector with the components g_{ik} of the gain matrix if an optimization of the gains in performed;

- a vector containing the components g_{ik} of the gain matix, the placements of sensors $\mathbf{X}_s$ and the placements of actuators $\mathbf{X}_a$ if an optimization in terms of gains and actuator/sensor positions is desired.

For this purpose an analytical expression of the gradient of J with respect to the optimization variables must be provided.

4.3 Gradient definition

4.3.1 Gain optimization

If an optimization in terms of the elements of the gain matrix is desired, then an expression for the gradient $\frac{\partial J}{\partial \mathbf{G}}$ must be provided. The gradient is computed as following:

$$\frac{\partial \mathbf{J}}{\partial g_{ik}} = Tr\,[\frac{\partial \mathbf{W}(\mathbf{G})}{\partial g_{ik}}\boldsymbol{\sigma}^2_{xx} + \mathbf{W}(\mathbf{G})\frac{\partial \boldsymbol{\sigma}^2_{xx}}{\partial g_{ik}}] = \tag{4.28}$$

$$= Tr\,[\frac{\partial \mathbf{W}(\mathbf{G})}{\partial g_{ik}}\boldsymbol{\sigma}^2_{xx} - (\boldsymbol{\Lambda}\mathbf{A}_c + \mathbf{A}_c^T\boldsymbol{\Lambda})\frac{\partial \boldsymbol{\sigma}^2_{xx}}{\partial g_{ik}}] = \tag{4.29}$$

$$= Tr\,[\frac{\partial \mathbf{W}(\mathbf{G})}{\partial g_{ik}}\boldsymbol{\sigma}^2_{xx} - \boldsymbol{\Lambda}(\mathbf{A}_c\frac{\partial \boldsymbol{\sigma}^2_{xx}}{\partial g_{ik}} + \frac{\partial \boldsymbol{\sigma}^2_{xx}}{\partial g_{ik}}\mathbf{A}_c^T)] = \tag{4.30}$$

$$= Tr\,[\frac{\partial \mathbf{W}(\mathbf{G})}{\partial g_{ik}}\boldsymbol{\sigma}^2_{xx} + \boldsymbol{\Lambda}(\frac{\partial \mathbf{A}_c}{\partial g_{ik}}\boldsymbol{\sigma}^2_{xx} + \boldsymbol{\sigma}^2_{xx}\frac{\partial \mathbf{A}_c^T}{\partial g_{ik}})] = \tag{4.31}$$

$$= Tr\,[\boldsymbol{\sigma}^2_{xx}\frac{\partial \mathbf{W}(\mathbf{G})}{\partial g_{ik}} + 2\boldsymbol{\sigma}^2_{xx}\frac{\partial \mathbf{A}_c}{\partial g_{ik}}^T\boldsymbol{\Lambda}] \tag{4.32}$$

4.3.2 Positions optimization

If, in addition to the gain optimization, a position optimization is desired, an expression for the gradient of J with respect to the coordinates of the locations of sensors (ξ_{s_i}, η_{s_i}) and actuators (ξ_{a_i}, η_{a_i}) must be provided, as proposed by Xu et al. [12]. It is possible to compute this gradient analitically deriving the functional J with respect to the state space matrices of the model and then deriving the latter with respect the position variables. Then, the following chain rule equation can be exploited:

$$\frac{\partial J(\mathbf{A})}{\partial x} = Tr\,[(\frac{\partial J(\mathbf{A})}{\partial A_{ij}}^T\frac{\partial \mathbf{A}}{\partial x}] \tag{4.33}$$

where J is a generic functional, $\mathbf{A}$ a generic matrix and x a generic variable.

The derivatives of the cost function J with respect to the state space model matrices are here derived. Expanding Equation 4.20 yields

$$\begin{aligned} J = Tr\,[&\mathbf{C}_z^T\mathbf{W}_{zz}\mathbf{C}_z\boldsymbol{\sigma}^2_{xx} + \mathbf{C}_y^T\mathbf{G}^T\mathbf{R}\mathbf{G}\mathbf{C}_y\boldsymbol{\sigma}^2_{xx} + \\ &\boldsymbol{\Lambda}\mathbf{A}\boldsymbol{\sigma}^2_{xx} - \boldsymbol{\Lambda}\mathbf{B}_u\mathbf{G}\mathbf{C}_y\boldsymbol{\sigma}^2_{xx} + \boldsymbol{\Lambda}\boldsymbol{\sigma}^2_{xx}\mathbf{A}^T \\ &- \boldsymbol{\Lambda}\boldsymbol{\sigma}^2_{xx}\mathbf{C}_y^T\mathbf{G}^T\mathbf{B}_u^T + \boldsymbol{\Lambda}\mathbf{B}_d\mathbf{W}_{dd}\mathbf{B}_d^T)] \end{aligned} \tag{4.34}$$

Exploiting the properties of the trace, the derivatives of the cost function with respect to the matrices $\mathbf{A}$, $\mathbf{B}_u$, $\mathbf{C}_y$ and $\mathbf{B}_d$ can be computed as:

$$\frac{\partial J}{\partial \mathbf{A}} = 2\mathbf{\Lambda}\boldsymbol{\sigma}_{xx}^2 \tag{4.35}$$

$$\frac{\partial J}{\partial \mathbf{B}_u} = -2\mathbf{\Lambda}\boldsymbol{\sigma}_{xx}^2\mathbf{C}_y^T\mathbf{G}^T \tag{4.36}$$

$$\frac{\partial J}{\partial \mathbf{C}_y} = -2\mathbf{G}^T\mathbf{B}_u^T\mathbf{\Lambda}\boldsymbol{\sigma}_{xx}^2 + 2\mathbf{G}^T\mathbf{R}\mathbf{G}\mathbf{C}_y\boldsymbol{\sigma}_{xx}^2 \tag{4.37}$$

$$\frac{\partial J}{\partial \mathbf{B}_d} = 2\mathbf{\Lambda}\mathbf{W}_{dd}\mathbf{B}_d \tag{4.38}$$

According to the model under study (ideal or including sensor/actuator dynamics), actuator and sensor positions appear in different matrices of the selected state-space form.

Ideal case In the ideal case, the positions (ξ_{a_i}, η_{a_i}) and (ξ_{s_i}, η_{s_i}) are included in the matrices $\mathbf{B}_{up}$ and $\mathbf{C}_{yp}$, respectively (see Chapter 2). The following two derivatives with respect to ξ_i coordinates can be computed:

$$\frac{\partial \mathbf{B}_u}{\partial \xi_{a_i}} = \begin{bmatrix} \mathbf{0} \\ \mathbf{U}_L^T \frac{\partial \mathbf{L}_{c_a}}{\partial \xi_{a_i}} \end{bmatrix} \tag{4.39}$$

$$\frac{\partial \mathbf{C}_y}{\partial \xi_{s_i}} = \begin{bmatrix} \mathbf{0} & \frac{\partial \mathbf{L}_{c_s}}{\partial \xi_{s_i}}\mathbf{U}_L \end{bmatrix} \tag{4.40}$$

$\mathbf{L}_{c_a}$ and $\mathbf{L}_{c_s}$ contain the Ritz functions evaluated at the actuator and sensor positions (see Chapter 2). So each element of the derivatives $\frac{\partial \mathbf{L}_{c_a}}{\partial \xi_{a_i}}$ and $\frac{\partial \mathbf{L}_{c_s}}{\partial \xi_{s_i}}$ can be computed as:

$$\begin{aligned} \frac{\partial L_{c_a}(m \cdot n, i)}{\xi_{a_i}} = \sum_{m=1}^{M}\sum_{n=1}^{N} \{ & a_m[\cos(a_m\xi_{a_i} + b_m)\sin(c_m\xi_{a_i} + d_m)] \\ & + c_m[\cos(c_m\xi_{a_i} + d_m)\sin(a_m\xi_{a_i} + b_m)]\} \\ & \times \sin(a_n\eta_{a_i} + b_n)\sin(c_n\eta_{a_i} + d_n) \end{aligned} \tag{4.41}$$

and

$$\frac{\partial L_{c_s}(i, m \cdot n)}{\xi_{s_i}} = \sum_{m=1}^{M}\sum_{n=1}^{N}\{a_m[\cos(a_m\xi_{s_i} + b_m)\sin(c_m\xi_{s_i} + d_m)] + c_m[\cos(c_m\xi_{s_i} + d_m)\sin(a_m\xi_{s_i} + b_m)]\} \times \sin(a_n\eta_{s_i} + b_n)\sin(c_n\eta_{s_i} + d_n) \quad (4.42)$$

Exploiting Equation 4.33 , the following expressions are obtained for the present case:

$$\frac{\partial J}{\partial \xi_{a_i}} = Tr[(\frac{\partial J}{\partial \mathbf{B}_{up}})^T \frac{\partial \mathbf{B}_{up}}{\partial \xi_{a_i}}] \quad (4.43)$$

$$\frac{\partial J}{\partial \xi_{s_i}} = Tr[(\frac{\partial J}{\partial \mathbf{C}_{yp}})^T \frac{\partial \mathbf{C}_{yp}}{\partial \xi_{s_i}}] \quad (4.44)$$

The same equations holds considering η_i coordinates. $\frac{\partial \mathbf{L}_{c_a}}{\partial \eta_{a_i}}$ and $\frac{\partial \mathbf{L}_{c_s}}{\partial \eta_{s_i}}$ can be computed as:

$$\frac{\partial L_{c_a}(m \cdot n, i)}{\eta_{a_i}} = \sum_{m=1}^{M}\sum_{n=1}^{N}\{a_n[\cos(a_n\eta_{a_i} + b_n)\sin(c_n\eta_{a_i} + d_n)] + c_n[\cos(c_n\eta_{a_i} + d_n)\sin(a_n\eta_{a_i} + b_n)]\} \times \sin(a_m\xi_{a_i} + b_m)\sin(c_m\xi_{a_i} + d_m) \quad (4.45)$$

and

$$\frac{\partial L_{c_s}(i, m \cdot n)}{\eta_{s_i}} = \sum_{m=1}^{M}\sum_{n=1}^{N} a_n[\cos(a_n\eta_{s_i} + b_n)\sin(c_n\eta_{s_i} + d_n)] + c_n[\cos(c_n\eta_{s_i} + d_n)\sin(a_n\eta_{s_i} + b_n)]\} \times \sin(a_m\xi_{s_i} + b_m)\sin(c_m\xi_{s_i} + d_m) \quad (4.46)$$

If a collocated sensor/actuator pattern is considered the previous equations remain valid with

$$\mathbf{L}_{c_s} = \mathbf{L}_{c_a}^T \tag{4.47}$$

$$\frac{\partial \mathbf{L}_{c_s}}{\partial \xi_i} = \frac{\partial \mathbf{L}_{c_a}}{\partial \xi_i}^T \tag{4.48}$$

$$\frac{\partial \mathbf{L}_{c_s}}{\partial \eta_i} = \frac{\partial \mathbf{L}_{c_a}}{\partial \eta_i}^T \tag{4.49}$$

and the gradient of J with respect to the coordinates ξ_i and η_i is computed summing up the derivatives 4.43 and 4.44.

Complete model In the case the model includes all the dynamic effects described in Chapter 2, the dependency on ξ_i and η_i is contained in matrices $\mathbf{A}_t$ and $\mathbf{B}_{dt}$ and the following derivatives are computed:

$$\frac{\partial \mathbf{A}_t}{\partial \xi_{a_i}} = \begin{bmatrix} \begin{bmatrix} \mathbf{0} & \mathbf{0} \\ -\frac{\partial \mathbf{M}^{-1}}{\partial \xi_{a_i}}\mathbf{K} - \mathbf{M}^{-1}\frac{\partial \mathbf{K}}{\partial \xi_{a_i}} & -\frac{\partial \mathbf{M}^{-1}}{\partial \xi_i}\mathbf{C} - \mathbf{M}^{-1}\frac{\partial \mathbf{C}}{\partial \xi_{a_i}} \end{bmatrix} & \begin{matrix} \mathbf{0} & \psi\frac{\partial \mathbf{B}_{up}}{\partial \xi_{a_i}} \\ \mathbf{0} & \psi\mathbf{B}_{uint}\frac{\partial \mathbf{D}_{up}}{\partial \xi_{a_i}} \end{matrix} \\ \begin{matrix} \mathbf{B}_{uint}\frac{\partial \mathbf{C}_{yp}}{\partial \xi_{a_i}} \\ \begin{bmatrix} \mathbf{0} & \mathbf{0} & \frac{\psi}{L}\frac{\partial \mathbf{L}_{c_a}}{\partial \xi_{a_i}}^T\mathbf{U}_L & \mathbf{0} \end{bmatrix} \end{matrix} & \begin{matrix} \mathbf{0} & \mathbf{0} \\ \mathbf{0} & \mathbf{0} \end{matrix} \end{bmatrix} \tag{4.50}$$

$$\frac{\partial \mathbf{A}_t}{\partial \xi_{s_i}} = \begin{bmatrix} \begin{bmatrix} \mathbf{0} & \mathbf{0} \\ -\frac{\partial \mathbf{M}^{-1}}{\partial \xi_{s_i}}\mathbf{K} & -\frac{\partial \mathbf{M}^{-1}}{\partial \xi_i}\mathbf{C} \end{bmatrix} & \begin{matrix} \mathbf{0} & \psi\frac{\partial \mathbf{B}_{up}}{\partial \xi_{s_i}} \\ \mathbf{0} & \psi\mathbf{B}_{uint}\frac{\partial \mathbf{D}_{up}}{\partial \xi_{s_i}} \end{matrix} \\ \begin{matrix} \mathbf{B}_{uint}\frac{\partial \mathbf{C}_{yp}}{\partial \xi_{s_i}} \\ \mathbf{0} \end{matrix} & \begin{matrix} \mathbf{0} & \mathbf{0} \\ \mathbf{0} & \mathbf{0} \end{matrix} \end{bmatrix} \tag{4.51}$$

$$\frac{\partial \mathbf{B}_{dt}}{\partial \xi_{a_i}} = \begin{bmatrix} \mathbf{0} \\ \frac{\partial \mathbf{M}^{-1}}{\partial \xi_{a_i}}\mathbf{B}_d \\ \mathbf{B}_{uint}\frac{\partial \mathbf{D}_{dp}}{\partial \xi_{a_i}} \\ \mathbf{0} \end{bmatrix} \tag{4.52}$$

$$\frac{\partial \mathbf{B}_{dt}}{\partial \xi_{s_i}} = \begin{bmatrix} \mathbf{0} \\ \frac{\partial \mathbf{M}^{-1}}{\partial \xi_{s_i}}\mathbf{B}_d \\ \mathbf{B}_{uint}\frac{\partial \mathbf{D}_{dp}}{\partial \xi_{s_i}} \\ \mathbf{0} \end{bmatrix} \tag{4.53}$$

where

$$\frac{\partial \mathbf{M}^{-1}}{\partial \xi_{a_i}} = -\mathbf{M}^{-1}\frac{\partial \mathbf{M}}{\partial \xi_{a_i}}\mathbf{M}^{-1} = \\ = -\mathbf{M}^{-1}\begin{bmatrix} \mathbf{U}_L^T\frac{\partial \mathbf{L}_{c_a}}{\partial \xi_{a_i}}\mathbf{Diag}\{M_{a_i}\}\mathbf{L}_{c_a}^T\mathbf{U}_L + \\ \mathbf{U}_L^T\mathbf{L}_{c_a}\mathbf{Diag}\{M_{a_i}\}\frac{\partial \mathbf{L}_{c_a}}{\partial \xi_{a_i}}\mathbf{U}_L & \mathbf{0} \\ \mathbf{0} & \mathbf{0} \end{bmatrix}\mathbf{M}^{-1} \tag{4.54}$$

$$\frac{\partial \mathbf{M}^{-1}}{\partial \xi_{s_i}} = -\mathbf{M}^{-1}\frac{\partial \mathbf{M}}{\partial \xi_{s_i}}\mathbf{M}^{-1} = \\ = -\mathbf{M}^{-1}\begin{bmatrix} \mathbf{U}_L^T\frac{\partial \mathbf{L}_{c_s}}{\partial \xi_{s_i}}\mathbf{Diag}\{M_{s_i}\}\mathbf{L}_{c_s}^T\mathbf{U}_L + \\ \mathbf{U}_L^T\mathbf{L}_{c_s}\mathbf{Diag}\{M_{s_i}\}\frac{\partial \mathbf{L}_{c_s}}{\partial \xi_{s_i}}\mathbf{U}_L & \mathbf{0} \\ \mathbf{0} & \mathbf{0} \end{bmatrix}\mathbf{M}^{-1} \tag{4.55}$$

$$\frac{\partial \mathbf{C}}{\partial \xi_{a_i}} = \begin{bmatrix} \mathbf{U}_L^T\frac{\partial \mathbf{L}_{c_a}}{\partial \xi_{a_i}}\mathbf{Diag}\{C_{a_i}\}\mathbf{L}_{c_a}^T\mathbf{U}_L + \\ \mathbf{U}_L^T\mathbf{L}_{c_a}\mathbf{Diag}\{C_{a_i}\}\frac{\partial \mathbf{L}_{c_a}}{\partial \xi_{a_i}}\mathbf{U}_L & -\mathbf{U}_L^T\frac{\partial \mathbf{L}_{c_a}}{\partial \xi_{a_i}}\mathbf{Diag}\{C_{a_i}\} \\ -\mathbf{Diag}\{C_{a_i}\}\mathbf{L}_{c_a}^T\mathbf{U}_L & \mathbf{0} \end{bmatrix} \tag{4.56}$$

$$\frac{\partial \mathbf{K}}{\partial \xi_{a_i}} = \begin{bmatrix} \mathbf{U}_L^T\frac{\partial \mathbf{L}_{c_a}}{\partial \xi_{a_i}}\mathbf{Diag}\{K_{a_i}\}\mathbf{L}_{c}^T\mathbf{U}_L + \\ \mathbf{U}_L^T\mathbf{L}_{c_a}\mathbf{Diag}\{K_{a_i}\}\frac{\partial \mathbf{L}_{c_a}}{\partial \xi_{a_i}}\mathbf{U}_L & -\mathbf{U}_L^T\frac{\partial \mathbf{L}_{c_a}}{\partial \xi_{a_i}}\mathbf{Diag}\{K_{a_i}\} \\ -\mathbf{Diag}\{K_{a_i}\}\mathbf{L}_{c_a}^T\mathbf{U}_L & \mathbf{0} \end{bmatrix} \tag{4.57}$$

$$\frac{\partial \mathbf{B}_{up}}{\partial \xi_{a_i}} = \begin{bmatrix} \mathbf{0} \\ \frac{\partial \mathbf{M}^{-1}}{\partial \xi_{a_i}}\begin{bmatrix} -\mathbf{U}_L^T\mathbf{L}_{c_a} \\ \mathbf{I} \end{bmatrix} + \mathbf{M}^{-1}\begin{bmatrix} -\mathbf{U}_L^T\frac{\partial \mathbf{L}_{c}}{\partial \xi_{a_i}} \\ \mathbf{0} \end{bmatrix} \end{bmatrix} \tag{4.58}$$

$$\frac{\partial \mathbf{B}_{up}}{\partial \xi_{s_i}} = \begin{bmatrix} \mathbf{0} \\ \frac{\partial \mathbf{M}^{-1}}{\partial \xi_{s_i}}\begin{bmatrix} -\mathbf{U}_L^T\mathbf{L}_{c_s} \\ \mathbf{I} \end{bmatrix} \end{bmatrix} \tag{4.59}$$

$$\frac{\partial \mathbf{C}_{yp}}{\partial \xi_{a_i}} = \begin{bmatrix} \mathbf{0} & \mathbf{0} & \mathbf{L}_{c_s}\mathbf{U}_L & \mathbf{0} \end{bmatrix} \begin{bmatrix} \mathbf{0} & \mathbf{0} \\ -\frac{\partial \mathbf{M}^{-1}}{\partial \xi_{a_i}}\mathbf{K} - \mathbf{M}^{-1}\frac{\partial \mathbf{K}}{\partial \xi_{a_i}} & -\frac{\partial \mathbf{M}^{-1}}{\partial \xi_{a_i}}\mathbf{C} - \mathbf{M}^{-1}\frac{\partial \mathbf{C}}{\partial \xi_{a_i}} \end{bmatrix} \tag{4.60}$$

$$\begin{aligned} \frac{\partial \mathbf{C}_{yp}}{\partial \xi_{s_i}} = & \begin{bmatrix} \mathbf{0} & \mathbf{0} & \frac{\partial \mathbf{L}_{c_s}}{\partial \xi_{s_i}}\mathbf{U}_L & \mathbf{0} \end{bmatrix} \begin{bmatrix} \mathbf{0} & \mathbf{I} \\ -\mathbf{M}^{-1}\mathbf{K} & -\mathbf{M}^{-1}\mathbf{C} \end{bmatrix} \\ & + \begin{bmatrix} \mathbf{0} & \mathbf{0} & \mathbf{L}_{c_s}\mathbf{U}_L & \mathbf{0} \end{bmatrix} \begin{bmatrix} \mathbf{0} & \mathbf{0} \\ -\frac{\partial \mathbf{M}^{-1}}{\partial \xi_{s_i}}\mathbf{K} & -\frac{\partial \mathbf{M}^{-1}}{\partial \xi_{s_i}}\mathbf{C} \end{bmatrix} \end{aligned} \tag{4.61}$$

$$\frac{\partial \mathbf{D}_{up}}{\partial \xi_{a_i}} = \begin{bmatrix} \mathbf{0} & \mathbf{0} & \mathbf{L}_{c_s}\mathbf{U}_L & \mathbf{0} \end{bmatrix} \frac{\partial \mathbf{B}_{up}}{\partial \xi_{a_i}} \tag{4.62}$$

$$\begin{aligned} \frac{\partial \mathbf{D}_{up}}{\partial \xi_{s_i}} = & \begin{bmatrix} \mathbf{0} & \mathbf{0} & \frac{\partial \mathbf{L}_{s_a}}{\partial \xi_{s_i}}\mathbf{U}_L & \mathbf{0} \end{bmatrix} \mathbf{B}_{up} \\ & + \begin{bmatrix} \mathbf{0} & \mathbf{0} & \mathbf{L}_{c_s}\mathbf{U}_L & \mathbf{0} \end{bmatrix} \frac{\partial \mathbf{B}_{up}}{\partial \xi_{s_i}} \end{aligned} \tag{4.63}$$

$$\frac{\partial \mathbf{D}_{dp}}{\partial \xi_{a_i}} = \begin{bmatrix} \mathbf{0} & \mathbf{0} & \mathbf{L}_{c_s}\mathbf{U}_L & \mathbf{0} \end{bmatrix} \frac{\partial \mathbf{M}^{-1}}{\partial \xi_{a_i}}\mathbf{B}_d \tag{4.64}$$

$$\begin{aligned} \frac{\partial \mathbf{D}_{dp}}{\partial \xi_{s_i}} = & \begin{bmatrix} \mathbf{0} & \mathbf{0} & \frac{\partial \mathbf{L}_{s_a}}{\partial \xi_{s_i}}\mathbf{U}_L & \mathbf{0} \end{bmatrix} \mathbf{M}^{-1}\mathbf{B}_d \\ & + \begin{bmatrix} \mathbf{0} & \mathbf{0} & \mathbf{L}_{c_s}\mathbf{U}_L & \mathbf{0} \end{bmatrix} \frac{\partial \mathbf{M}^{-1}}{\partial \xi_{s_i}}\mathbf{B}_d \end{aligned} \tag{4.65}$$

The derivatives $\frac{\partial \mathbf{L}_{c_a}}{\partial \eta_{a_i}}$ and $\frac{\partial \mathbf{L}_{c_s}}{\partial \eta_{s_i}}$ can be computed as in Equations 4.3.2 and 4.42.
Exploting previous equations and Equation 4.33 the following derivatives can be computed:

$$\frac{\partial J}{\partial \xi_{a_i}} = Tr[(\frac{\partial J}{\partial \mathbf{A}_t})^T \frac{\partial \mathbf{A}_t}{\partial \xi_{a_i}}] + Tr[(\frac{\partial J}{\partial \mathbf{B}_{dt}})^T \frac{\partial \mathbf{B}_{dt}}{\partial \xi_{a_i}}] \tag{4.66}$$

$$\frac{\partial J}{\partial \xi_{s_i}} = Tr[(\frac{\partial J}{\partial \mathbf{A}_t})^T \frac{\partial \mathbf{A}_t}{\partial \xi_{s_i}}] + Tr[(\frac{\partial J}{\partial \mathbf{B}_{dt}})^T \frac{\partial \mathbf{B}_{dt}}{\partial \xi_{s_i}}] \tag{4.67}$$

If the plate is provided with collocated sensor/actuator pairs, then the previous equations remain valid imposing

$$\mathbf{L}_{c_s} = \mathbf{L}_{c_a}^T \tag{4.68}$$

$$\frac{\partial \mathbf{L}_{c_s}}{\partial \xi_i} = \frac{\partial \mathbf{L}_{c_a}}{\partial \xi_i}^T \tag{4.69}$$

$$\frac{\partial \mathbf{L}_{c_s}}{\partial \eta_i} = \frac{\partial \mathbf{L}_{c_a}}{\partial \eta_i}^T \tag{4.70}$$

and the gradient can be computed by summing up Equations 4.66 and 4.67.

The same considerations and equations hold for η_i coordinates.

Finally the same equations hold also if the radiation model is added to the structural one. In this case the state matrices derived in Chapter 3 will be used but this will not have any effect on the derivatives previously formulated as the acoustic model doesn't depend on actuator/sensor positions.

Chapter 5

Results of vibration control with sensors and actuators in assigned positions

Referring to the structural model and the control strategy presented in Chapter 2 and Chapter 4, let's study the active vibration control (AVC) of plates in different configurations, with assigned sensor/actuator grids and using the Stochastic Suboptimal Control.
The three different types of suboptimal controllers presented in Chapter 1 (decentralized, centralized and equal gains controllers) are here considered.

Some exampes of AVC performed using assigned grids of sensor/actuator collocated pairs will be presented in the following sections. Differences among the three control strategies mentioned above will be discussed, by varying the number of actuators and sensors. An analysis of the control problem by varying the number of modes considered in the design reduced order model will be also provided.
Finally, some remarks on the effects due to the dynamics of sensors and actuators and to the control weights will be presented.

All data of the electromechanical model of the actuators are taken from the datasheets of Micromega Dynamics [1]. In particular, inertial actuators of the type ADD-1N are used (Figure 5.1).
Sensors are located in the same positions of the actuators (collocated sensor/actuator pairs) and their properties are taken from PCB Piezotronics [2]. In particular, miniature single axis piezoelectric accelerometers of the model 352C23 are used (Figure 5.2). Collocated sensor/actuator pairs are here con-

sidered. The integrator devices are modeled as second order dynamic systems with a damping factor of 0.7 and a natural frequency a decade smaller than the lowest frequency of the plate.
Uniform distributed or randomly distributed white noise disturbances are used to excite the plate.
The weighting matrix $\mathbf{W}_{uu}$ is chosen diagonal, with all equal elements W_{uu}, and selected in order to comply with the maximum peak current limitation of the actuator considered. As relative values between the weighting matrices count, the performance weighting matrix $\mathbf{W}_{zz}$ is selected as the identity matrix.
A reduced order model with modes up to the frequency $f_{design}^{max} = 1000$ Hz is considered for the control design model, while the test model contains modes up to the frequency $f_{test}^{max} = 10000$ Hz.
The models of the plates are built by using a number of Ritz functions that is chosen according to the convergence analyses presented in Chapter 8.
Two types of materiales, whose properties are listed in Table 5.1, are considered.

Actuator Parameters	Moving mass weight	32 gr	
	Suspension stiffness	180N/m	
	Suspension damping	$\zeta = 0.2$	
	Moving mass stroke	±1 mm	
	Resonant frequency	12Hz	
	Dimensions (∅ x H)	∅32 mm x 37 mm	
	Force constant	1.6 N/A	
	Total Weight	84 gr	
	Mechanical Interface	Flat surface	
Winding Constants	DC Resistance	3Ω	
	Inductance	70 ~ 100 µH	
	Max. temperature of coil	105°C (221°F)	
	Max. continuous current	1 A (at 20°C ambient temperature)	
	Max. peak current	2 A	
Environment		***Operating***	***Non-Operating***
	Temperature	0 ~ 40°C (32 ~ 104°F)	-20 ~ 75°C (-4 ~ 167°F)
	Humidity	5 ~ 85% @ 40°C (104°F)	5 ~ 95%
Electrical Interface	Twin 0.41 mm^2 cable		

Figure 5.1: ADD-1N inertial actuator specifications.

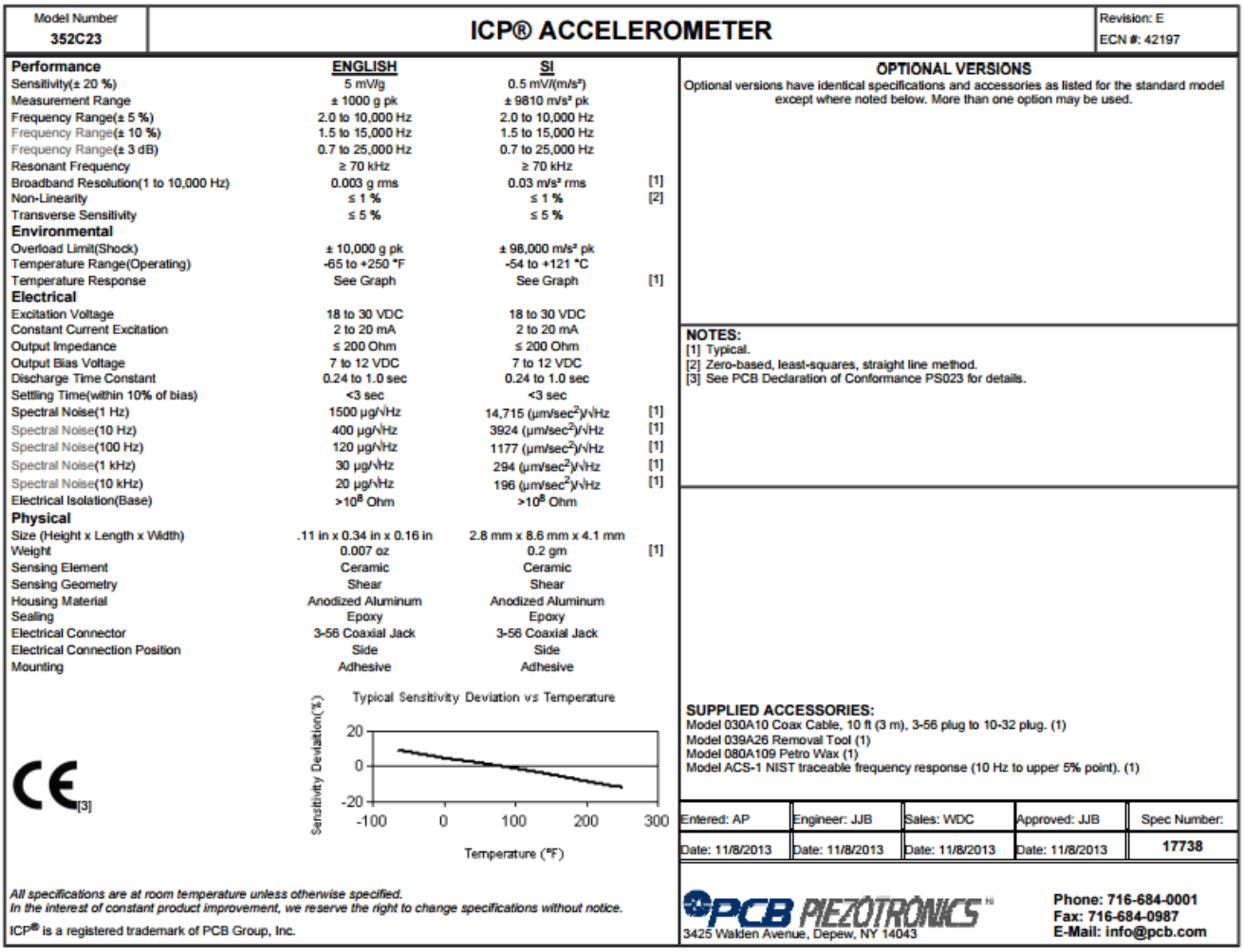

Model Number 352C23

ICP® ACCELEROMETER

Revision: E
ECN #: 42197

Performance	ENGLISH	SI	
Sensitivity(± 20 %)	5 mV/g	0.5 mV/(m/s²)	
Measurement Range	± 1000 g pk	± 9810 m/s² pk	
Frequency Range(± 5 %)	2.0 to 10,000 Hz	2.0 to 10,000 Hz	
Frequency Range(± 10 %)	1.5 to 15,000 Hz	1.5 to 15,000 Hz	
Frequency Range(± 3 dB)	0.7 to 25,000 Hz	0.7 to 25,000 Hz	
Resonant Frequency	≥ 70 kHz	≥ 70 kHz	
Broadband Resolution(1 to 10,000 Hz)	0.003 g rms	0.03 m/s² rms	[1]
Non-Linearity	≤ 1 %	≤ 1 %	[2]
Transverse Sensitivity	≤ 5 %	≤ 5 %	
Environmental			
Overload Limit(Shock)	± 10,000 g pk	± 98,000 m/s² pk	
Temperature Range(Operating)	-65 to +250 °F	-54 to +121 °C	
Temperature Response	See Graph	See Graph	[1]
Electrical			
Excitation Voltage	18 to 30 VDC	18 to 30 VDC	
Constant Current Excitation	2 to 20 mA	2 to 20 mA	
Output Impedance	≤ 200 Ohm	≤ 200 Ohm	
Output Bias Voltage	7 to 12 VDC	7 to 12 VDC	
Discharge Time Constant	0.24 to 1.0 sec	0.24 to 1.0 sec	
Settling Time(within 10% of bias)	<3 sec	<3 sec	
Spectral Noise(1 Hz)	1500 µg/√Hz	14,715 (µm/sec²)/√Hz	[1]
Spectral Noise(10 Hz)	400 µg/√Hz	3924 (µm/sec²)/√Hz	[1]
Spectral Noise(100 Hz)	120 µg/√Hz	1177 (µm/sec²)/√Hz	[1]
Spectral Noise(1 kHz)	30 µg/√Hz	294 (µm/sec²)/√Hz	[1]
Spectral Noise(10 kHz)	20 µg/√Hz	196 (µm/sec²)/√Hz	[1]
Electrical Isolation(Base)	>10⁸ Ohm	>10⁸ Ohm	
Physical			
Size (Height x Length x Width)	.11 in x 0.34 in x 0.16 in	2.8 mm x 8.6 mm x 4.1 mm	
Weight	0.007 oz	0.2 gm	[1]
Sensing Element	Ceramic	Ceramic	
Sensing Geometry	Shear	Shear	
Housing Material	Anodized Aluminum	Anodized Aluminum	
Sealing	Epoxy	Epoxy	
Electrical Connector	3-56 Coaxial Jack	3-56 Coaxial Jack	
Electrical Connection Position	Side	Side	
Mounting	Adhesive	Adhesive	

CE [3]

Typical Sensitivity Deviation vs Temperature

All specifications are at room temperature unless otherwise specified.
In the interest of constant product improvement, we reserve the right to change specifications without notice.

ICP® is a registered trademark of PCB Group, Inc.

OPTIONAL VERSIONS

Optional versions have identical specifications and accessories as listed for the standard model except where noted below. More than one option may be used.

NOTES:
[1] Typical.
[2] Zero-based, least-squares, straight line method.
[3] See PCB Declaration of Conformance PS023 for details.

SUPPLIED ACCESSORIES:
Model 030A10 Coax Cable, 10 ft (3 m), 3-56 plug to 10-32 plug. (1)
Model 039A26 Removal Tool (1)
Model 080A109 Petro Wax (1)
Model ACS-1 NIST traceable frequency response (10 Hz to upper 5% point). (1)

Entered: AP	Engineer: JJB	Sales: WDC	Approved: JJB	Spec Number:
Date: 11/8/2013	Date: 11/8/2013	Date: 11/8/2013	Date: 11/8/2013	17738

PCB PIEZOTRONICS
3425 Walden Avenue, Depew, NY 14043

Phone: 716-684-0001
Fax: 716-684-0987
E-Mail: info@pcb.com

Figure 5.2: Miniature single axis piezoelectric accelerometer specifications - model 352C23.

Code	Material	D_{22}	D_{12}	D_{66}	ν	E	ρ
M0	Isotropic	D	νD	$(1-\nu)D/2$	0.3	$7\text{x}10^{10}$ Pa	2720 Kg/m^3
M1	Orthotropic	$D/2$	νD	$D/2$	0.3	$7\text{x}10^{10}$ Pa	2700 Kg/m^3

Table 5.1: Material properties used in the numerical results - D_{ij} are the bending/twisting rigidities of the plate, ρ is the mass per unit volume, h is the plate thickness, ν is Poisson's coefficient, E is the Young's Modulus and $D = Eh^3/12(1-\nu^2)$ is the flexural rigidity of the plate.

5.1 Fully clamped isotropic plate with sensor/actuator pairs in assigned positions

A fully clamped isotropic (material M0) plate is here considered, with properties reported in Table 5.2.
The dynamics of actuators and sensors are taken into account for all the results in the present section.
A uniform distributed white noise excitation of intensity $W_{dd} = 100$ is used as a disturbance.

Property	Description	Value
a	x dimension	0.8 m
b	y dimension	0.5 m
ζ	Modal damping factor	0.001
h	Thickness	0.002 m

Table 5.2: Properties of the CCCC M0 plate.

5.1.1 Fully clamped isotropic plate with one actuator/sensor pair

Consider the case of a plate with one actuator/sensor pair located in the central position, as shown in Figure 5.3.

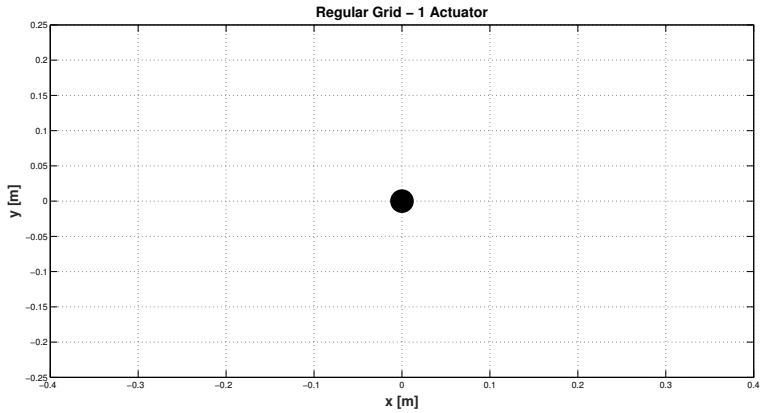

Figure 5.3: Assigned actuator position on the CCCC M0 plate - 1 Actuator.

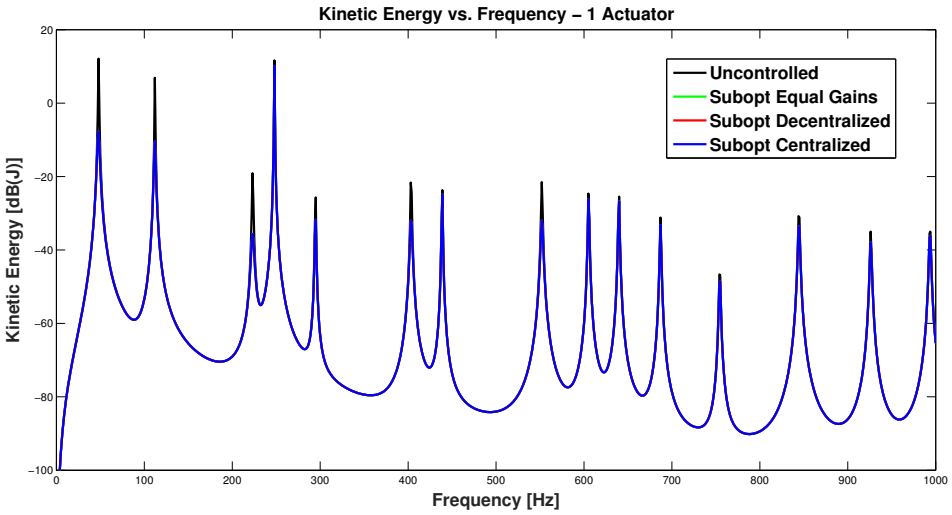

Figure 5.4: Uncontrolled and controlled kinetic energy versus frequency for different types of control strategy - CCCC M0 plate - 1 Actuator - $W_{uu} = 1/700$.

In Figure 5.4 the results in terms of kinetic energy versus frequency are presented, for a control weight $W_{uu} = 1/700$. Obviously, for the case of control performed with a single actuator/sensor pair, there will be no difference among the three types of suboptimal control in terms of the minimum found for the cost function:

$$J_{dec} = J_{cen} = J_{eq} = 0.1691$$

A time simulation with a time window of 1 second is performed in order to see the time evolution of some significant parameters as control currents (Figure 5.5).
It is possible to notice that, for the chosen value of the control weight, the values assumed by the control currents remain in the boundaries of $\pm 2A$ indicated in the actuator specifications.

In order to quantify the control energy, RMS values of forces, currents and voltages are reported:

$$\begin{aligned} RMS_{dec}^{force} = RMS_{cen}^{force} = RMS_{eq}^{force} = 0.8350 \text{ N} \\ RMS_{dec}^{curr} = RMS_{cen}^{curr} = RMS_{eq}^{curr} = 0.5219 \text{ A} \\ RMS_{dec}^{volt} = RMS_{cen}^{volt} = RMS_{eq}^{volt} = 1.5657 \text{ V} \end{aligned}$$

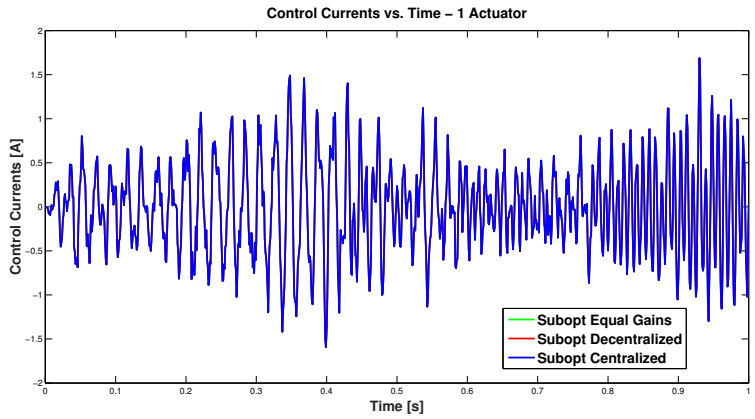

Figure 5.5: Control currents for the three control strategies - CCCC M0 plate - 1 Actuator.

5.1.2 Fully clamped isotropic plate with 5 actuator/sensor pairs

Let's consider now the same plate controlled by 5 sensor/actuator pairs located as in Figure 5.6.

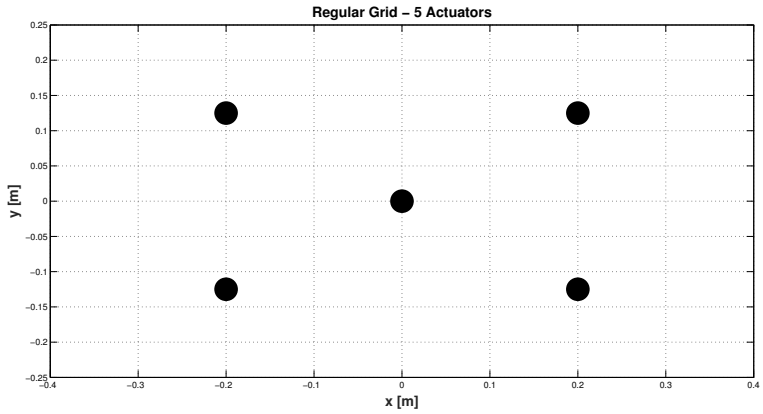

Figure 5.6: Assigned actuators positions on the CCCC M0 plate - 5 Actuators.

In Figure 5.7 the results in terms of kinetic energy versus frequency are presented. As expected, it is possible to notice that the centralized controller performs the best, while the decentralized and equal gains controllers give substantially the same results. This is clearly seen from the cost function values reported in Table 5.3. The chosen value for the control weight is $W_{uu} = 1/1500$.

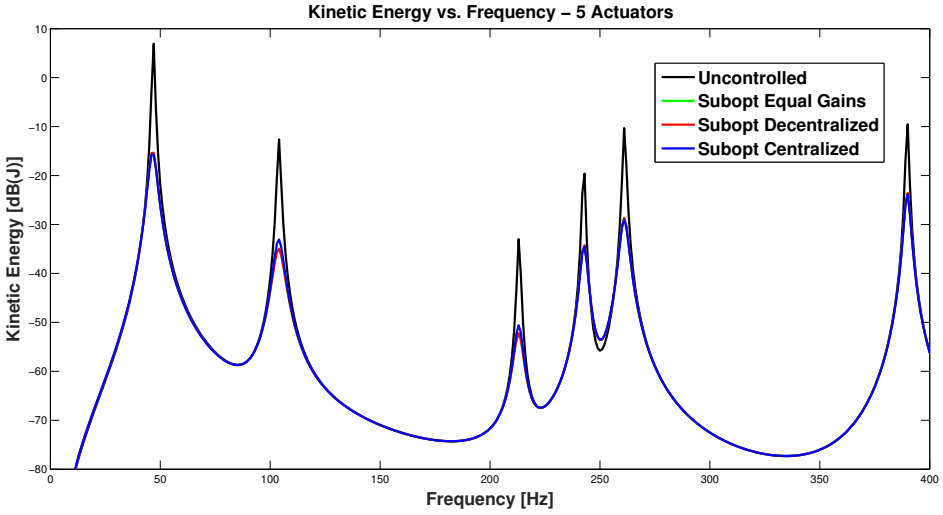

Figure 5.7: Uncontrolled and controlled kinetic energy versus frequency for different types of control strategy - CCCC M0 plate - 5 Actuators - $W_{uu} = 1/1500$.

Subopt Dec	Subopt Cen	Eq Gains
0.0767	0.0766	0.0767

Table 5.3: Cost function values - CCCC M0 plate - 5 Actuators.

Relative errors between cost functions obtained with the three types of controller are:

$$err_{dec-cen} = 0.1454\% \qquad err_{eq-dec} = 0.0055\%$$

As done before, time simulations with a time window of 1 second are performed in order to see the evolution of control currents for the three control strategies (Figure 5.8).

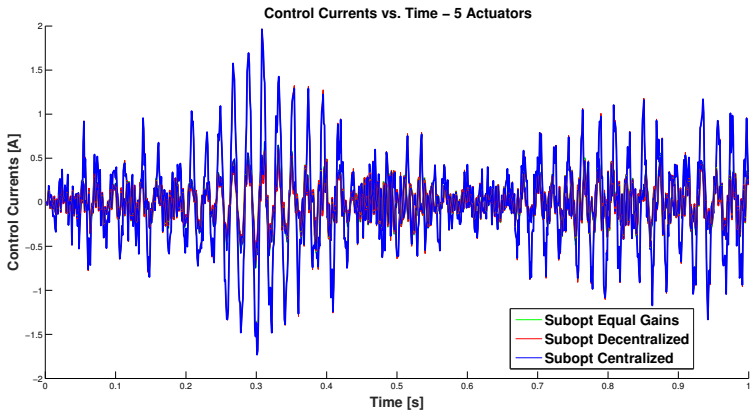

Figure 5.8: Control currents for the three control strategies - CCCC M0 plate - 5 Actuators.

In order to quantify the control energy, RMS values of forces, currents and voltages are reported:

$$RMS_{dec}^{force} = 0.4749 \text{ N} \qquad RMS_{cen}^{force} = 0.4759 \text{ N} \qquad RMS_{eq}^{force} = 0.4746 \text{ N}$$
$$RMS_{dec}^{curr} = 0.2968 \text{ A} \qquad RMS_{cen}^{curr} = 0.2974 \text{ A} \qquad RMS_{eq}^{curr} = 0.2967 \text{ A}$$
$$RMS_{dec}^{volt} = 0.8762 \text{ V} \qquad RMS_{cen}^{volt} = 0.8787 \text{ V} \qquad RMS_{eq}^{volt} = 0.8757 \text{ V}$$

5.1.3 Fully clamped isotropic plate with 9 actuator/sensor pairs

The same plate configuration is now studied with a regular grid of 9 actuator/sensor pairs (Figure 5.9)

In Figure 5.10 the results in terms of kinetic energy versus frequency are presented for a control weight $W_{uu} = 1/8000$. For this case it is possible to notice a more pronounced difference in terms of performance of the three different types of suboptimal controller. As expected, the best performance is achieved by the centralized controller, followed by the decentralized one.

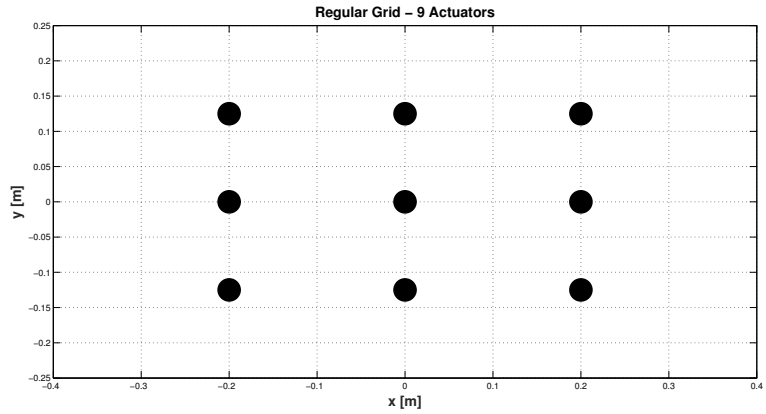

Figure 5.9: Assigned actuators positions on CCCC M0 plate - 9 Actuators.

The controller with equal gains is the simpler one, so it performs slightly worse than the decentralized controller.
These remarks are clearly proved by the cost function values reported in Table 5.4.

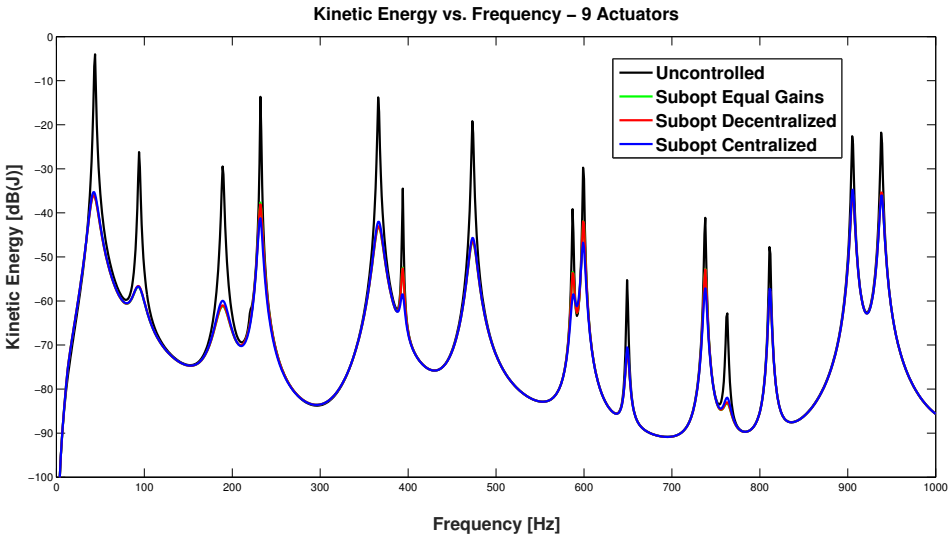

Figure 5.10: Uncontrolled and controlled kinetic energy versus frequency for different types of control strategy - CCCC M0 plate - 9 Actuators - $W_{uu} = 1/8000$.

Relative errors between cost functions obtained with the three types of controllers are:

$$err_{dec-cen} = 1.6095 \qquad err_{eq-dec} = 0.0804$$

Subopt Dec	Subopt Cen	Eq Gains
0.0275	0.0271	0.0277

Table 5.4: Cost function values - CCCC M0 plate - 9 Actuators.

The time simulation of control currents is presented in Figure 5.5.

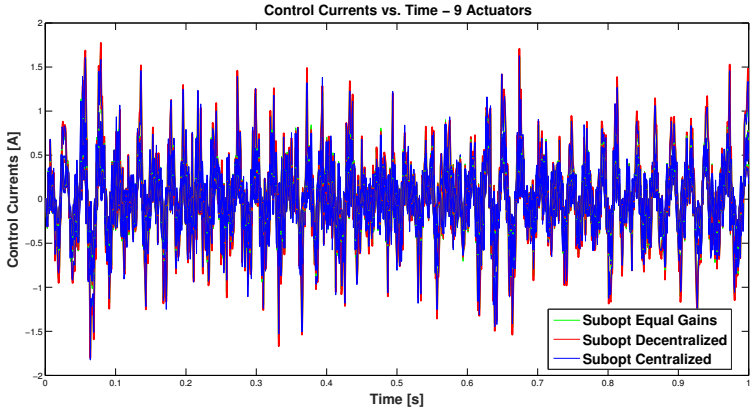

Figure 5.11: Control currents for the three control strategies - CCCC M0 plate - 9 Actuators.

In order to quantify the control energy, RMS values of forces, currents and voltages are reported:

$$RMS_{dec}^{force} = 0.5174 \text{ N} \quad RMS_{cen}^{force} = 0.5097 \text{ N} \quad RMS_{eq}^{force} = 0.5168 \text{ N}$$
$$RMS_{dec}^{curr} = 0.3234 \text{ A} \quad RMS_{cen}^{curr} = 0.3185 \text{ A} \quad RMS_{eq}^{curr} = 0.3230 \text{ A}$$
$$RMS_{dec}^{volt} = 0.9642 \text{ V} \quad RMS_{cen}^{volt} = 0.9504 \text{ V} \quad RMS_{eq}^{volt} = 0.9641 \text{ V}$$

5.1.4 Fully clamped isotropic plate with 16 actuator/sensor pairs

Let's now consider the same plate controlled by 16 actuators in a regular grid as in Figure 5.12.

In Figure 5.13 the results in terms of kinetic energy versus frequency are presented. For this problem a very low control effort weight is used ($W_{uu} = 1/50000$). It is possible to observe how a peak at low frequency arises in the energy plot: this peak is due to the resonance of the actuators, a phenomenon that is observed when the control weight is strongly reduced and the separation between the resonance frequency of the actuators and

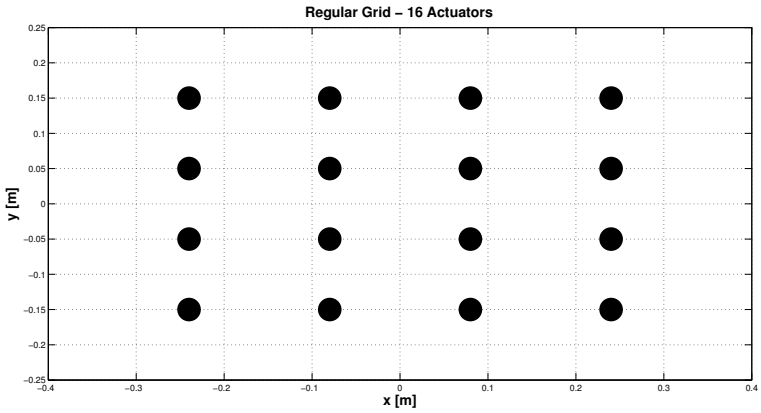

Figure 5.12: Assigned actuators positions on the CCCC M0 plate - 16 Actuators.

the first natural frequency of the plate is quite small. A brief study on this aspect is presented in the following section.

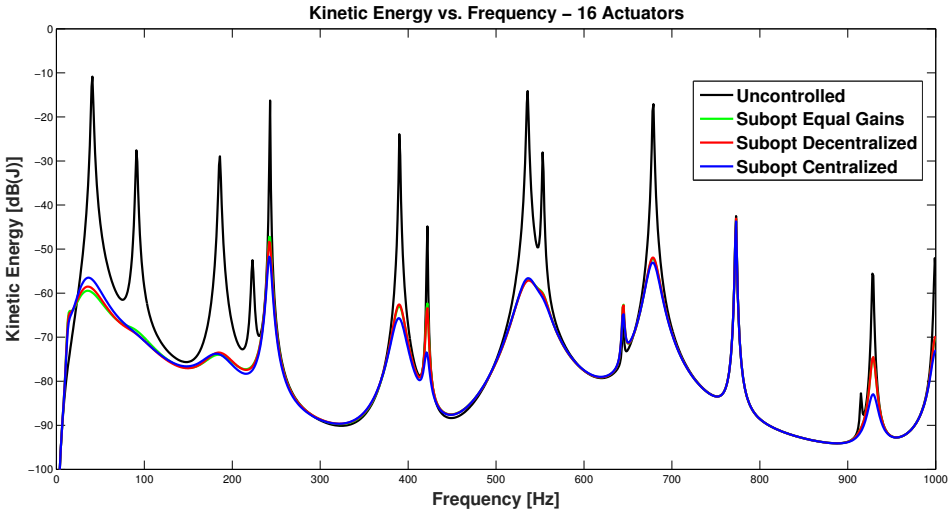

Figure 5.13: Uncontrolled and controlled kinetic energy versus frequency for different types of control strategy - CCCC M0 plate - 16 Actuators - $W_{uu} = 1/50000$.

5.2 Separation between resonance frequency of the actuators and first natural frequency of the plate

As shown in the previous example, a large resonance associated with the actuator dynamics may appear when a rather aggressive control action is introduced on the plate. The amplification of kinetic energy introduced by this phenomenon depends on the separation between the resonance frequency of the actuators and the first natural frequency of the plate. Let's consider the same fully clamped isotropic plate of the previous examples, but modeled with only one mode and controlled by one actuator/sensor pair placed in the center. In Figure 5.14 four plots of the spectrum of uncontrolled and controlled kinetic energies are presented for a control weight $W_{uu} = 1/10^6$ and different geometric dimensions of the plate(and so different values of natural frequencies): it is possible to notice how the resonance of the actuator is less and less important increasing the frequency gap between the dynamics of the actuator and the plate. For a frequency gap of 150 Hz the actuator resonance almost disappears.

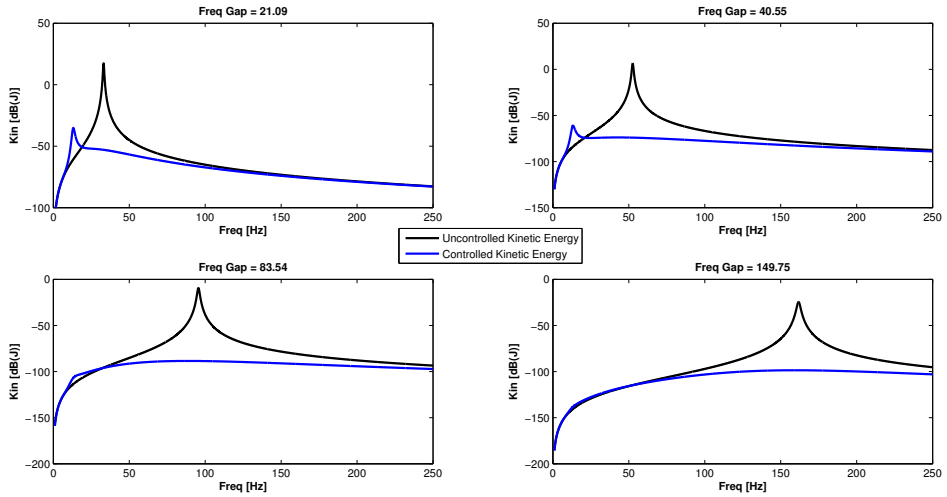

Figure 5.14: Uncontrolled and controlled kinetic energy versus frequency for $W_{uu} = 1/10^6$ and different values of the first natural frequency of the CCCC M0 plate - 1 Actuator

Some simulations have been performed in order to obtain an information on the minimum frequency gap required to obtain negligible amplifications in the controlled kinetic energy due to the effect described: in Table 5.5 some

suitable values of frequency gap between the dynamics of the actuators and the plate are presented for different control weights.

Weight	Frequency Gap
$1/10^5$	$80 - 90$ Hz
$1/10^4$	$30 - 40$ Hz
$1/10^3$	$20 - 30$ Hz

Table 5.5: Values of the frequency separation between the actuator resonance frequency and the fisrt natural frequency of the CCCC M0 plate, for different control weights, in order to avoid large actuator resonances.

5.3 Differences among centralized, decentralized and equal gains control startegies with different number of actuators

Several other simulations have been performed using the configuration considered in Section 5.1 and varying the number of actuator/sensor pairs in order to see the differences in the performances obtained with the three types of control strategy considered. The results in terms of percentage variation of the cost function between centralized and decentralized controllers and between decentralized and equal gains controllers versus the number of actuators used are reported in Figures 5.15 and 5.16, for a control weight $W_{uu} = 1/1000$.

The positions of actuator/sensor pairs have been chosen in order to keep the simmetry in the configuration. Nevertheless this arbitrariness in locating the transducers doesn't allow to observe a clear trend in the error evolution, which is mainly oscillatory. The most important remark is that, for any number of actuators considered, the error between decentralized and centralized controllers remains very low. This happens also for the error between decentralized and equal gains control strategies.
As the centralized controller presents a full gain matrix, the optimization procedure for this strategy is computationally demanding and, increasing the numeber of actuators, the time required for the convergence is greater and greater compared to the one of the decentralized controllers. This remark is clearly shown in Figure 5.17.

The same observations can be done performing the study on an orthotropic (material M1) cantilever plate, whose properties are shown in Table

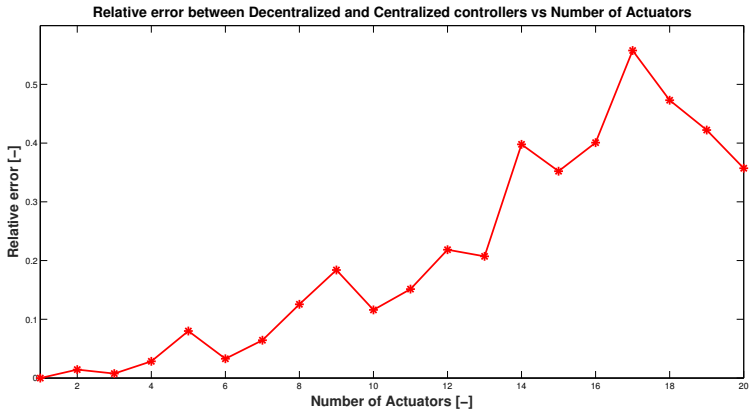

Figure 5.15: Percentage variation between Decentralized and Centralized controllers versus Number of Actuators - CCCC M0 plate

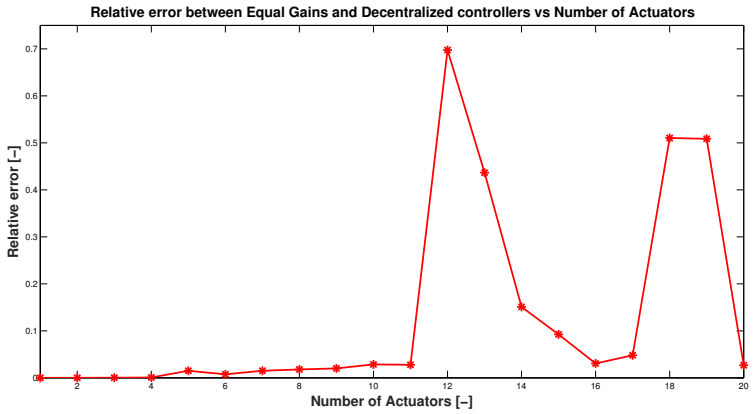

Figure 5.16: Percentage variation between Equal Gains and Decentralized controllers versus Number of Actuators - CCCC M0 plate

5.6.

Also in this case convergence times are shown in Figure 5.20.

It appears that using a simple equal gains decentralized control strategy provides closed-loop performances comparable to other more complicated stategies. Therefore, for the AVC of a simple structure like a plate, control strategies like equal gains and decentralized with independent gains are satisfactory compared to more complicated and computationally expensive centralized controllers.

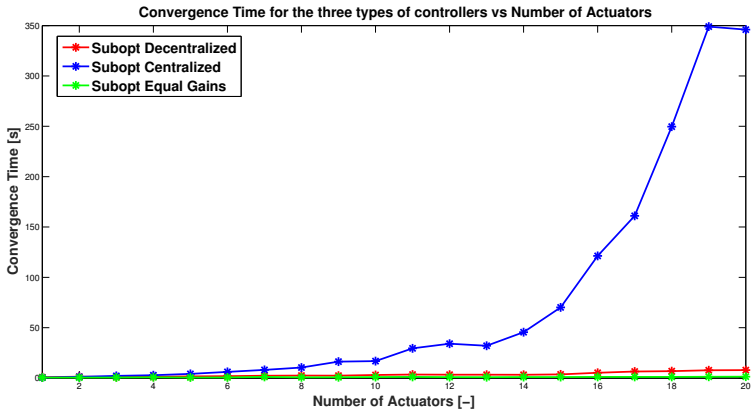

Figure 5.17: Convergence times for the three types of controller versus Number of Actuators - CCCC M0 plate

Property	Description	Value
a	x dimension	0.25 m
b	y dimension	0.25 m
ζ	Modal damping factor	0.001
h	Thickness	0.003 m

Table 5.6: Properties of the CFFF M1 plate

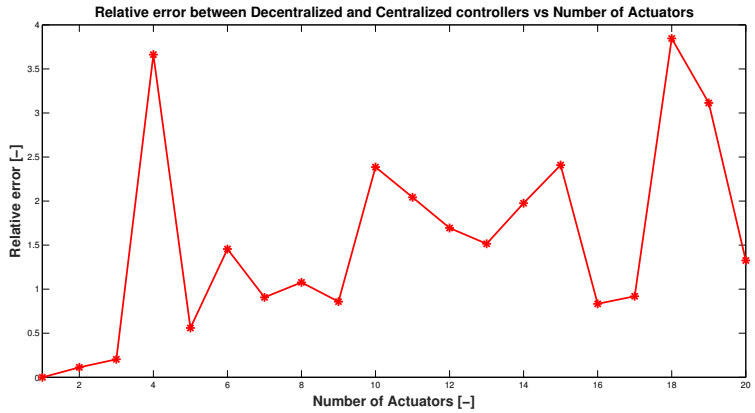

Figure 5.18: Percentage variation between Decentralized and Centralized controllers versus Number of Actuators - CFFF M1 plate

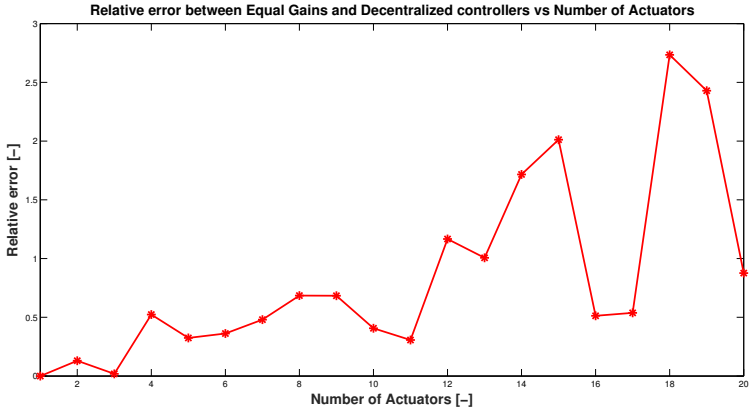

Figure 5.19: Percentage variation between Equal Gains and Decentralized controllers versus Number of Actuators - CFFF M1 plate

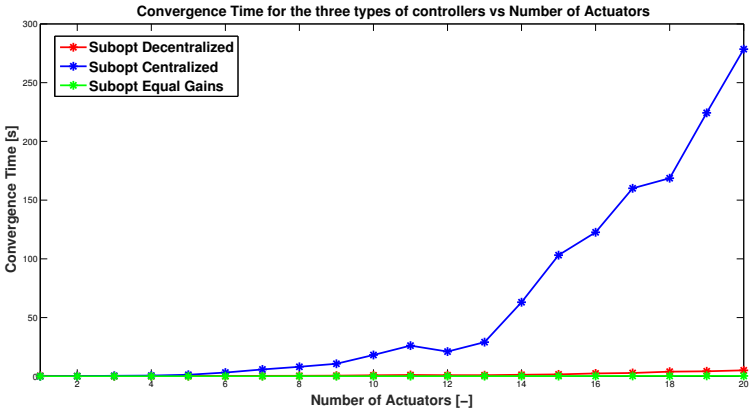

Figure 5.20: Convergence times for the three types of controllers vs Number of Actuators - CFFF M1 plate

5.4 Differences among centralized, decentralized and equal gains control strategies with different number of modes in the design reduced order model

Some simulations have been performed by varying the number of modes considered in the design reduced order model in order to study the sensitivity of the controllers to this parameter.
Let's consider the same fully clamped plate used in Section 5.1, controlled by 9 actuators placed as in Figure 5.9. The design reduced order model here

considered takes into account the dynamics of sensors and actuators and it is built considering only the first mode of the plate. The test model takes into account all modes up to the frequency $f_{test}^{max} = 10000$ Hz.

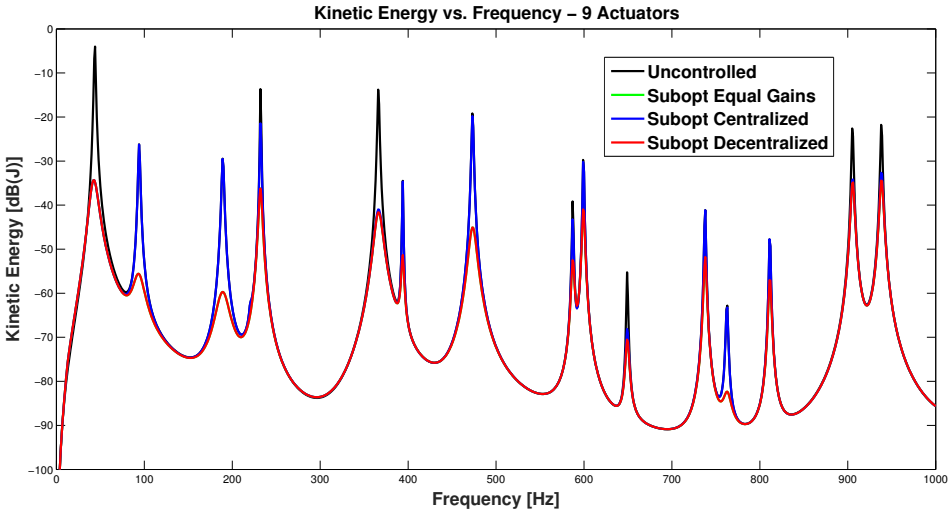

Figure 5.21: Uncontrolled and controlled kinetic energy versus frequency for different types of control strategy, considering only the first plate mode in the reduced order model - CCCC M0 plate - 9 Actuators - $W_{uu} = 1/8000$.

As we can see from Figure 5.21, the control system performs well, without introducing any destabilizing action. However, if few modes are considered in the reduced order model, the centralized control may perform worse than the other two control strategies in damping modes not included in the design model. Quite reasonably this result is due to the fact that the centralized control takes into account the behavior of the complete set of actuator/sensor pairs optimizing the control action for the modes it is considering. In a decentralized strategy, on the contrary, every actuator/sensor pair performs a control loop independent from the others and this may result in an advantage if models with few modes are provided.

Several simulations with very reduced order models have been performed but none of them has shown a destabilizing behavior of the control action. Even for very low damping values and taking into account only few modes the only effect observed is a degradation of the perfomance.
This remark can be shown in the following example, in which a fully simply supported, squared, orthotropic (material M1) plate is considered. Properties of the plate are reported in table 5.7.

The control is performed with 5 actuators positioned as in Figure 5.22 and

Property	Description	Value
a	x dimension	0.4 m
b	y dimension	0.4 m
ζ	Modal damping factor	10^{-4}
h	Thickness	0.003 m

Table 5.7: Properties of the SSSS M1 plate

the plate is excited with a randomly distributed white noise of unit intensity. Taking into account only the first 5 plate modes in the design reduced order model, the control action is quite ineffective but not destabilizing (Figure 5.23).

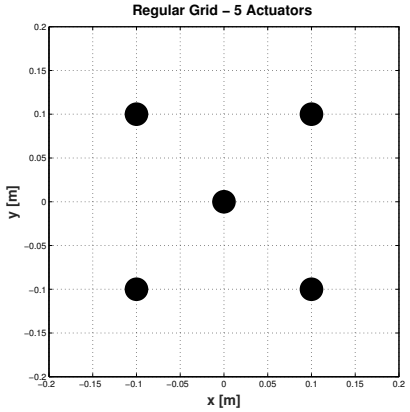

Figure 5.22: Assigned actuators positions on the SSSS M1 plate - 5 Actuators

Increasing the number of modes considered in the design model and keeping the control action quite constant in terms of control currents ($RMS^{curr}_{5modes} =$ 0.47 A, $RMS^{curr}_{30modes} = 0.45$ A) better results are obtained (Figure 5.24).

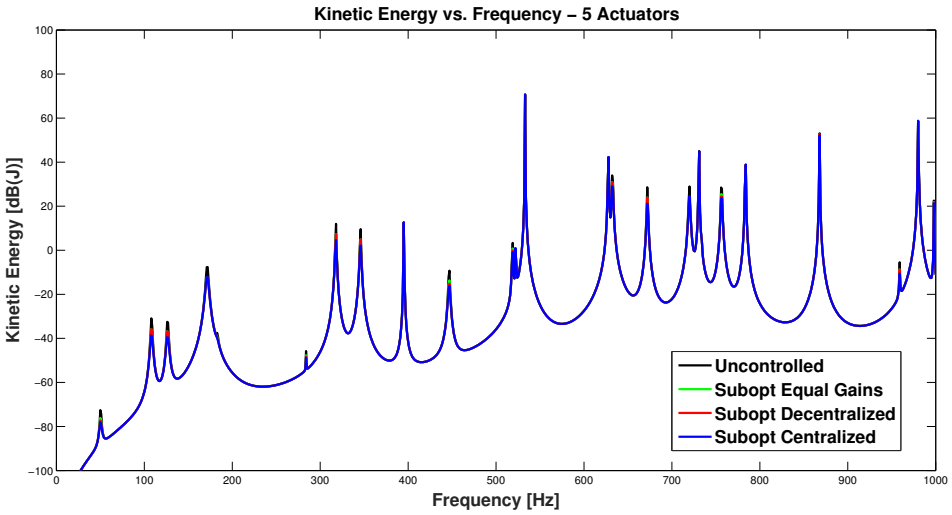

Figure 5.23: Uncontrolled and controlled kinetic energy versus frequency for different types of control strategy and considering only the first 5 plate modes in the reduced order model - SSSS M1 plate - 5 Actuators - $W_{uu} = 1/350$).

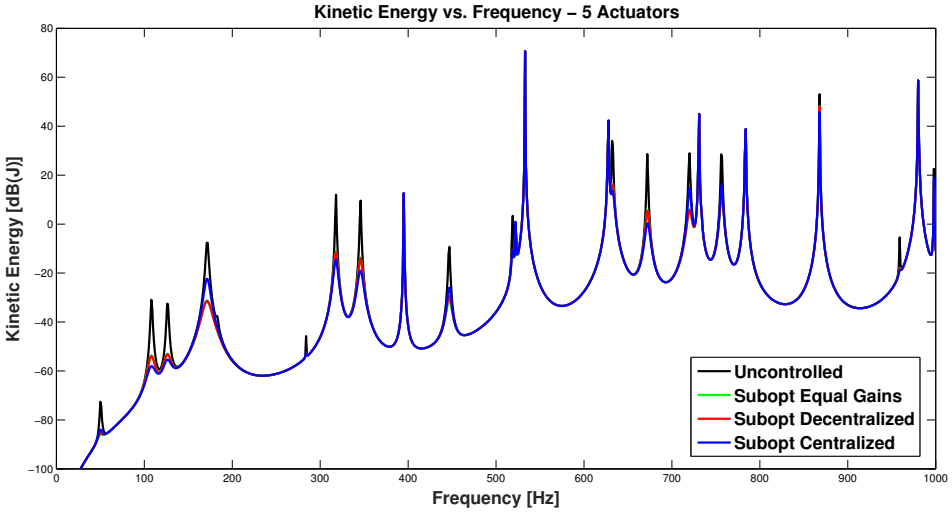

Figure 5.24: Uncontrolled and controlled kinetic energy versus frequency for different types of control strategy and considering only the first 30 plate modes in the reduced order model - SSSS M1 plate - 5 Actuators - $W_{uu} = 1/300$).

Chapter 6

Results of vibration control with sensors and actuators in optimal positions

In this chapter some AVC results are obtained using a minimization procedure which is capable of providing not only optimal gains but also optimal positions of sensors and actuators, according to what outlined in Chapter 4. In the following, some examples aimed at discussing AVC with optimal placement of collocated sensor/actuator pairs are presented.
In particular, a comparison between configurations with a fixed grid and an optimal grid of ideal sensor/actuator pairs are presented first. Then, an example of optimal grid AVC including actuators and sensors dynamics is presented in order to demonstrate that different optimal configurations do exist for the same problem, but they all correspond to similar values of the cost function.
Owing to the remarks on control strategies discussed in Chapter 5 and for the sake of brevity, only a decentralized control strategy will be considered in the present dissertation.

Properties of the sensors, the actuators and the materials considered are the same used in Chapter 5. Uniform distributed or randomly distributed white noise disturbances are used to excite the plate.
A reduced order model with modes up to the frequency $f_{design}^{max} = 1000$ Hz is considered for the control design model, while the test model contains modes up to the frequency $f_{test}^{max} = 10000$ Hz.
The models of the plates are built using a number of Ritz functions that is chosen according to the convergence analyses presented in Chapter 8

6.1 Comparison between fixed grid and optimal grid configurations

In this section some advantages of the optimization of positions of sensors and actuators are shown through two examples. In order to compare the optimal grid solutions with the fixed grid ones, ideal models are considered; indeed the kinetic energy response would deeply change varying the position of sensors and actuators if their dynamic effects were included.
In order to make a valid comparison, control weight matrices are selected so that almost the same RMS values of control forces are obtained for the compared configurations.
Collocated sensor/actuator pairs are considered.

6.1.1 Cantilever isotropic plate with one ideal actuator/sensor pair

Let's consider a cantilever isotropic (material M0) plate, equipped with a sensor/actuator pair located at $(0.17, 0)$ (Figure 6.1). The properties of the plate are reported in Table 6.1.

Property	Description	Value
a	x dimension	0.4 m
b	y dimension	0.3 m
ζ	Modal damping factor	0.001
h	Thickness	0.003 m

Table 6.1: Properties of the CFFF M0 plate

If the plate is excited with a randomly distributed white noise disturbance of unit intensity, the spectrum of the controlled kinetic energy in Figure 6.2 is obtained, using a control weight $W_{uu} = 1/150$. The configuration considered allows a good damping of flexural modes, as the first and the third, while it is mainly ineffective in damping the torsional modes because the actuator is located on a nodal line of these modes.

If a grid optimization is provided, the sensor/actuator pair is placed in a more suitable position in order to damp well all resonance peaks. The kinetic energy spectrum obtained, using a control weight $W_{uu} = 1/110$, is shown in Figure 6.3: even if some modes are less controlled compared to the fixed grid case, the optimal grid guarantees a more uniform damping action over the

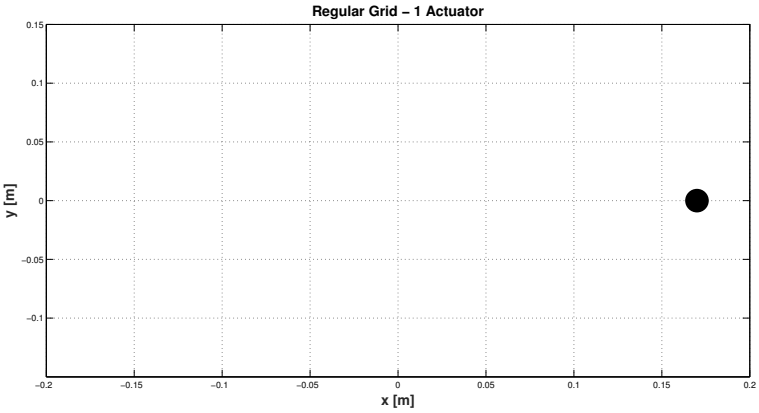

Figure 6.1: Assigned actuator position on the the CFFF M0 plate.

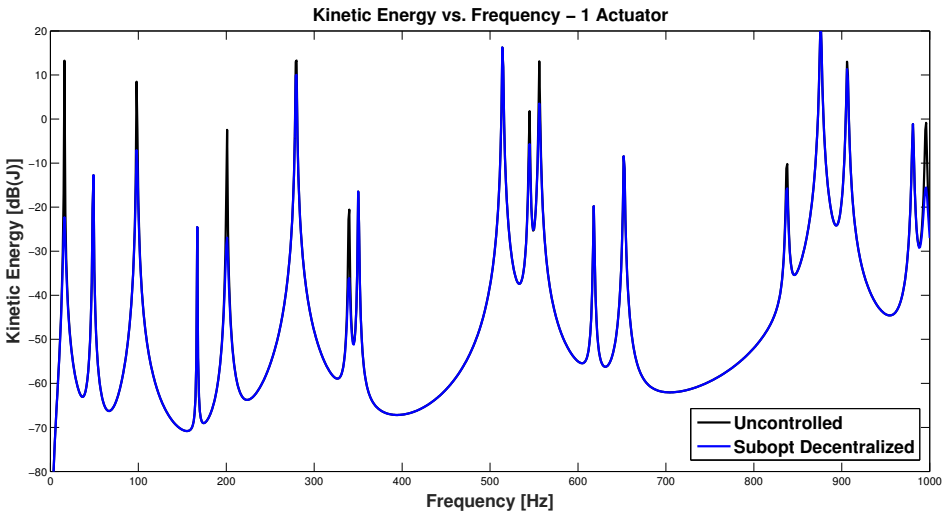

Figure 6.2: Uncontrolled and controlled kinetic energy versus frequency for a fixed grid configuration - CFFF M0 plate - 1 Actuator

bandwidth of interest (Figure 6.4). In particular, the better distribution of the control action over all modes reflects in a good damping of the torsional modes.

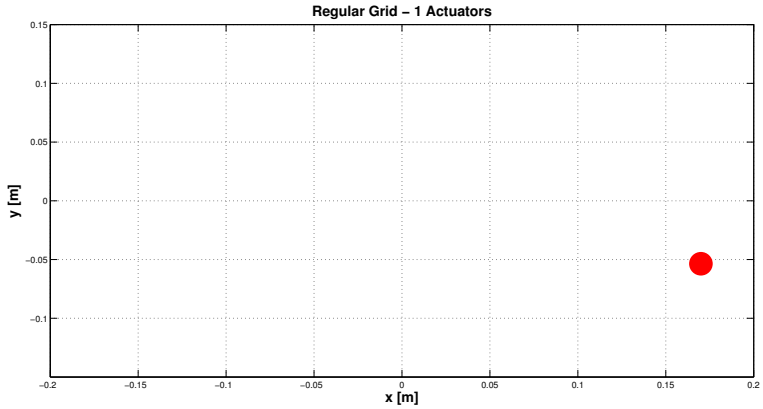

Figure 6.3: Optimal actuator position on the CFFF M0 plate.

The mode shape of a torsional mode (the second) is reported in Figure 6.5 : it is clear how the position of the actuator in the optimal grid case is suitable for damping this mode.

6.1.2 CFSF orthotropic plate with 5 ideal sensor/actuator pairs

Let's consider now a rectangular orthotropic (material M1) plate. The plate is clamped on an edge and simply supported on the opposed one, while the other two edges are free. Properties of the plate are reported in Table 6.2.

Property	Description	Value
a	x dimension	0.4 m
b	y dimension	0.3 m
ζ	Modal damping factor	0.001
h	Thickness	0.002 m

Table 6.2: Properties of the CFSF M1 plate

The control is performed with 5 actuators and the plate is excited with a randomly distributed white noise of unit intensity. In Figures 6.6 and 6.7 the

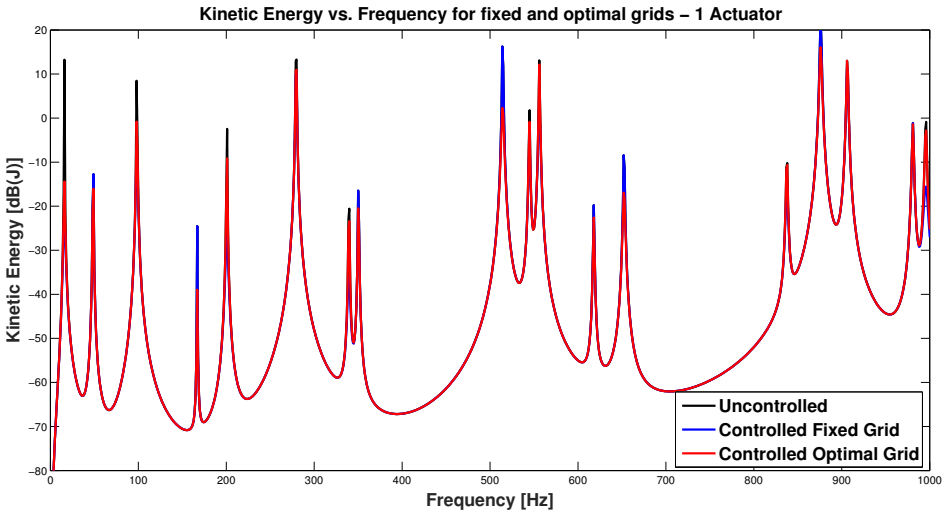

Figure 6.4: Kinetic energy versus frequency for fixed and optimal grid configurations - CFFF M0 plate - 1 Actuator.

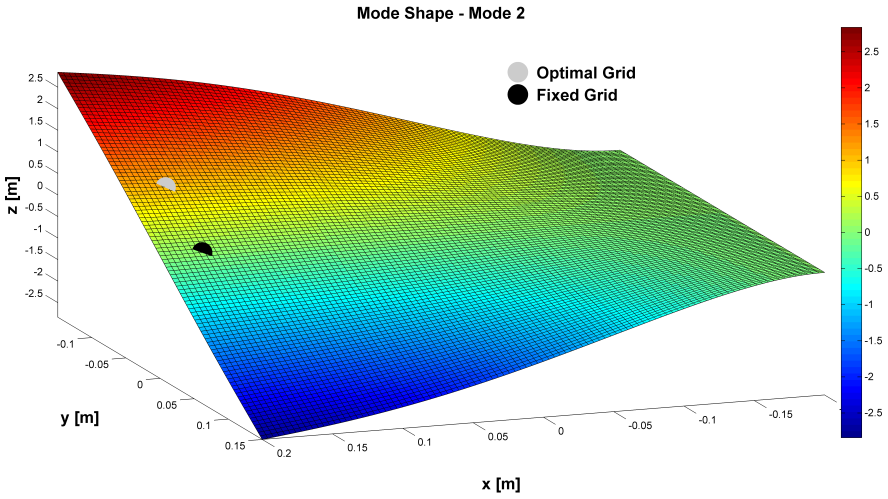

Figure 6.5: Mode shape - mode 2.

positions of the actuators in the fixed grid configuration and in the optimal positions obtained by the minimization process are presented, respectively.

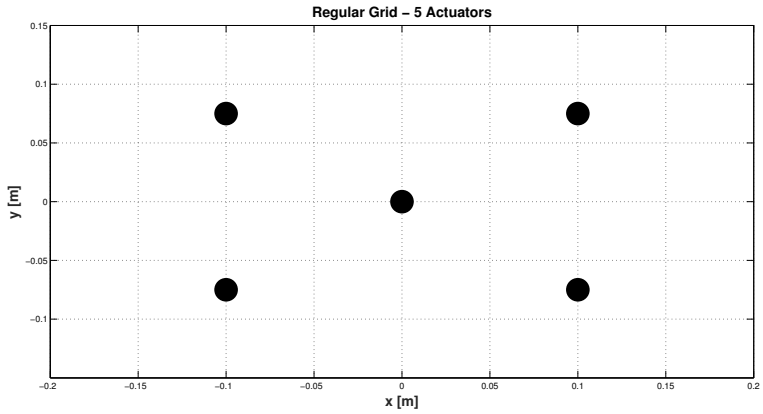

Figure 6.6: Assigned actuators positions for the CFSF M1 plate

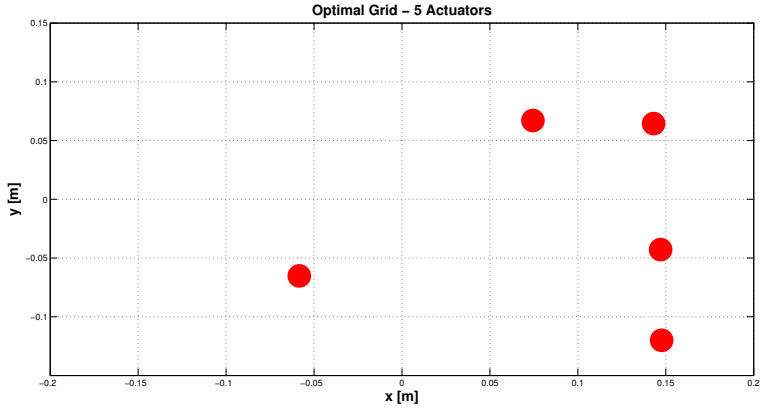

Figure 6.7: Optimal actuators positions for the CFSF M1 plate

Also in this case, the optimal grid approach guarantees a more distributed control action, capable of damping modes that are not controlled by the fixed grid configuration (Figure 6.8).

As an example, the modal shape related to the mode 12 is reported in Figure 6.9: the reader can see how the optimal grid configuration obtained from the optimization procedure presents actuators located in the proximity of peaks and valleys, resulting in a very effective damping action.

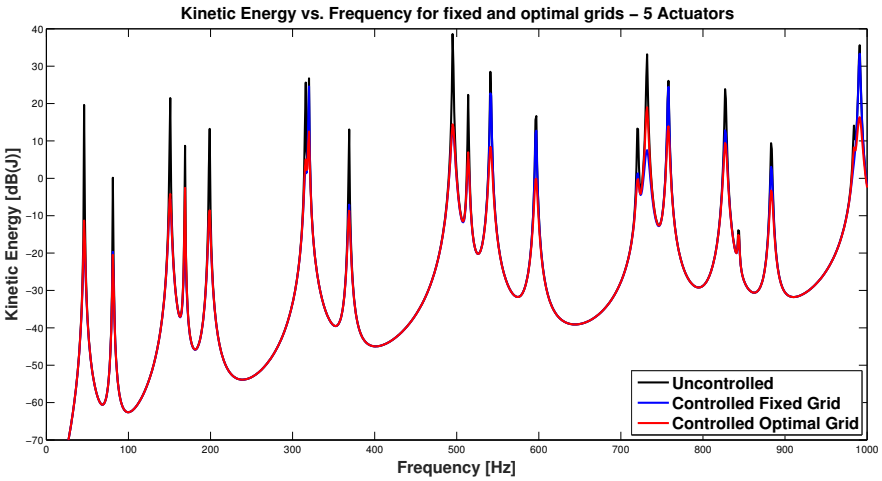

Figure 6.8: Kinetic energy versus frequency for fixed and optimal grid configurations - CFSF M1 plate - 5 Actuators

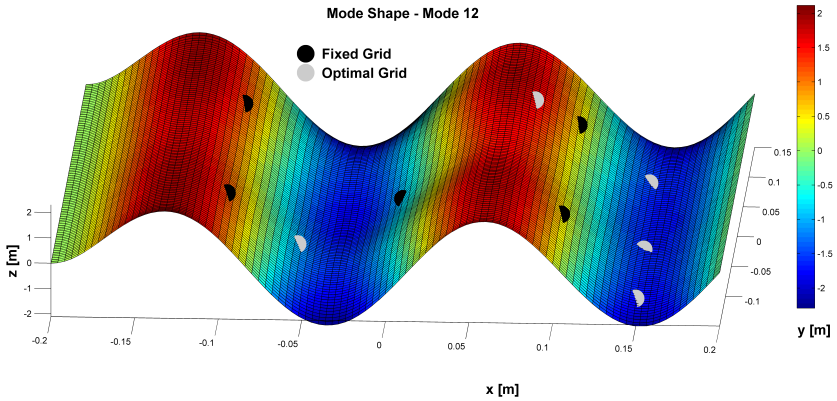

Figure 6.9: Mode shape - mode 12.

6.2 Fully clamped plate with 4 sensor/actuator pairs

Let's now consider a fully clamped, orthotropic (material M1) plate with 4 sensor/actuator pairs (Table 6.3). The model here considered takes into account all the dynamics described in Chapter 2. The plate is excited by a uniform distributed white noise disturbance. A weigthing value $W_{uu} = 1/1000$ on the control action is used.

Property	Description	Value
a	x dimension	0.5 m
b	y dimension	0.5 m
ζ	Modal damping factor	0.001
h	Thickness	0.002 m

Table 6.3: Properties of the CCCC M1 plate

Ten simulations are performed keeping the same parameters: the results in terms of sensor/actuator pairs placement and cost function obtained are presented in Figure 6.10.

As mentioned in the introduction to this chapter, it is possible to see how the solution of the positions optimization is not unique and a different pattern of the sensors/actuators grid is obtained for each simulation. However, all the results obtained correspond to similar values of the cost function, which guarantees that the optimization procedure always finds the same optimal compromise between performance and control.
A possible guideline to select one configuration among the others is to observe that each solution provides better damping of some modes compared to the others. Even if differences are not so pronounced, if we are interested in controlling some specific modes among the others, we can select the optimal solution that gives the best performance in that sense.

For example, looking at the spectrum of the kinetic energy for the case (i), shown in Figure 6.11, it is possible to see that this configuration provides a very good damping of the first five modes.

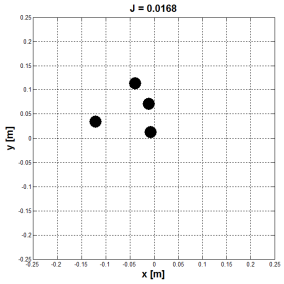

(a) J = 0.0168

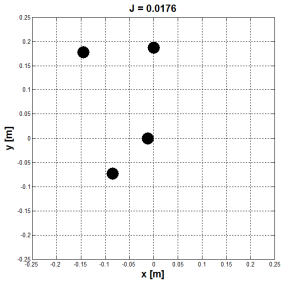

(b) J = 0.0176

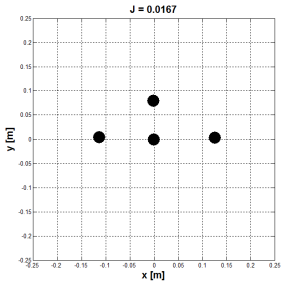

(c) J = 0.0167

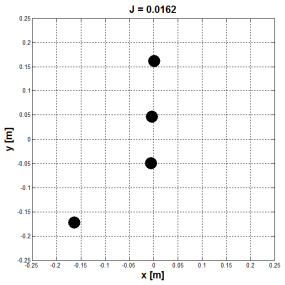

(d) J = 0.0162

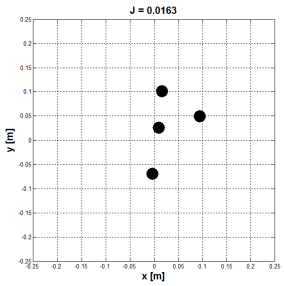

(e) J = 0.0163

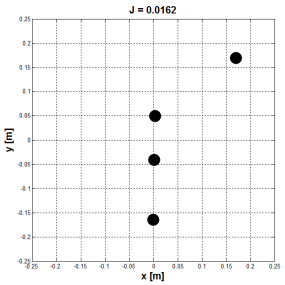

(f) J = 0.0162

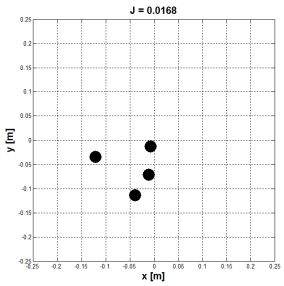

(g) J = 0.0168

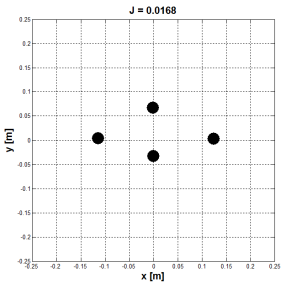

(h) J = 0.0168

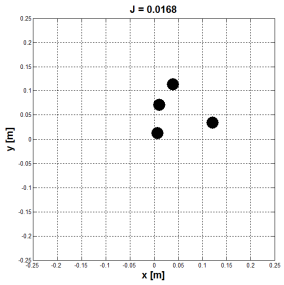

(i) J = 0.0168

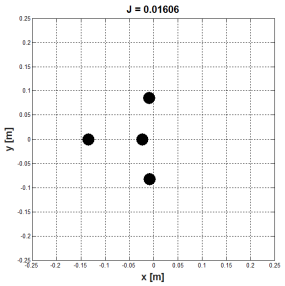

(j) J = 0.0161

Figure 6.10: Optimal sensor/actuator pairs placement obtained from different simulations with the same parameters - CCCC M0 plate - 4 Actuators

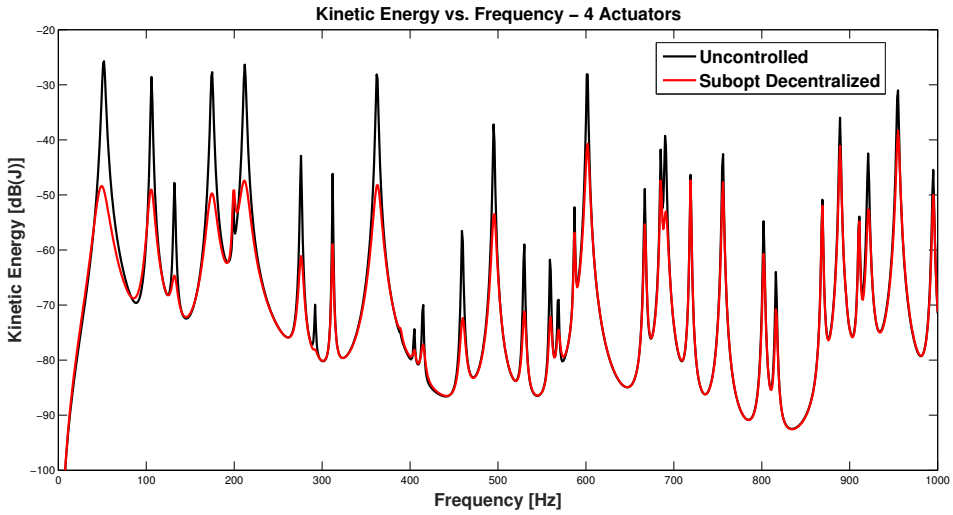

Figure 6.11: Uncontrolled and controlled kinetic energy versus frequency for the case (i) - CCCC M1 plate - 4 Actuators - $J = 0.0168$

Chapter 7

Results of structural acoustic control

Referring back to Chapter 3 for the acoustic model, in this chapter some examples of active structural acoustic control (ASAC) are presented. In particular, results obtained using as performance index the total kinetic energy or the total radiated sound power are discussed and compared in order to quantify the differences between the two approaches. The same considerations are made for assigned and optimal grids of collocated sensor/actuator pairs.
The weighting matrix $\mathbf{W}_{uu}$ is chosen diagonal with all equal elements of value W_{uu}, which is selected in order to comply with the maximum peak current limitation for the actuators considered. The performance weighting matrix $\mathbf{W}_{zz}$ is selected as the identity matrix.
A reduced order structural model with modes up to the frequency $f_{design}^{max} =$ 500 Hz is considered for the control design model, while the test model contains modes up to the frequency $f_{test}^{max} = 5000$ Hz. As respect to the acoustic model, a maximum frequency $f_{acoustic}^{max} = 500$ Hz is considered to perform the RME realization. Quite reasonably, if spillover doesn't show for the structural model, it is supposed that the same happens for the acoustic model. For this reason, the same reduced order radiation model is used both for the design and the test models. The number of significant modes is selected based on the convergence study presented in Chapter 8. In order to build the elementary radiators grid, 20 elementary radiators are used along the x direction, while 18 elements are used along the y direction for rectangular plates, 20 for the squared plates .
The reader can refer to Chapter 5 for the properties of sensors, actuators and materials used.
A randomly distributed white noise of unit intensity is chosen to excite the plate.

7.1 Differences among centralized, decentralized and equal gains control startegies with different number of actuators

The present example is aimed at showing how, even for the case of vibro-acoustic control, differences in terms of performances among decentralized with independent gains, centralized and decentralized with equal gains controllers are not so significant and the complication introduced by the centralized controller justify the fact that this approach is hardly ever used in control problems. In Figures 7.1 and 7.2, the results in terms of percentage variation of the cost function between centralized and decentralized controllers and between decentralized and equal gains controllers versus the number of actuators, are shown, for a fully clamped isotropic plate (properties in Table 7.1) with 9 sensor/actuator pairs. The radiated sound power is used as performance index to minimize and a weight $W_{uu} = 1/1000$ is used. It is possible to see how the percentage variations among the three types of control strategy are larger than those found in Chapter 2 for the vibration control. However, convergence times for the centralized approach remain very high compared to the other two types of controller (Figure 7.3).

Property	Description	Value
a	x dimension	0.8 m
b	y dimension	0.5 m
ζ	Modal damping factor	0.001 m
h	Thickness	0.002 m

Table 7.1: Properties of the CCCC M0 plate

The previous considerations and the fact that in real life centralized controllers may lead to an improper behavior in case of failure explain why decentralized control strategies are much more used.

7.2 Fully clamped isotropic plate with 9 sensor/actuator pairs in assigned positions

Let's consider the same fully clamped isotropic (material M0) plate of the previuos section (properties in Table 7.1), equipped with 9 sensor/actuator

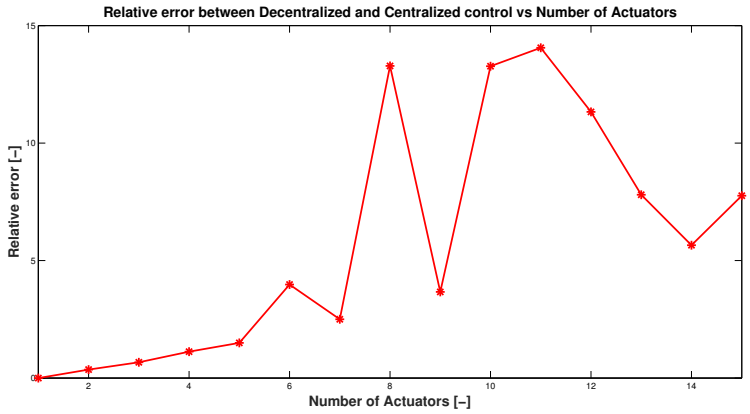

Figure 7.1: Percentage variation between Decentralized and Centralized controllers versus Number of Actuators - CCCC M0 plate

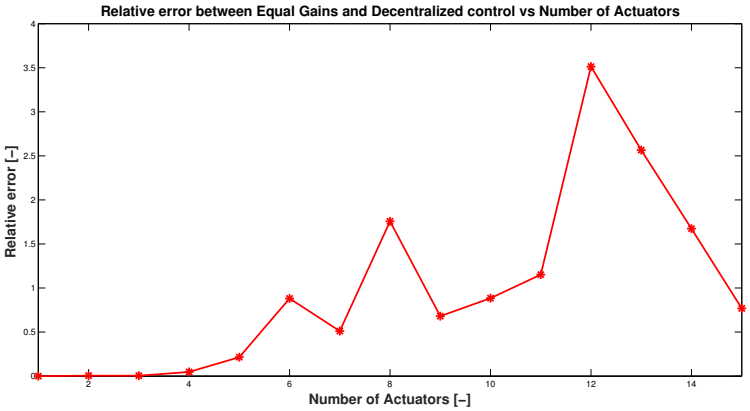

Figure 7.2: Percentage variation between Equal Gains and Decentralized controllers versus Number of Actuators - CCCC M0 plate

pairs located as in Figure 7.4. The dynamics of sensors and actuators are taken into account.

Let's perform an ASAC on the plate using as performance index the kinetic energy, first, and then the radiated acoustic power. Both designs are perfomed using a control weighting to obtain the same RMS values of the control currents. For the kinetic energy minimization, a value of $RMS_{curr}^{kin} = 0.4013$ A is obtained with a control weight $W_{uu} = 1/2500$, while, for the acoustic radiated power minimization, the value $RMS_{curr}^{rad} = 0.3832$ A is obtained with a control weight $W_{uu} = 1/1500$.

In this case, it is possible to see how the two types of minimizations

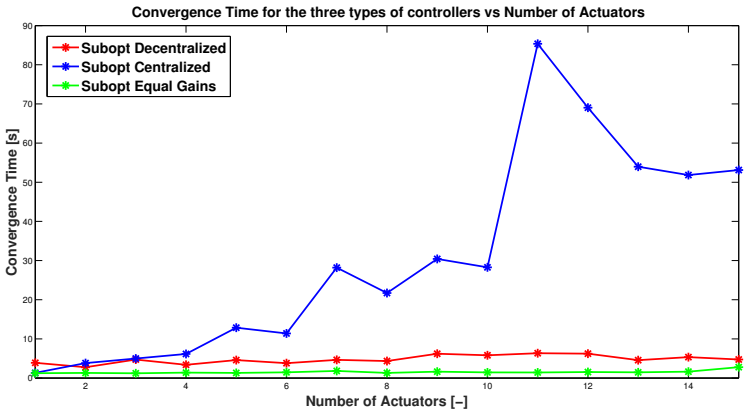

Figure 7.3: Convergence times for the three types of controller versus Number of Actuators - CCCC M0 plate

lead to very similar results in terms of kinetic energy and radiated sound power control (Figures 7.5 and 7.6). In particular, better results up to 3 dB for the vibration control performed using the kinetic energy as performance index are shown on modes 4,5 and 6. The same improvements are shown for the modes in the middle of the bandwith in the case of noise attenuation obtained by radiated sound power minimization . However, differences are not remarkable.

7.3 Simply supported orthotropic plate with 5 sensor/actuator pairs in assigned positions

Let's consider a simply supported orthotropic (material M1) plate, whose properties are listed in Table 7.2, equipped with 5 sensor/actuator pairs located as in Figure 7.7. The dynamics of sensors and actuators are taken into account.

Property	Description	Value
a	x dimension	0.5 m
b	y dimension	0.5 m
ζ	Modal damping factor	0.001 m
h	Thickness	0.002 m

Table 7.2: Properties of the SSSS M1 plate

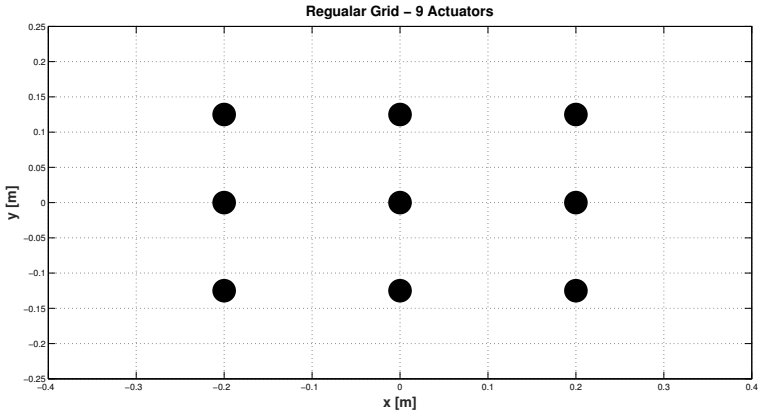

Figure 7.4: Assigned actuators positions on the CCCC M0 plate - 9 Actuators.

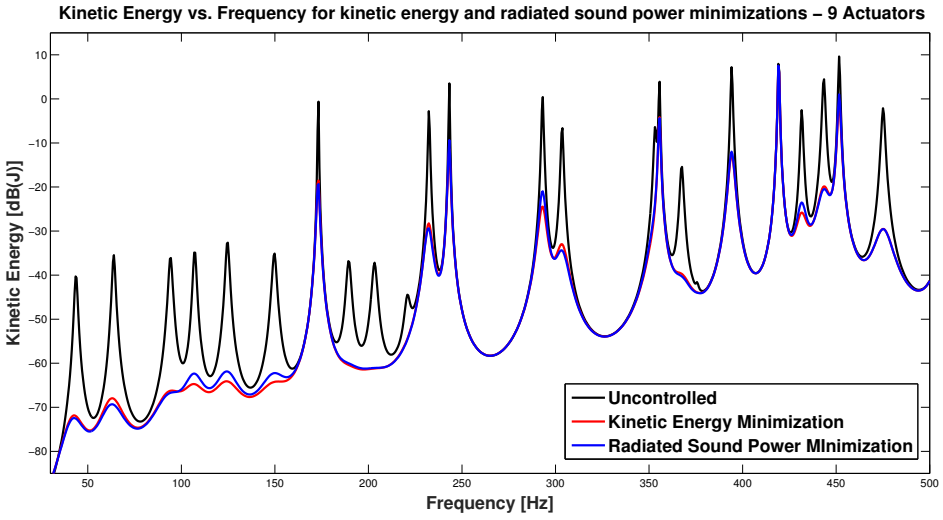

Figure 7.5: Uncontrolled and controlled kinetic energy versus frequency for kinetic energy and radiated sound power minimization indeces - CCCC M0 plate - 9 Actuators in assigned positions - $W_{uu} = 1/2500$.

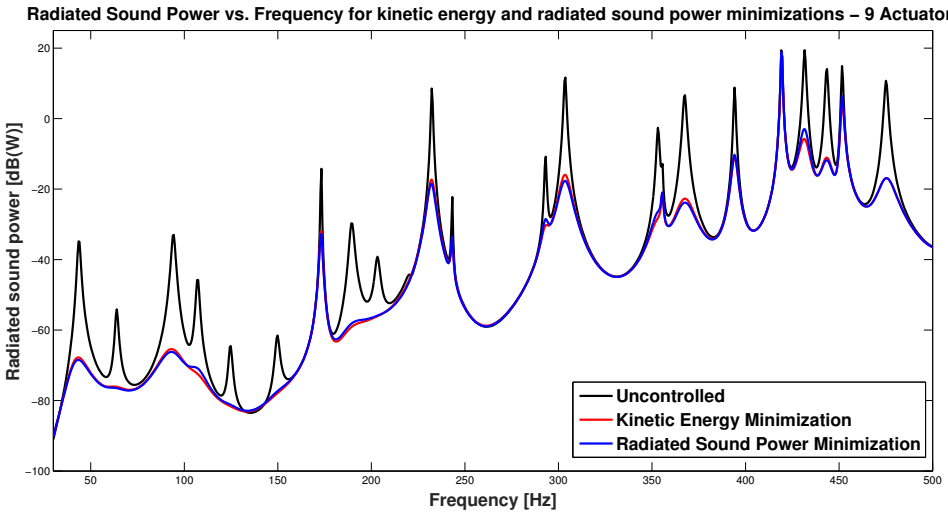

Figure 7.6: Uncontrolled and controlled radiated sound power versus frequency for kinetic energy and radiated sound power minimization indeces - CCCC M0 plate - 9 Actuators in assigned positions - $W_{uu} = 1/1500$.

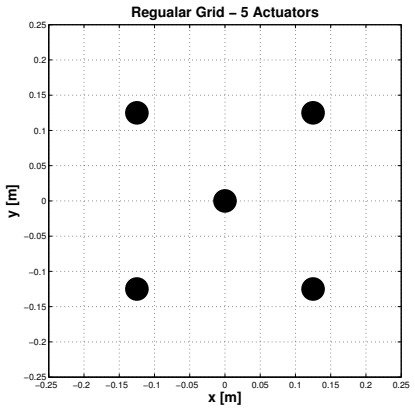

Figure 7.7: Assigned actuators positions on the SSSS M1 plate - 5 Actuators.

The results for the spectrum of the kinetic energy using the two minimization procedures are shown in Figure 7.8. Also in this case, the performances obtained with the two approaches differ in few decibels. The same considerations hold for the radiated sound power spectrum presented in Figure 7.9.

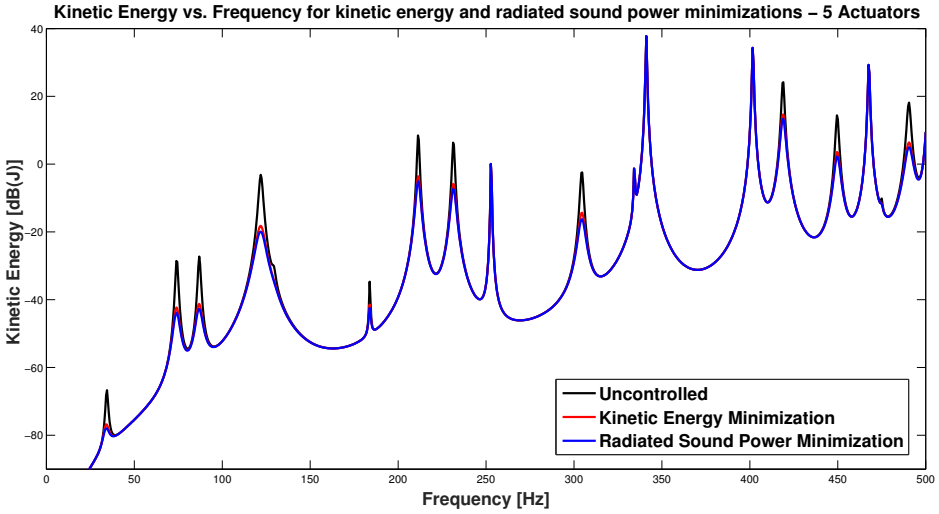

Figure 7.8: Uncontrolled and controlled kinetic energy versus frequency for kinetic energy and radiated sound power minimization indeces - SSSS M1 plate - 5 Actuators in assigned positions - $W_{uu} = 1/500$.

Therefore, it seems that performing an optimization with an approach rather than the other doesn't lead to significant improvements in the results. However, in the following, it is shown that, if an optimal sensor/actuator placement tecnique is used, remarkable differences arises between the two minimization approaches.

7.4 Fully clamped isotropic plate with 5 ideal sensor/actuator pairs in optimal positions

Let's consider the same fully clamped isotropic plate of the previous example (see Table 7.1), equipped with 5 ideal sensor/actuator pairs located by an optimal placement technique.
For the kinetic energy minimization approach a weight $W_{uu} = 1/600$ is used, while the acoustic sound power minimization is performed with $W_{uu} = 1/500$. This guarantees similar control currents values in the two cases.
Very important differences are shown in the two minimization approaches

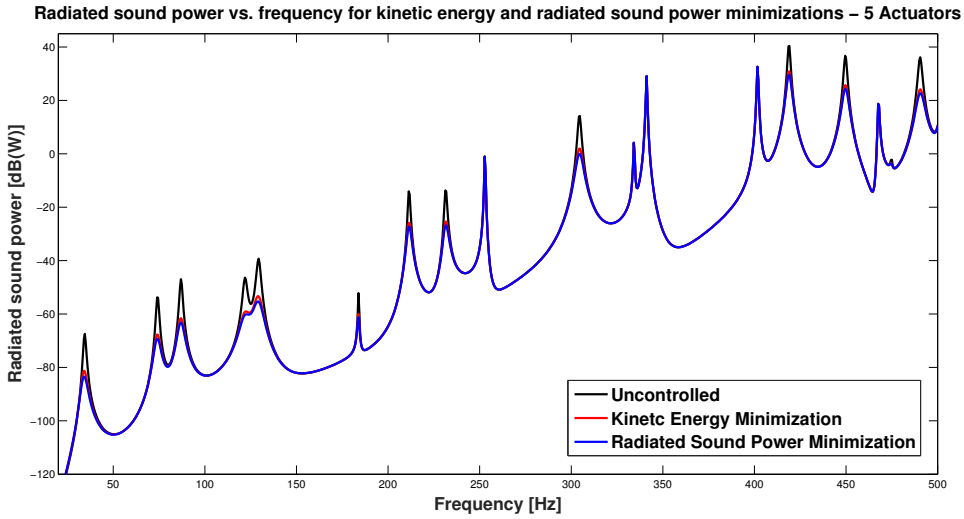

Figure 7.9: Uncontrolled and controlled radiated sound power versus frequency for kinetic energy and radiated sound power minimization indeces - SSSS M1 plate - 5 Actuators in assigned positions - $W_{uu} = 1/200$.

here considered. As shown in Figure 7.10, the controlled kinetic energy presents strong differences (up to 12-14 dB) on some modes using a minimization technique rather than the other. Moreover, for the first two modes and the sixth mode, it appears that the sound power minimization approach works better, while, for the other modes, the level of damping obtained minimizing the kinetic energy is definitely better. The same consideratons hold for the noise control, whose results in terms of the spectrum of radiated sound power are shown in Figure 7.11. For example, using a sound power minimization approach, the radiated power magnitude corresponding to the sixth mode is reduced 14 dB more compared to the other minimization approach, which consists in a remarkable difference perceived by the human ear.
This example shows how, in this case, the optimal solution for the vibration damping doesn't provide an optimal solution in terms of noise attenuation and viceversa and, depending on the mode considered, one of the two approaches may lead to better results both in terms of kinetic energy and radiated sound power minimization.

The two grids of sensor/actuator pairs obtained by the optimization procedure are shown in Figures 7.12 and 7.13.

It must be pointed out that another possible reason why the two simulations lead to very different results is the non-uniqueness of the solution for the optimal placements of sensors and actuators. However, several simula-

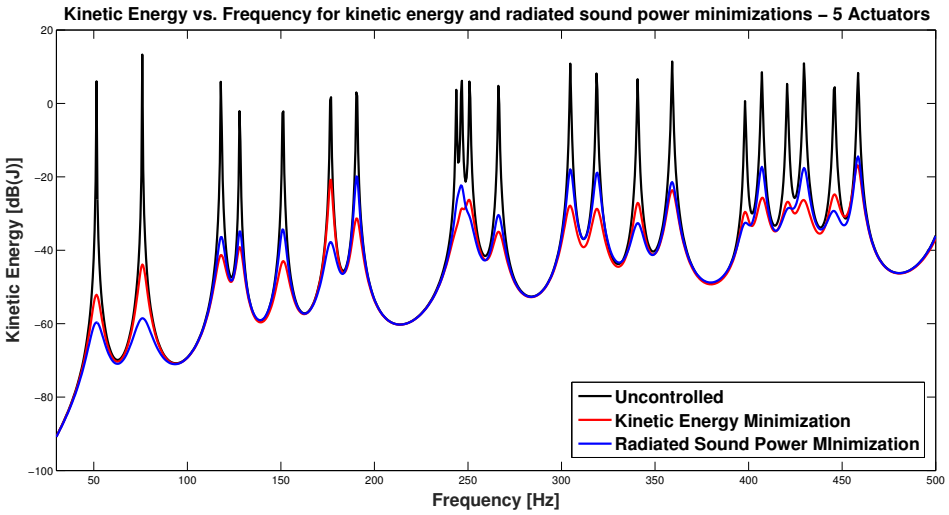

Figure 7.10: Uncontrolled and controlled kinetic energy versus frequency for kinetic energy and radiated sound power minimization indeces - CCCC M0 plate - 5 Actuators in optimal positions - $W_{uu} = 1/600$.

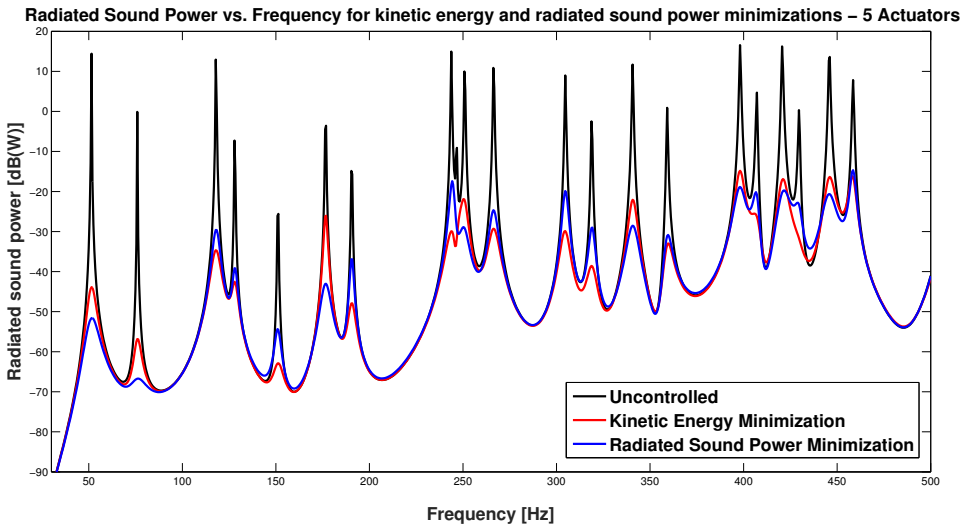

Figure 7.11: Uncontrolled and controlled radiated sound power versus frequency for kinetic energy and radiated sound power minimization indeces - CCCC M0 plate - 5 Actuators in optimal positions $W_{uu} = 1/500$.

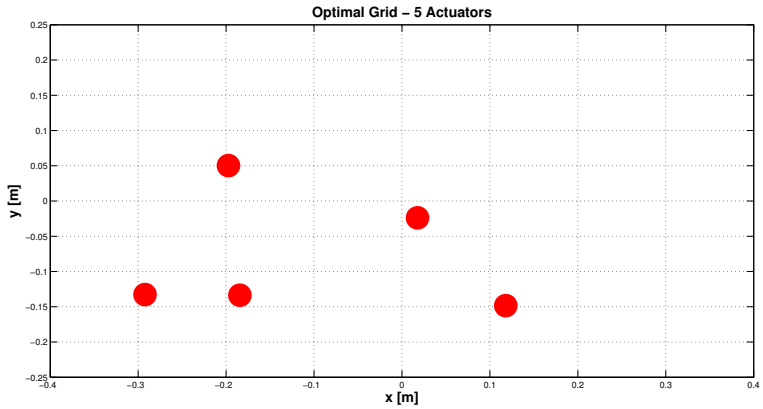

Figure 7.12: Optimal actuators positions on the CCCC M0 plate for kinetic energy minimization - 5 Actuators .

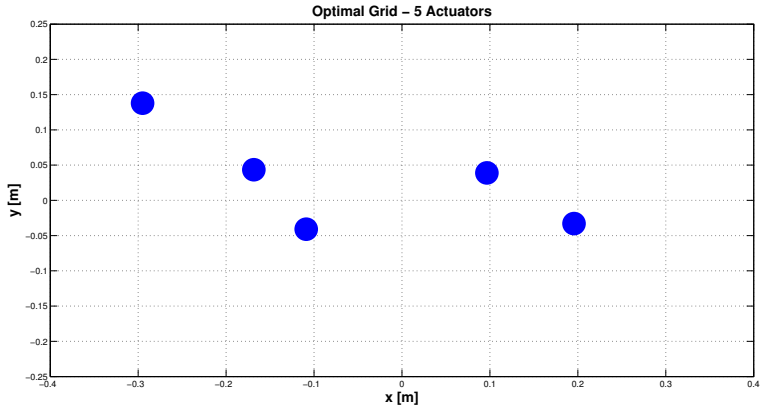

Figure 7.13: Optimal actuators positions on the CCCC M0 plate for radiated sound power minimization - 5 Actuators.

tions has shown slight differences between the optimal solutions obtained and the trend of kinetic energy and radiated sound power for the two difference apporoaches described have been confirmed.

7.5 Simply supported orthotropic plate with 5 ideal sensor/actuator pairs in optimal positions

Let's now consider the same simply supported orthotropic (material M1) plate of the previous example (see Table 7.2), equipped with 5 ideal sensor/actuator pairs located by an optimal placement technique (Figures 7.14 and 7.15).

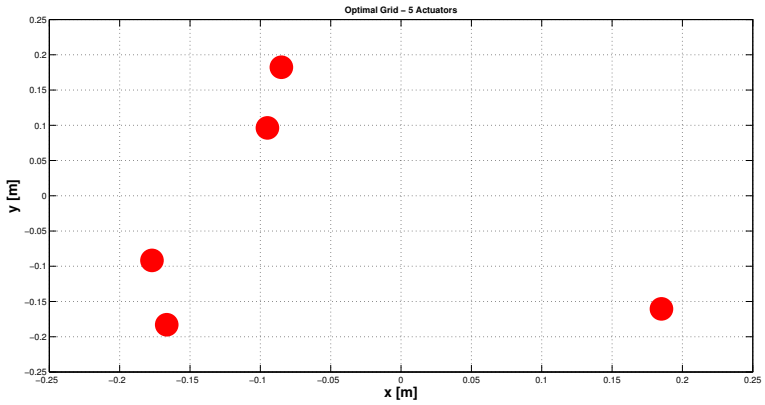

Figure 7.14: Optimal actuators positions on the SSSSS M0 plate for kinetic energy minimization - 5 Actuators .

The spectra of the kinetic energy and the radiated sound power are shown in Figures 7.16 and 7.17. Control weigths $W_{uu} = 1/300$ and $W_{uu} = 1/360$ are used, respectively.

As discussed in the previous example, also in this case it is possible to see how, depending on the minimization approach used, the optimal solution obtained is different. For example, the first two modes are controlled very well optimazing the controller configuration for the minimization of the radiated acoustic power and this leads to a decrease of $6-7$ dB of the noise produced with respect to a configuration obtained minimizing the kinetic energy.

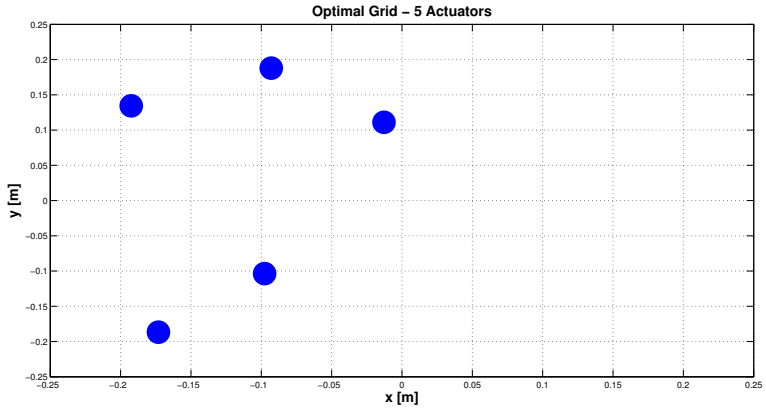

Figure 7.15: Optimal actuators positions on the SSSS M0 plate for radiated sound power minimization - 5 Actuators.

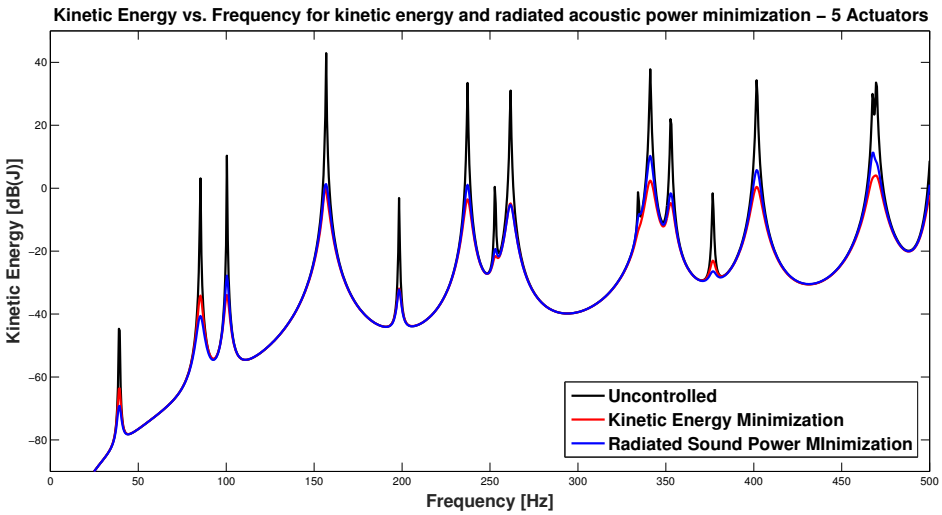

Figure 7.16: Uncontrolled and controlled kinetic energy versus frequency for kinetic energy and radiated sound power minimization indeces - SSSS M1 plate - 9 Actuators in optimal positions - $W_{uu} = 1/300$.

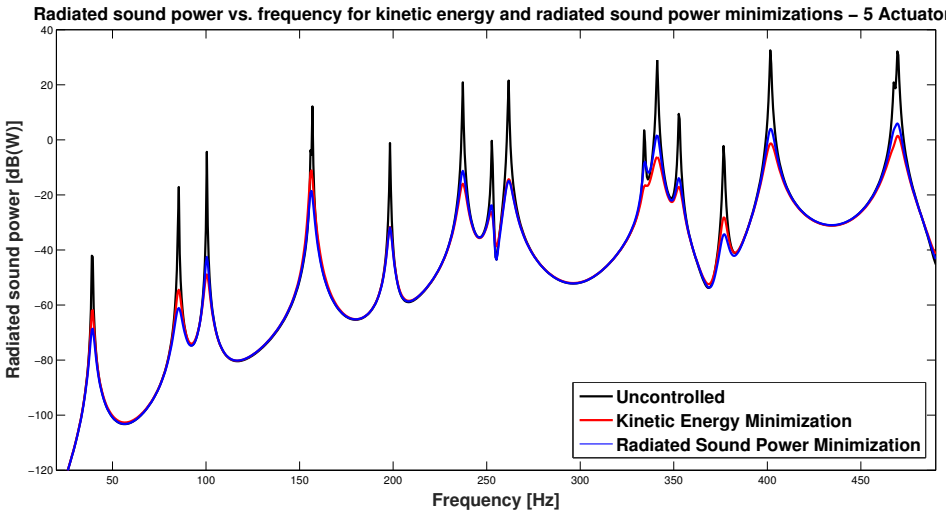

Figure 7.17: Uncontrolled and controlled radiated sound power versus frequency for kinetic energy and radiated sound power minimization indeces - SSSS M1 plate - 9 Actuators in optimal positions - $W_{uu} = 1/360$.

Therefore, depending on which performance we want to optimize, the suitable minimization approach should be selected.

Chapter 8

Convergence study

In order to validate the results obtained in the previous chapters, a study of convergence of the methods used is carried out, without control simulation, both for the structural and the acoustic model. Plates with all the combinations of boundary conditions used in the previous chapters are here considered. Some convergence results are also compared with references from the literature in order to validate both the structural and the acoustic models. For the other examples the only plots in which convergence is reached are shown.
A bandwidth of 10 kHz will be considered for the convergence analysis of the structural model, while the convergence of the RME model is verified for a bandwidth up to 500 Hz.
For the present work, good accuray of the model used may be required only in the control bandwidth, which is usually up to 1 kHz or less, while only discrete convergence properties on the other modes can be sufficient in order to perform simple spillover tests. However, a number of Ritz functions sufficient to guarantee good accuracy all over the bandwidth is chosen.

8.1 Validation and convergence analysis of the structural model

In this section convergence solutions for a clamped and a simply supported plates are compared with reference cases available in the literature. Then, convergence studies are presented for the following cases:

- a fully clamped isotropic (material M0) plate

- a cantilever orthotropic (material M1) plate
- a simply supported orthotropic (material M1) plate
- a CFSF orthotropic (material M1) plate

Convergence is shown through plots of both the spectrum of kinetic energy and the frequency response of the system.
All the plates are considered equipped with a sensor/actuator pair with the properties presented in Chapter 5 and whose dynamics is taken into account. Results are obtained by using a square selection strategy, i.e., the same number of terms M = N is adopted in the series.

8.1.1 Validation of the structural model

In order to validate the structural model used, the first six frequency parameters $\lambda = \omega a^2\sqrt{\rho h/D_{11}}$ of square orthotropic plates (material M1) carrying an elastically mounted mass M_a with dimensionless spring constant $K_0 = K_a ab/D_{11}$ will be presented and compared with two references in literature, Dozio [6] and Bambill et al. [3].
Note that ω is the natural pulsation corresponding to the mode considered and M_p is the plate mass. In Table 8.1 the comparisons are shown for a simply supported plate and in Table 8.2 a fully clamped plate is considered. Good agreement among the results can be seen.

Reference	Mode sequence					
	1	2	3	4	5	6
Present	9.34771	21.2068	43.4712	51.1890	79.7635	79.9378
Dozio [6]	9.34718	21.2066	43.4711	51.1890	79.7630	79.9378
Bambill et al. [3]	9.34828	21.2070	43.4711	51.1889	79.7626	79.9377

Table 8.1: First six frequency parameters $\lambda = \omega a^2\sqrt{\rho h/D_{11}}$ of a square, simply supported, orthotropic (material M1) plate carrying an elastically mounted mass $M_a = 0.1M_p$ with dimensionless spring constant $K_0 = K_a ab/D_{11} = 10$, in position (0,0)

Reference	Mode sequence					
	1	2	3	4	5	6
Present	5.59411	34.4230	61.5623	73.5962	103.841	104.580
Dozio [6]	5.59375	34.4223	61.5602	73.5938	103.835	104.574
Bambill et al. [3]	5.5940	34.422	61.558	73.592	-	-

Table 8.2: First six frequency parameters $\lambda = \omega a^2\sqrt{\rho h/D_{11}}$ of a square, fully clamped, orthotropic (material M1) plate carrying an elastically mounted mass $M_a = 0.3M_p$ with dimensionless spring constant $K_0 = K_a ab/D_{11} = 10$, in position (0,0)

8.1.2 Convergence study for a fully clamped isotropic plate

Let consider a fully clamped, isotropic (material M0) plate, whose properties are listed in Table 8.3.

Property	Description	Value
a	x dimension	0.8 m
b	y dimension	0.5 m
ζ	Modal damping factor	0.001
h	Thickness	0.002 m

Table 8.3: Properties of the CCCC M0 plate

The frequency response and the spectrum of the kinetic energy are shown in Figures 8.1 and 8.2, for different number of Ritz functions used. Although good accuracy in the bandwidth up to 1 kHz is obtained with a small number of admissible functions, good convergence properties all over the bandwidth can be reached including more trial functions in the model. Using 36 Ritz functions for each dimension the accuracy of the model seems to be very good.

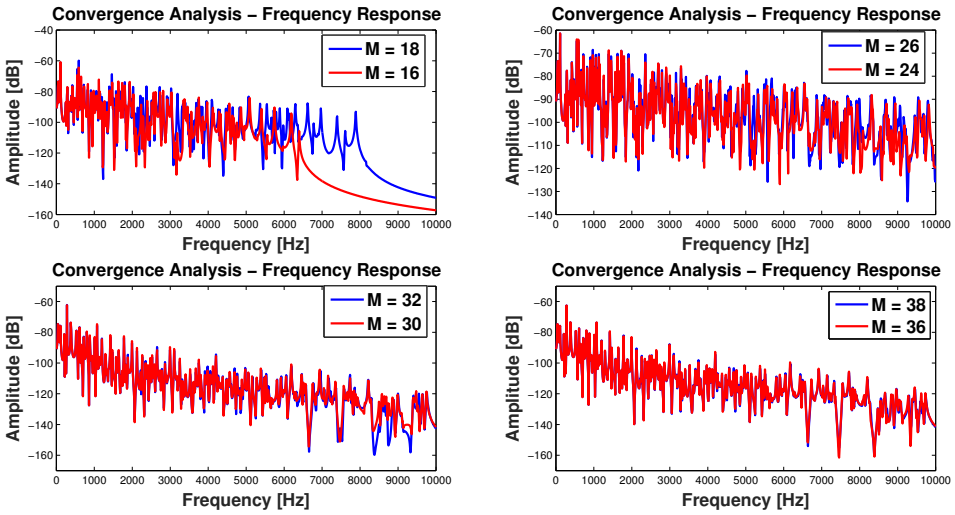

Figure 8.1: Frequency response for different numbers N = M of Ritz functions - 627 modes considered - CCCC M0 plate

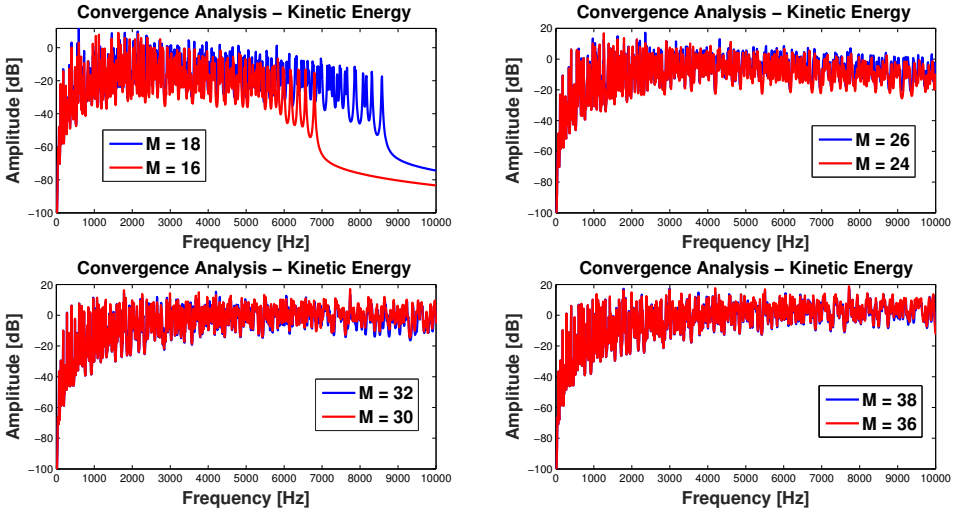

Figure 8.2: Spectrum of kinetic energy for different numbers N = M of Ritz functions - 627 modes considered - CCCC M0 plate

8.1.3 Convergence study for a cantilever orthotropic plate

The properties of the plate considered in this example are listed in Table 8.4.

Property	Description	Value
a	x dimension	0.25 m
b	y dimension	0.25 m
ζ	Modal damping factor	0.001
h	Thickness	0.003 m

Table 8.4: Properties of the CFFF M1 plate

The convergence plots of the frequency response and of the spectrum of the kinetic energy are shown in Figures 8.3 and 8.4: in order to have a good approximation all over the bandwith considered, 34 terms must be adopted in the series expansion of the Ritz functions. In the control bandwidth, which is up to 1000 Hz, the model is very accurate.

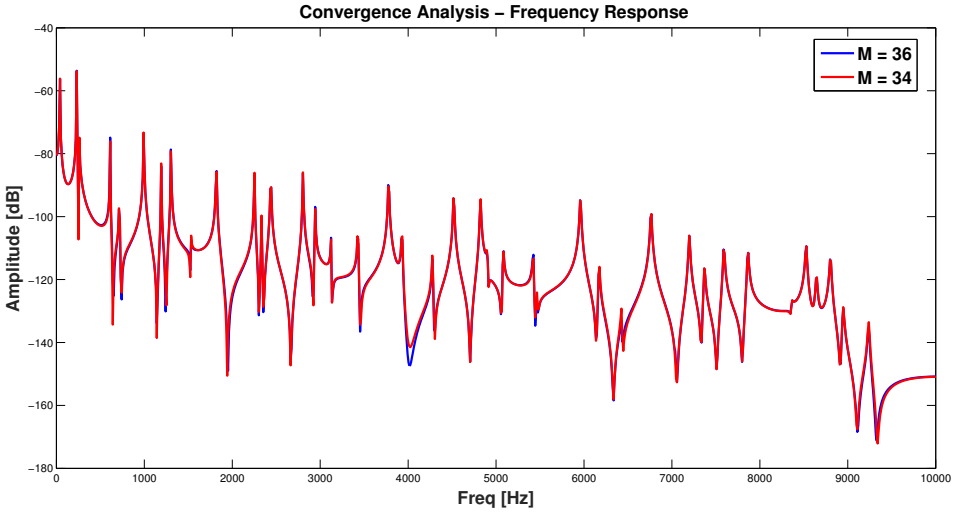

Figure 8.3: Frequency response for N = M = 34 and N = M = 36 Ritz functions - 79 modes considered - CFFF M1 plate

8.1.4 Convergence study for a simply supported orthotropic plate

The properties of the plate considered in this example are listed in Table 8.5.

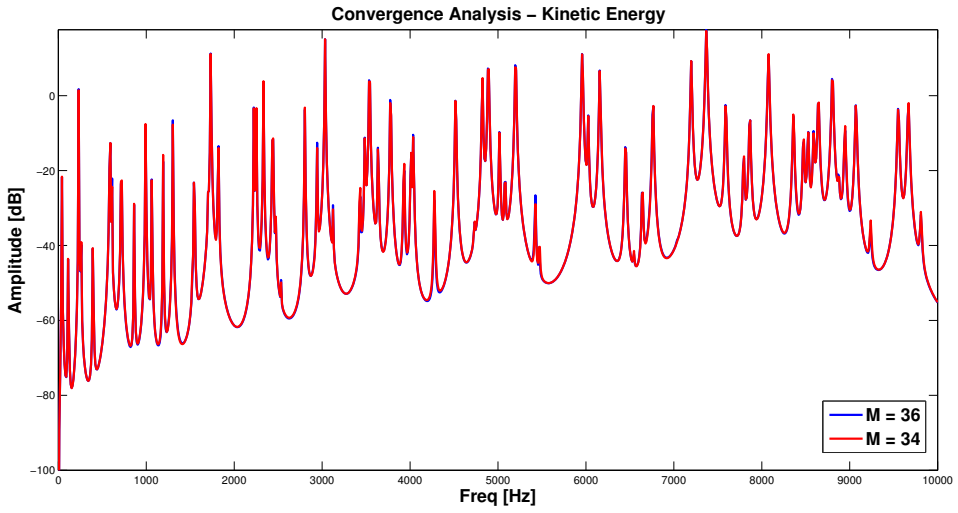

Figure 8.4: Spectrum of kinetic energy for N = M = 34 and N = M = 36 Ritz functions - 79 modes considered - CFFF M1 plate

Property	Description	Value
a	x dimension	0.4 m
b	y dimension	0.4 m
ζ	Modal damping factor	10^{-4}
h	Thickness	0.003 m

Table 8.5: Properties of the SSSS M1 plate

The convergence plot of the frequency response and of the spectrum of the kinetic energy are shown in Figures 8.5 and 8.6: in order to have a good approximation all over the bandwith considered, 32 terms must be adopted in the series expansion for the Ritz functions. Also in this case, the number of admissible functions chosen guarantees a very good accuray of the model in the control bandwidth.

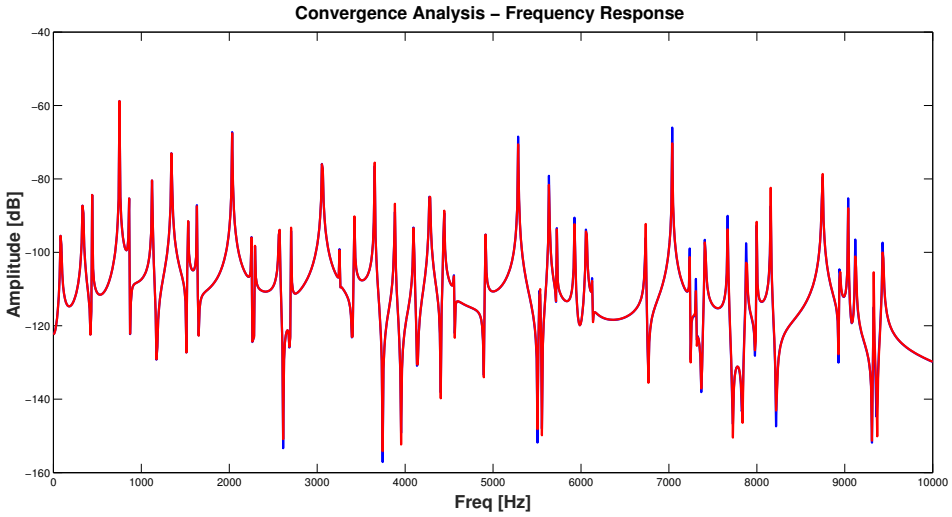

Figure 8.5: Frequency response for N = M = 32 and N = M = 34 Ritz functions - 172 modes considered - SSSS M1 plate

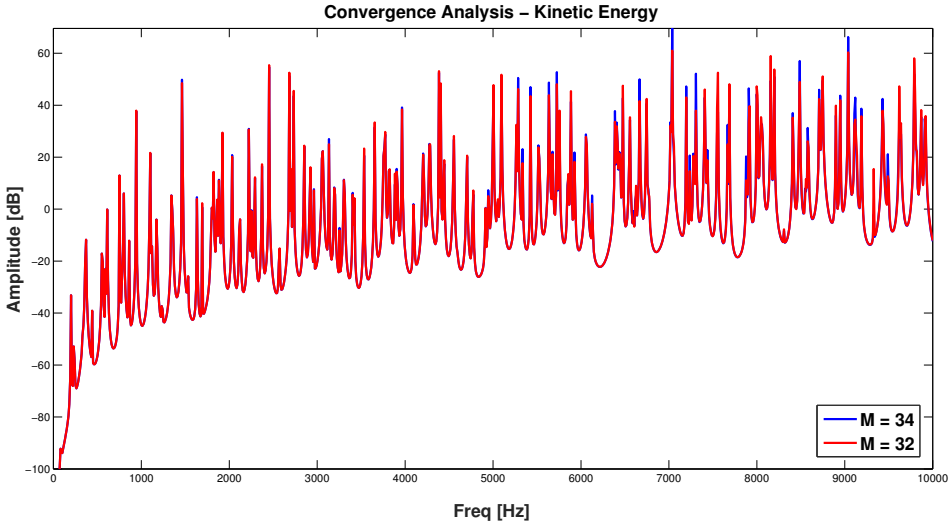

Figure 8.6: Spectrum of kinetic energy for N = M = 32 and N = M = 34 Ritz functions - 172 modes considered - SSSS M1 plate

8.1.5 Convergence study for a CFSF orthotropic plate

The properties of the plate considered in this example are listed in Table 8.6.

Property	Description	Value
a	x dimension	0.4 m
b	y dimension	0.3 m
ζ	Modal damping factor	0.001
h	Thickness	0.002 m

Table 8.6: Properties of the CFSF M1 plate

The convergence plot of the frequency responce and of the spectrum of the kinetic energy are shown in Figures 8.7 and 8.8: in order to have a good approximation all over the bandwith condidered, 30 terms must be adopted in the series expansion of the Ritz functions. For the control bandwidth, which is usually of 1000 Hz, the model is very accurate.

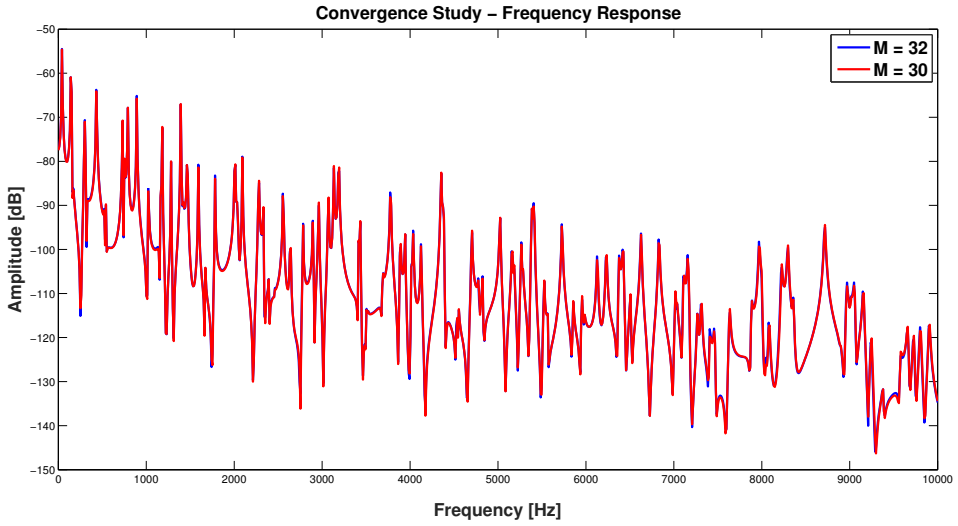

Figure 8.7: Frequency response for N = M = 30 and N = M = 32 Ritz functions - 213 modes considered - CFSF M1 plate

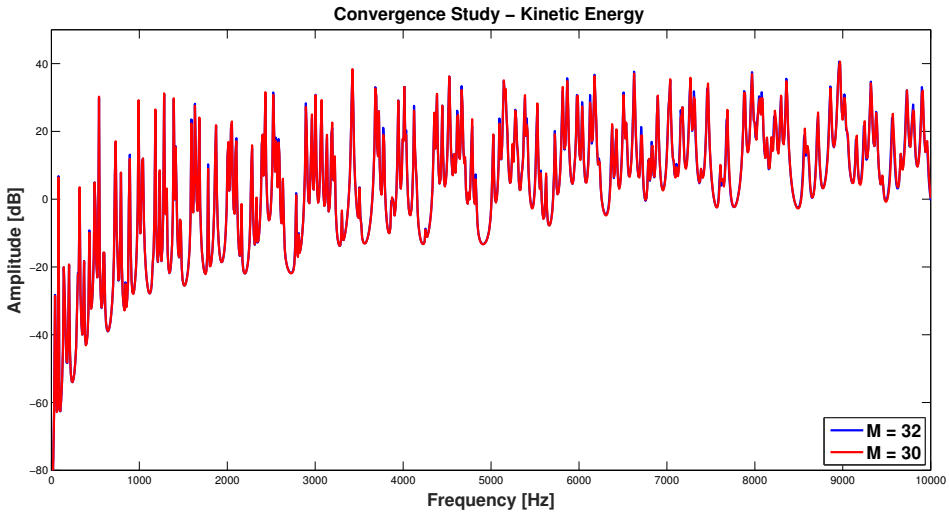

Figure 8.8: Spectrum of kinetic energy for N = M = 30 and N = M = 32 Ritz functions - 213 modes considered - CFSF M1 plate

8.2 Validation and convergence analysis of the radiation model

In this section some convergence studies of the RME model are presented. In particular, an example of evaluation of eigenvalues and amplitude weighting coefficients for an aluminium simply supported plate is compared to references in the literature in order to validate the radiation model used. Then, plots of the radiated sound power evaluated by the RME tecnique for a number of significant modes that guarantees convergence are shown. All the analyses are performed using a number of Ritz functions that guarantees the convergence of the structural model of the plates considered.

8.2.1 Validation of the radiation model

In order to validate the radiation model used, let's consider an aluminium simply supported plate, whose porperties are listed in Table 8.7.

Property	Description	Value
a	x dimension	0.355 m
b	y dimension	0.254 m
ζ	Modal damping factor	0.001 m
h	Thickness	0.001 m
E	Young's Modulus	71 x 10^9 Pa
ρ	Density	2700 Kg/m^3
ν	Poisson's ratio	0.33

Table 8.7: Properties of the SSSS aluminium plate .

In Figure 8.9 the first six eigenvalues of the Radiated Resistance Matrix **R** (see Chapter 3) are plotted versus frequency (a) and compared with a reference in the literature (b). It is shown a good agreement between the two results.

The amplitue-weighting coefficients for the same plate evaluated through the RME technique are shown in Figure 8.10 and compared to the ones obtained by Gibbs et al. [9]. Also in this case the agreement between the two results is good.
Therefore, both the radiation element model and the RME model results are comparable to the ones present in the literature.

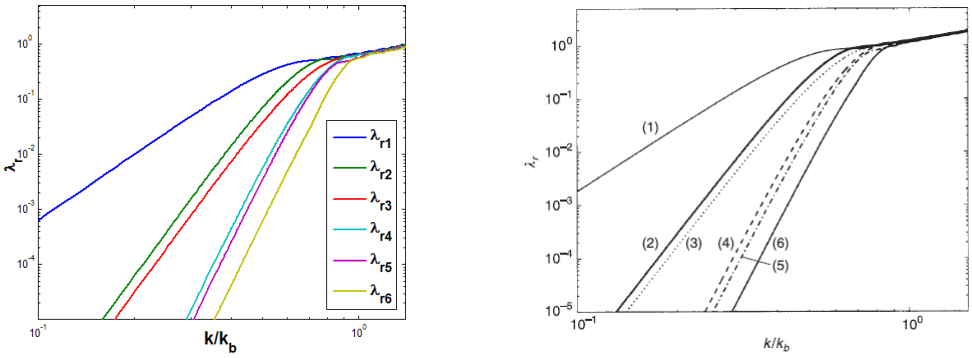

(a) Present (b) Fahy and Gardonio [8]

Figure 8.9: First six eigenvalues of the radiation model of an aluminium baffled simply supported plate versus the parameter k/k_b, with $k = \omega/c$ and $k_b = \frac{\omega^2 M_p}{EI}^{0.25}$. ω is the natural pulsation, c the speed of sound in air, M_p the plate mass, E the Young's Modulus, I the moment of inertia the plate - Aluminium SSSS plate

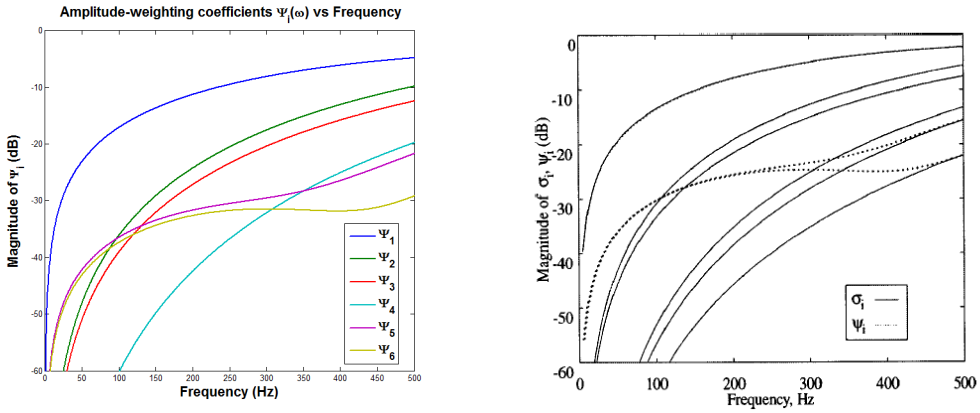

(a) Present (b) Gibbs et al. [9]

Figure 8.10: First six amplitue-weighting coefficients evaluated through the RME technique for an aluminium baffled simply supported plate versus frequency - Aluminium SSSS plate

8.2.2 Convergence study for a fully clamped isotropic plate

The properties of the plate considered in this example are listed in Table 8.8.

Property	Description	Value
a	x dimension	0.8 m
b	y dimension	0.5 m
ζ	Modal damping factor	0.001
h	Thickness	0.002 m

Table 8.8: Properties of the CCCC M0 plate

The convergence of the radiation filters model reduced by the RME technique is shown through Figure 8.11, where the radiated sound power spectrum obtained with different numbers significant modes considered in the RME model is represented. 20 radiators elements are used on the x-wise direction, 18 along the y-wise direction. A maximum frequency $f_{max} = 500$ Hz is used to perform the RME realization. It is shown that using 10 significant radiation modes the convergence is reached.

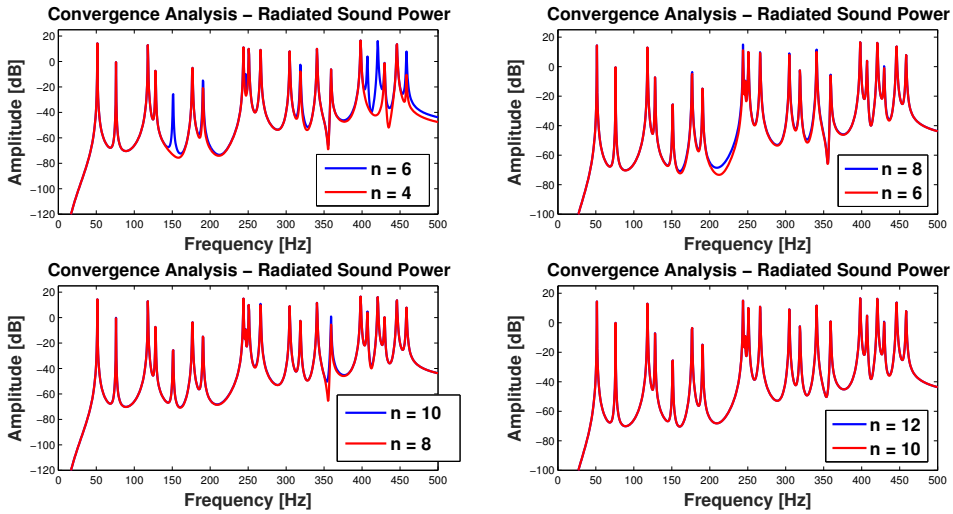

Figure 8.11: Spectrum of radiated sound power for different numbers n of significant modes - $f_{max} = 500$ Hz - CCCC M0 plate

8.2.3 Convergence study for a simply supported orthotropic plate

The properties of the plate considered in this example are listed in Table 8.9.

Property	Description	Value
a	x dimension	0.5 m
b	y dimension	0.5 m
ζ	Modal damping factor	0.001
h	Thickness	0.002 m

Table 8.9: Properties of the SSSS M1 plate

In Figure 8.12 the radiated sound power spectrum obtained with 10 and 12 significant modes considered is represented. 20 radiators elements are used on the x-wise direction, 20 along the y-wise direction. A maximum frequency $f_{max} = 500$ Hz is used to perform the RME realization. It is shown that the two curves are perfectly overlapping, hence the model is at convergence.

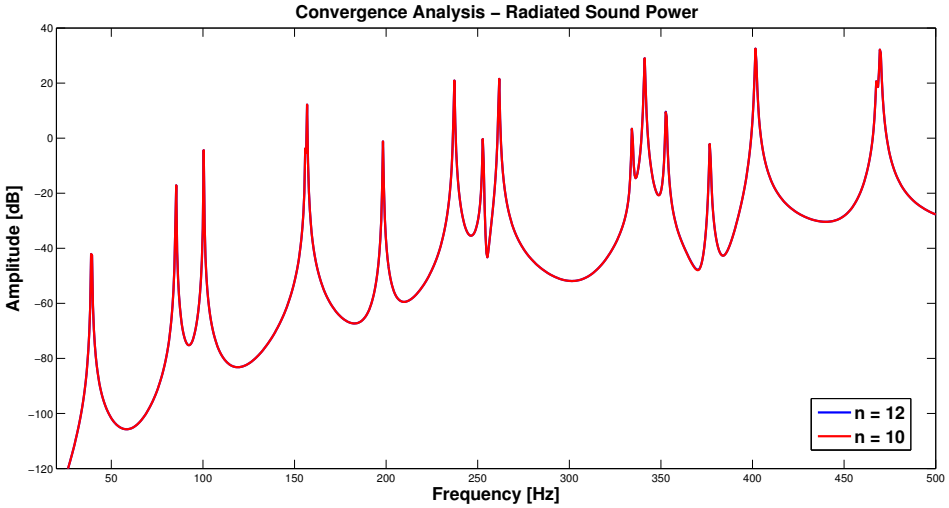

Figure 8.12: Spectrum of radiated sound power for $n = 10$ and $n = 12$ significant modes - $f_{max} = 500$ Hz - SSSS M1 plate

Chapter 9

Conclusions

Several examples related to the active vibro-acoustic control of rectangular plates have been presented in this work, with the aim of showing some aspects of this important field of engineering.
First of all, the dynamics of inertial actuators and integrators was introduced in order to provide a more realistic model, allowing to consider real control efforts in terms of control currents and taking into account real limitations of the actuators.
A study was done on three different types of suboptimal control (decentralized with independent gains, centralized and decentralized with equal gains) in order to show differences, advantages and drawbacks. It was shown through some examples that the centralized controller gives slightly better results compared to the other two approaches, but the level of complexity and the high computational cost for its design are significant drawbacks for its use for the control of a simple plate.
Active vibration results were obtained using a minimization procedure which is capable of providing not only optimal gains but also optimal positions of sensors and actuators, showing the advantages of this approach in terms of more uniform control action on the bandwidth considered. Moreover, it was pointed out that the solution of the sensor/actuator placement optimization is non-unique, but, for the same plate configuration, comparable results in terms of performance and control are obtained with the different sensor/actuator grid solutions.
Finally, results for the actve structural acoustic control were presented using two types of minimization approach, based on the use of the kinetic energy or the radiated sound power as performance index to minimize. It was shown that, in case of assigned grid of sensor/actuator pairs, the two approaches provide only slight differences in terms of vibration and noise control. On

the contrary, it was shown that, using an optimal sersor/actuator placement technique, important differences arise in the use of a minimization approach rather than the other and the optimal solution for the vibration damping doesn't provide an optimal solution in terms of noise attenuation and viceversa.

9.1 Future developments

This work presents a large variety of aspects that can be improved or adapted to different types of applications and challenging situations.

Here follows, as an example, a small list of topics that can be taken as a direction path for future research works:

- Improvement of the numerical optimization technique using Hessian based methods, instead of a Gradient based one.
- Consider non-collocated sensors and actuators, improving the numerical optimization procedure in order to obtain good and reliable results.
- Use piezoelectric actuators instead of inertial actuators to control the plates.
- Consider plates made of other materials, like laminated composite plates.
- Include a new type of plate geometry.

Bibliography

[1] Micromega Dynamics SA. URL `http://www.micromega-dynamics.com/`.

[2] PCB Piezotronics, Inc. URL `http://www.pcb.com/`.

[3] D. V. Bambill, D. H. Felix, and C.A. Rossit. "Natural frequencies of thin rectangular plates with holes or orthotropic patches carrying an elastically mounted mass.". *International Journal of Solids and Structures*, 43(-):4116Ű35, July 2006.

[4] Oliver N. Baumann and Stephen Stephen J. Elliot. "The stability of decentralized multichannel velocity feedback controllers using inertial actuators.". *Journal of Acoustical Society of America*, 121(1):188–196, January 2007.

[5] O. Beslin and J. Nicolas. "A hierarchical functions set for predictin very high order plate bending modes with any boundary conditions.". *Journal of Sound and Vibration*, 202, 1997.

[6] Lorenzo Dozio. "On the use of the Trigonometric Ritz method for general vibration analysis of rectangular Kirchoff plates". *Thin-Walled Structures*, 49:129–144.

[7] Wouter P. Engels, Oliver N. Baumann, and Stephen J. Elliot. "Centralized and decentralized control of structural vibration and sound radiation.". *2000 Acoustic Society of America*, 119(3):1487–1495, March 2006.

[8] F.J. Fahy and P. Gardonio. *"Sound and Structural Vibration (2nd edn).".* Academic Press - Elsevier, 2007.

[9] Gary P. Gibbs, Robert L. Clark, David E. Cox, and Jeffrey S. Vipperman. "Radiation modal expansion: Application to active structural acoustic control.". *Journal of Acoustical Society of America*, 107(1): 332–339, 2000.

[10] Steven Griffin, Steven A. Lane, Colin Hansen, and Ben Cazzolato. "Active Structural-Acoustic Control of a Rocket Fairing Using Proof-Mass Actuators.". *Journal of Spacecraft and Rockets*, 38(2), March-April 2001.

[11] Arthur W. Leissa. "The free vibration of rectangular plates". *Journal of Sound and Vibration*, 31, 1973.

[12] K. Xu, P. Warnitchai, and T. Igusa. "Optimal placement and gains of sensors and actuators for feedback control". *Journal of Guidance, Control, and Dynamics*, 17(5):929–934, 1993.